3-2020

Design, Development, and Testing of a Low Cost, Additively-Manufactured, Centrifugal Compressor

Aaron P. Bauer

Design, Development, and Testing of a Low Cost, Additively-Manufactured, Centrifugal Compressor

THESIS

Aaron P. Bauer, 2d Lt, USAF

AFIT/MS/ENY/20-M-254

DEPARTMENT OF THE AIR FORCE
AIR UNIVERSITY

AIR FORCE INSTITUTE OF TECHNOLOGY

Wright-Patterson Air Force Base, Ohio

AFIT/MS/ENY/20-M-254

DESIGN, DEVELOPMENT, AND TESTING OF A LOW COST, ADDITIVELY-MANUFACTURED, CENTRIFUGAL COMPRESSOR

THESIS

Presented to the Faculty

Department of Aeronautics and Astronautics

Graduate School of Engineering and Management

Air Force Institute of Technology

Air University

Air Education and Training Command

in Partial Fulfillment of the Requirements for the

Degree of Masters of Science in Aeronautical Engineering

Aaron P. Bauer, B.S.

2d Lt, USAF

March 2020

AFIT/MS/ENY/20-M-254

DESIGN, DEVELOPMENT, AND TESTING OF A LOW COST, ADDITIVELY-MANUFACTURED, CENTRIFUGAL COMPRESSOR

Aaron P. Bauer, B.S.
2d Lt, USAF

Committee Membership:

Frederick Schauer, PhD
Chairman

Lt Col James Rutledge, PhD
Member

Major Brian Bohan, PhD
Member

ADEDJI B. BADIRU, PhD
Dean, Graduate School of Engineering and Management

Signature Page

Abstract

The Air Force has recently focused on small jet turbine engines as a power source for small, lightweight systems. This is due to higher power density and improved reliability over piston engines. Additive manufacturing capabilities have grown in the last decade. This thesis provides a proof of concept solving the problem of costly and slow compressor design iterations with the maturing field of additive manufacturing.

The three objectives of this research were: 1.) to design, build, and test an additively-manufactured, centrifugal compressor that could substitute into a commercial, off-the-shelf, micro gas turbine engine, 2.) to provide an initial correlation between finite element analysis and compressor failure speed, and 3.) to attempt to characterize the effects of additive manufacturing on compressor performance. These objectives were in an attempt to improve the design cycle cost and the development time cycle from design to validation.

A wide variety of research was accomplished to meet these goals and include: material research on a variety of additively-manufactured materials; measuring the temperature-dependent material properties for additively-manufactured materials; finite element analysis on a variety of compressor designs using the determined temperature-dependent material properties, compressor redesign to enhance the structural capabilities of the compressor; instrumentation and compressor performance assessment; and physical spin testing to determine the failure speed of the manufactured compressors.

Three materials (ULTEM 9085, 300-AMB, and Onyx-Kevlar) were selected and temperature-dependent material properties were measured. Finite element analysis predicted the failure speed of the stock compressor designs and led to an improved design that could fulfill the small jet engine compressor requirements. Physical testing

of both aluminum and ULTEM 9085 with the stock design occurred. A comparison of these compressors' performances demonstrated that the low cost, additively-manufactured materials are viable alternatives to aluminum for certain micro-turbine applications. Decreased material stiffness led to tip wear, effectively eliminating adverse tip clearance effects. This improvement could be optimized to counteract undesirable surface roughness effects on performance. An improved design was produced out of Onyx-Carbon Fiber and was tested to failure.

The results obtained in this work provided an initial proof of concept supporting additively-manufactured compressors for improving the development time cycle. This approach in an enabler for high-risk yet low-cost applications. Additionally, with proper mission planning, additive compressors could provide significant improvements in the cost and weight for limited-life applications.

Acknowledgements

Anything worth doing is worth overdoing.

I would like to thank my adviser, Dr. Fred Schauer, for his limitless guidance, invigorating energy, and contagious enthusiasm for reaching beyond what I thought possible.

I would also like to thank Lt Col Rutledge and Maj Bohan for their expertise and selfless willingness to assist me in creating and editing this thesis. Additionally, I would like to thank the many members of AFRL/RQTC, ISSI, AFIT Model Shop, and the AFIT labs for aiding me in this project, very little of it could have been accomplished without you.

Additionally, I would like to thank my wife, Kaylin, and my close group of friends who supported and encouraged me throughout this long and arduous journey. Finally, Soli Deo gloria!

Aaron P. Bauer

Table of Contents

Page

List of Figures

List of Tables

. List of Abbreviations

Abbreviation	Expansion
AN^2	Area times Rotational Speed, Squared
2D	Two Dimensional
3D	Three Dimensional
ABS	Acrylonitrile Butadiene Styrene
AM	Additive Manufacturing
CAD	Computer-Aided Design
CNC	Computer Numerical Control
CTA	Constant-Temperature Anemometry
DED	Direct Energy Deposition
FDM	Fused Deposition Modeling
FEA	Finite Element Analysis
GTT	Glass Transition Temperature
HDT	Heat Deflection Temperature
HIP	Hot Isostatic Pressing
IC	Internal Combustion
IR	Infrared
MAF	Mass Air Flow Sensor
ME	Material Extrusion
ME-CF	Material Extrusion, Continuous Fiber
MTS	Material Test System
PBF	Powder-Bed Fusion
PEI	Polyetherimide
PLA	Polylactic Acid
TC	Thermocouple
UV	Ultraviolet
VP	Vat Photopolymerization
XY	Flat
XZ	On Edge
ZX	Upright

. List of Symbols

Latin Symbols

Symbol	Definition
a	Speed of Sound
a	Constant
A	Area
b	Constant
C	Constant
c_D	Drag Coefficient
c_L	Coefficient of Lift
C_m	Mass Flow Coefficient
c_p	Specific Heat at Constant Pressure
c_t	Relative Tip Clearance
$C_{\dot{w}}$	Power Coefficient
D	Diameter
e	Specific Internal Energy
E	Energy
E	Voltage
E	Modulus of Elasticity
F	Force
g	Gravity
h	Specific Enthalpy
k	Boltzmann's Constant
k	Thermal Conductivity
k_s	Sand Grain Equivalent Roughness
KE	Kinetic Energy
L	Length
$\dot{m}$	Mass Air Flow Rate
Ma	Mach Number
N	Number
P	Pressure
q	Heat Transfer
Q	Volumetric Flow Rate
r	Radius
R	Air-Specific Gas Constant

Latin Symbols, Continued

Symbol	Definition
R	Resistance
R^2	Statistical Coefficient of Determination
Ra	Surface Roughness
Re	Reynolds Number
Re_k	Roughness Reynolds Number
t	Tip Clearance
t	Thickness
T	Temperature
T_{ij}	Stress Tensor
u	Axial Flow Velocity
u_r	Friction Velocity
U	Linear Rotational Velocity
v	Tangential Flow Velocity
v	Volume Fraction of Material
V	Flow Velocity
V_R	Flow Velocity Relative to Blades
$\forall$	Volume
w	Radial Flow Velocity
w	Width

Greek Symbols

Symbol	Definition
α	Coefficient of Thermal Expansion
α	Angle Between V an U
α	Temperature Coefficient of Resistance
β	Angle Between V and V_R
γ	Ratio of Specific Heats
δ	Nondimensional Pressure
δ	Displacement
∂	Partial Derivative
ε	Slip Factor
ε	Strain
η	Isentropic Efficiency
θ	Angle
θ	Nondimensional Temperature
μ	Dynamic Viscosity
ν	Poisson's Ratio
ν	Kinematic Viscosity

Greek Symbols, Continued

Symbol	**Definition**
π	Pressure Ratio
Π	Nondimensional Pi Terms
ρ	Density
σ	Stress
$\sigma()$	Standard Deviation of ()
τ	Temperature Ratio
τ_A	Applied Torque
ϕ	Flow Coefficient
ψ	Head Coefficient
ω	Rotational Speed

Subscripts

Subscript	**Definition**
1	Compressor Inducer
3	Compressor Exducer
b	Blade
c	Centrifugal
c	Compressor
c	Corrected
e	Exducer
h	Heated
h	Hub
i	index
i	Inducer
m	Mean
o	Original
r	Radial
ref	Reference Condition
s	Specific
s	Static
t	Tangential
t	Tip
t	Total
u	Ultimate
u	Unheated
w	Weighted

DESIGN, DEVELOPMENT, AND TESTING OF A LOW COST, ADDITIVELY-MANUFACTURED, CENTRIFUGAL COMPRESSOR

I. Introduction

With most areas of research, many advances can be made in a small amount of time. However, eventually, future advances require manufacturing or sensing methods that have not yet been fully developed. When this is the case, that research slows down for many years to allow the methods to catch up to the innovation. Additive Manufacturing (AM) often fills in that novel manufacturing method required by many new technologies. A decade ago, AM was confined to the outer regions of research. AM parts were more for modeling and displaying an idea before it was built out of a "real" material with a "real" method. No turbomachinery could ever be built by AM. Not because it did not add anything new to the design process, but rather, because everyone knew that it could not work.

However, the steady marching of technological progress has caught up AM technology to the point that it should not be so easily dismissed in turbomachinery research. The potential to save countless hours of skilled labor and hundreds of dollars per iteration is a huge draw to AM. While some forms of AM have already been used to create working turbomachinery components, little research has been done using the newer "engineering-grade" AM plastics. These are much more attractive to research due to their lower cost and significantly easier operations than metal printers [1].

The design cycle is the time it takes for a concept to go from the "back of the napkin" to a physical part. While the cycle components upstream of the manufacturing method (such as design and initial analysis) can take many weeks, months, or

years to reach an acceptable solution, the manufacturing step always is a bottleneck to research. The more complicated and costly the manufacturing, the more in-depth the a priori design must be. Before any part has even been created to determine if the idea aligns at all with reality, dozen to hundreds of hours have been poured into computer models. By using AM to minimize the costs of the physical manufacturing, the cost savings can be applied to many quick iterations of an idea rather than one large, costly iteration. These many iterations provide more chances to input reality into the design process as the behavior and performance of the previous design is incorporated into the subsequent designs.

Micro-gas turbine engine research has largely remained stagnant for many years. The developments by Japikse [2], Rodgers [3], and Logan [4] in the 1980s-1990s pushed centrifugal compressor research to the outskirts of what was possible at that time. With the huge boom of new technological advancements occurring in AM, it is time to try to apply the new technology to an older problem.

Micro-gas turbine engines are used for a wide range of applications ranging from small-scale ground power units, hobbyist RC aircraft, jet packs, and swarm technology. The research presented in this thesis set out with three primary objectives in mind. The first was to design, build, and test an additively-manufactured centrifugal compressor that could be substituted into a commercial off-the-shelf micro-gas turbine. Demonstrating that plastic centrifugal compressors could withstand the harsh and precise environment of a small jet engine would be a huge boost to the confidence to continue this research. The second objective of this research was to begin to provide an initial correlation between AM compressors and failure speed using Finite Element Analysis (FEA). If it could be shown that FEA accurately predicts failure speed, more effort could be put into development, optimized to the method and the materials. The final research objective was to attempt to characterize the

effects of AM on compressor performance. It is intuitively understood that switching from a precise manufacturing method, such as Computer Numerical Control (CNC) machining, to one currently more infantile in its precision would lead to a plethora of increased inefficiencies and chances for failure. However, the primary question that many researchers need to know before they begin designing for AM is how great of a performance loss should be expected. If the improved design cycle time and increased available geometrical complexity outweighs the losses in efficiency and compressor lifetime, than AM would be the preferred solution.

All three of these research objectives were completed with the focus of decreasing the design cycle cost and time between iterations of compressors. Figure 1 depicts a possible design cycle for compressor research. Beginning with an initial compressor design, a quick material research is required to determine if there is a chance the compressor design could work. After selecting a collection of possible materials, an in-depth material testing process would begin. This is necessary in order to create a more accurate computer model.

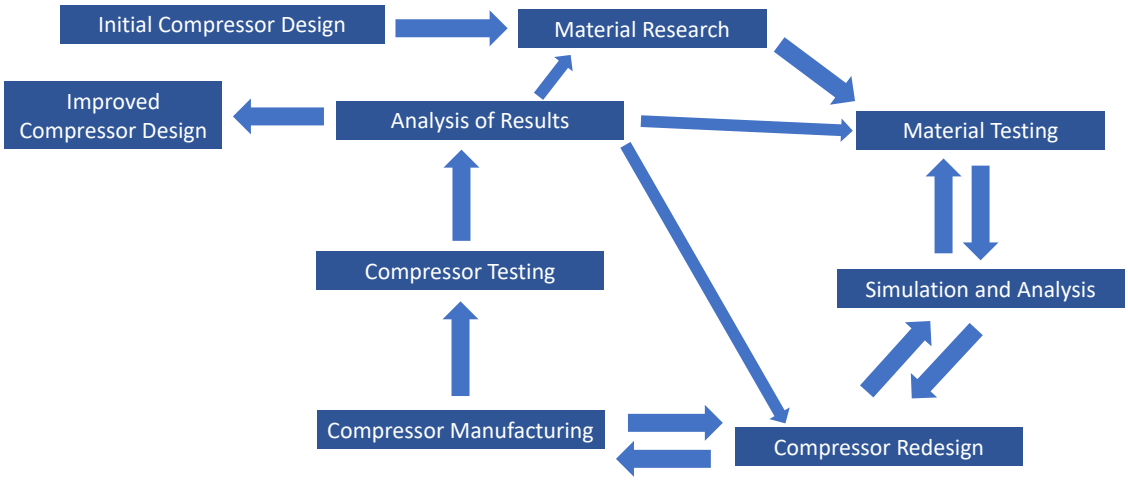

Figure 1. Compressor Design Cycle Process

Following the material testing is the computer simulation. At this point, if the model is not giving adequate results, more material testing might be necessary -

either with different materials or more conclusive testing of the previous materials. After satisfactory simulation, there can be a time of redesign in which the initial compressor design is modified to conform to the material limitations discovered in the material testing. Following the redesign, the compressor can be manufactured. If some unknown manufacturing limit exists, such as part thickness or tolerance, the design is sent back to be redesigned. Once the compressor physically exists, it is tested in an environment similar to the expected operating conditions. Upon analysis, the decision to accept the new design as adequate or repeat the design loop again is made. This design cycle is repeated until the desired results are obtained [5].

II. Background and Literature Review

While a huge number of compressor types exist with a variety of applications, two types are commonly seen in gas turbine engines: the axial compressor and the centrifugal compressor. Two primary differences between these two compressor types are 1.) flow enters and exits the axial compressor in the axial direction while the centrifugal compressor turns the flow from an axial direction to the radial direction 2.) the pressure ratio per stage for an axial compressor is typically less than 2.5 while the centrifugal compressor is capable of reaching pressure ratios of 4-10+ [6]. While centrifugal compressors have typically been cast and machined, new research is attempting to incorporate additive manufacturing into the production of centrifugal compressors.

The following literature review analyzes previous research that will be used to solve the AM compressor fabrication problems. Section 2.1 is focused on centrifugal compressors and covers the common nomenclature, typical uses, compressor fundamentals, structural limits, design considerations, small compressor trends, and current AM compressor research. Section 2.2 discusses the material research. This includes an introduction to AM methods, a comparison of common AM materials, and proper material testing practices. Section 2.3 briefly introduces the concepts behind finite element analysis. The final section, Section 2.4, discusses the four primary sensors used in this research and introduces to the concept of uncertainty.

2.1 Centrifugal Compressors

Turbomachinery is broadly defined as any device that transfers energy either into or out of a flowing fluid through the use of moving blades. This includes open turbomachinery - such as propellers, wind turbines, and fans - and closed turbomachinery -

including shrouded fans, turbines, pumps, and compressors. The closed turbomachinery is distinguished by the determinate amount of mass flow through the machine and includes all turbomachinery seen inside of a gas turbine engine [6]. The indeterminate amount of mass flow for open turbomachinery is shown in Figure 2a in contrast to the determinate, closed turbomachinery shown in Figure 2b.

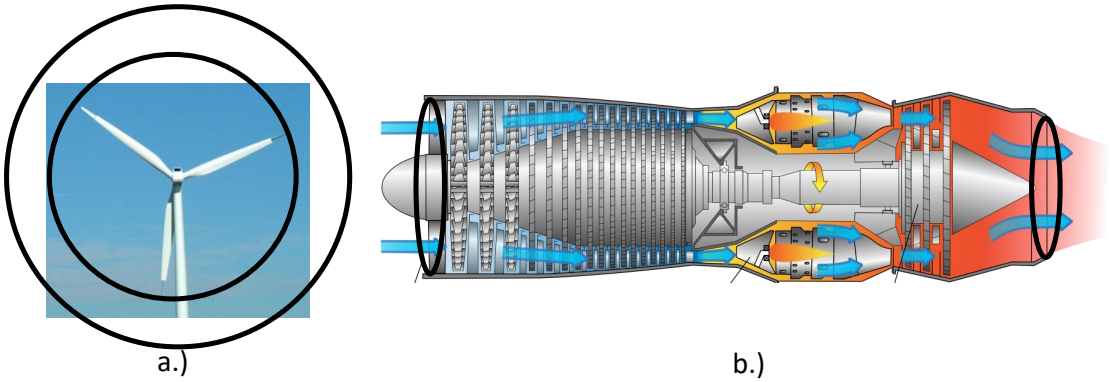

Figure 2. Open versus Closed Turbomachinery. a.) Indeterminate Regions of Flow Affected by Open Turbomachinery. b.) Determinate Region of Flow Affected by Closed Turbomachinery. Adapted from [7]

The primary mission of a compressor in a gas turbine engine is to increase the pressure of the incoming air. This is done to both improve the efficiency and power density of the combustor and to provide a stagnation pressure that allows expansion and thrust to occur. This pressure rise needs to occur with minimal losses in order to allow continuous operation powered by the turbine [6]. The following sections cover background research regarding turbomachinery and centrifugal compressors and include common nomenclature in Section 2.1.1, common uses for centrifugal compressors in Section 2.1.2, fundamental equations critical to the understanding of compressors in Section 2.1.3, design features relevant to AM in Section 2.1.5, common centrifugal compressor trends in Section 2.1.6, and a brief overview on the research into AM compressors with a focus on micro-gas turbine engines in Section 2.1.7.

2.1.1 Engine Station Nomenclature.

Both compressor stations and engine stations have their own unique nomenclature. Using the compressor station nomenclature would assist in describing both the rotors/stators region of the compressor stage and the multiple stages common in compressors. However, for this entire work, the nomenclature common in gas turbine engines will be used consistently unless otherwise noted. This notation is shown in Figure 3. The stations are numbered 0 through 9. Station numbers appear to be missing in Figure 3 because the same numbering notation is typically consistent for all gas turbine engines of increasing complexity and denote components that are absent in the simple turbojet engine.

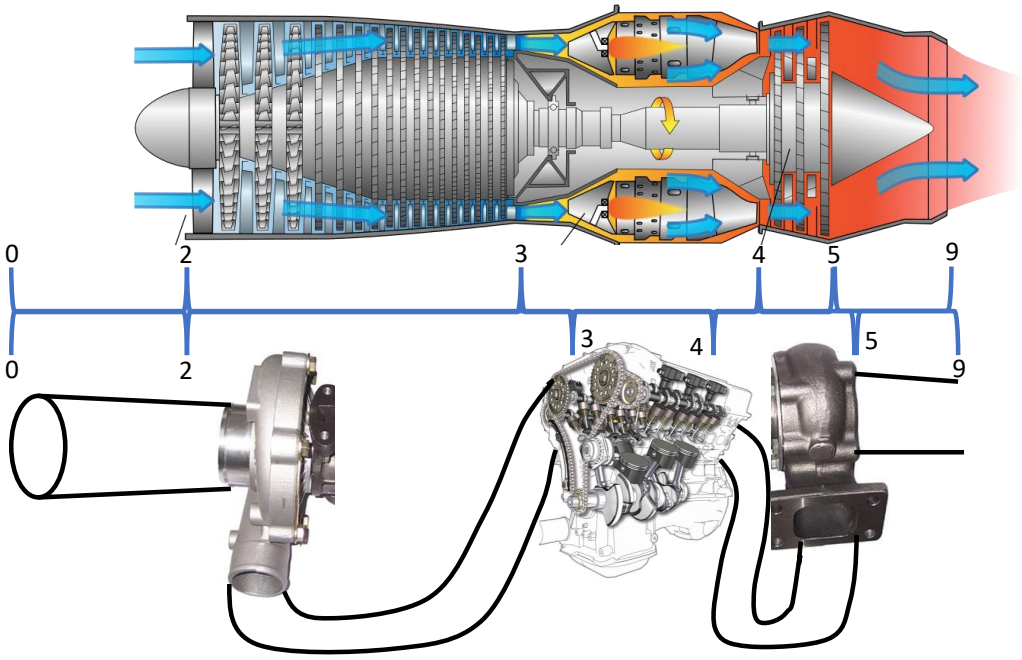

Figure 3. Engine Station Designations for a Single-Spool Turbojet and a Turbocharged Internal Combustion Engine. Adapted from [7].

For a single-spool turbojet engine, from 0-2 is the air intake. 2-3 is the compressor section where shaft energy is transferred to the air in the form of a temperature and pressure rise. 3-4 is the combustor section where energy is added from fuel. 4-5 is the turbine section where energy is extracted from the flow to power the compressor.

5-9 is the nozzle section where the high-energy gasses are accelerated to produce thrust [6]. The Internal Combustion (IC) engine stations can be similarly numbered - more so when a turbocharger is included. 0-2 is the air intake. 2-3 includes the turbocharger compressor and the compression stroke of the IC engine. 3-4 is the combustion stroke. 4-5 is both the expansion stroke of the IC engine and the turbine side of the turbocharger. 5-9 is the waste exhaust [8].

2.1.2 Typical Uses.

There are two well-known uses for centrifugal compressors that both relate to this project. The first is in small ($\leq$10 kg/s) gas turbine engines. One common gas turbine engine is the JetCat P400. This engine is used in many hobbyist RC airplanes and has even been used in a jetpack-wingsuit hybrid [9]. This engine is shown in Figure 4. This engine is important to this research because the printed compressor is closely modeled off of this compressor with the eventual goal of supplanting the aluminum compressor with a lightweight additively-manufactured compressor.

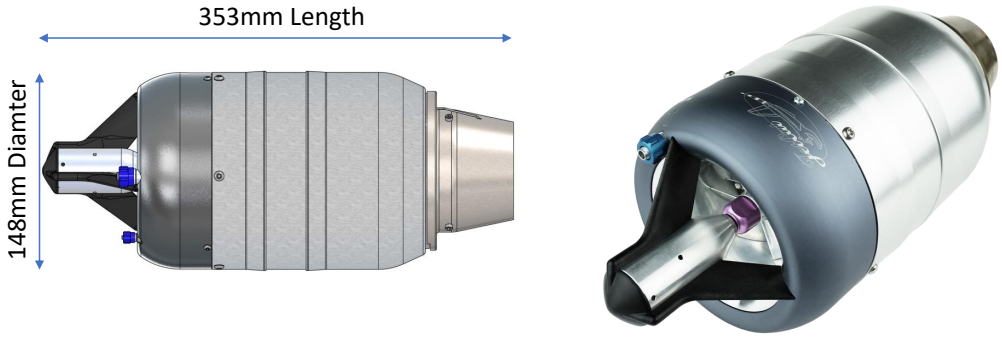

Figure 4. Images of a JetCat P400 Gas Turbine Engine [10].

Key published specifications for the JetCat P400 are shown in Table 1. The five primary values relating to the compressor are the pressure ratio, the mass flow, the idle speed, the maximum speed, and the weight. In order to achieve a successful design, a replacement compressor aerodynamically must be able to increase the air

Table 1. JetCat P400 Key Published Specifications [10]

Pressure Ratio	3.8	Weight	3.65 kg
Mass Air Flow	0.67 kg/s	Price	12,000 USD
Idle Speed	30 kRPM	Idle Thrust	14 N
Maximum Speed	98 kRPM	Maximum Thrust	397 N
Exhaust Power	116 kW	Exhaust Velocity	590 m/s

pressure close to 3.8 while passing through a mass flow rate close to 0.67 kg/s. In addition, it must structurally be able to withstand the 98 kRPM rotational speed. Ideally, the proposed solution would be lighter than the original compressor.

The second common use for centrifugal compressors is seen within a turbocharger. Turbochargers are typically found on performance cars, trucks, and airplanes, pressurizing the air prior to the IC engine. The turbocharger used in this research was the Garrett GTX5008R, used in IC engines ranging from 720-1270 hp and displacements of 2.5 L-10.0 L [11].

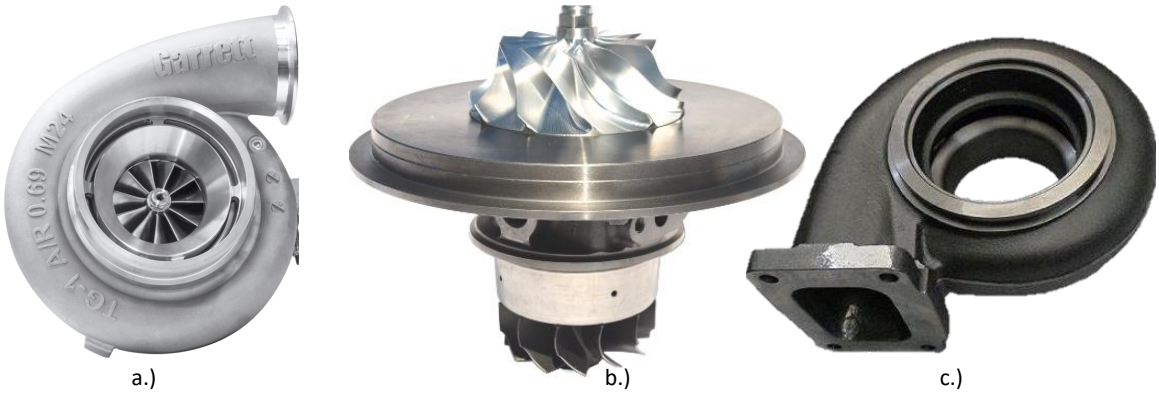

Figure 5. Images of a Garrett GTX5008R Turbocharger. a.) GTX5008R Compressor Inside of Compressor Housing. b.) GTX5008R Centre Housing Rotating Assembly (CHRA). c.) GTX50 Turbine Housing [11]

The purpose of this turbocharger was to provide a means to spin the AM compressors to the maximum speed with adequate energy to measure compressor performance, for this reason, the GTX5008R turbocharger was used. Table 2 shows the comparison between the P400 and the GTX5008R compressors. Because the GTX5008R compressor pressure ratio (π_c), mass flow rate ($\dot{m}$), and RPM were all greater than the

P400, the turbine side likely could deliver adequate energy to spin the test compressor up to the desired speed and π_c.

Table 2. Compressor Comparison of JetCat P400 to GTX5008R. *Measured

Compressor	π_c	$\dot{m}$, kg/s	RPM_{max}	D_i*	D_e*	N_{blades}	θ_{blade}*
JetCat P400	3.8	0.67	98 kRPM	75 mm	10 mm	14 (7+7)	57.9°
GTX5008R	4.75	0.15-0.95	100 kRPM	80 mm	108 mm	11	46.75°

2.1.3 Compressor Fundamentals.

2.1.3.1 Velocity Diagrams.

An ubiquitous manner to describe the many velocities present within a centrifugal compressor is with a velocity diagram [2, 4, 6]. An example of a velocity diagram applied to a centrifugal compressor is shown in Figure 6. The stationary coordinate system is looking at motion from outside the rotor while the moving coordinate system is the flow as seen by an observer fixed onto the surface of the rotor. U is the rotational velocity of the blade, defined in Equation 1. The incoming flow velocity (V_1) is assumed purely axial, therefore is purely the incoming axial flow velocity (u_1). The relative incoming velocity is the sum of the rotational velocity and the axial velocity; the relationship is shown in Equations 2-3. The angles between the velocities are shown in Figure 6.

$$U_j \equiv \omega_j r_j \tag{1}$$

$$\overrightarrow{V_R} = \overrightarrow{u} - \overrightarrow{U} \tag{2}$$

$$V_R = U\sin(\beta) = u\cos(\beta) \tag{3}$$

At the compressor exit, there is exit velocity (V), broken into radial (w) and tangential (v) components of velocity. The relative velocity is described in Equation 4.

$$\overrightarrow{V_R} = (\overrightarrow{v} - \overrightarrow{U}) + \overrightarrow{w} \tag{4}$$

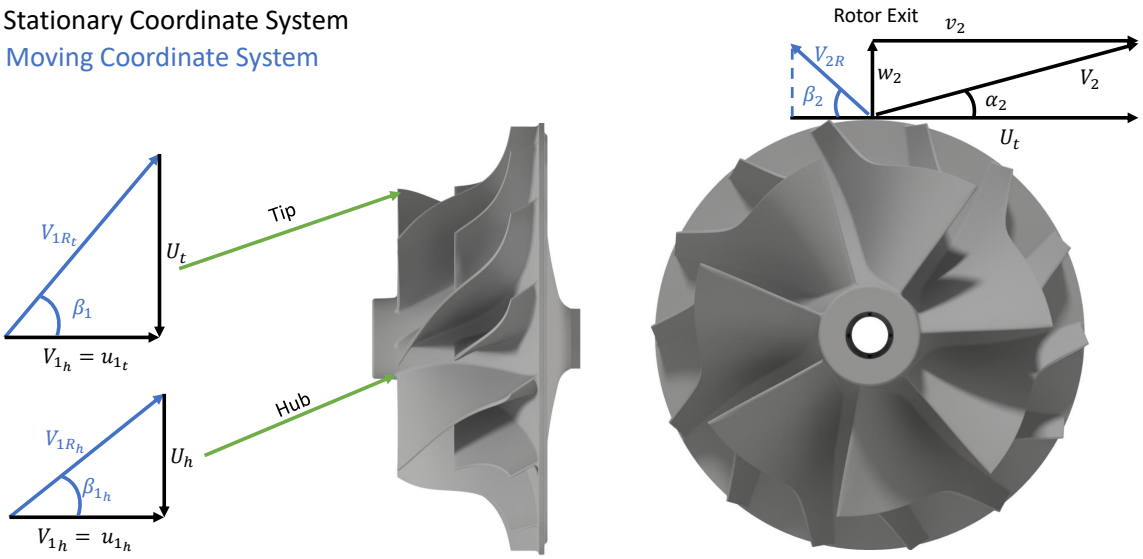

Figure 6. Velocity Diagram for a Centrifugal Compressor

2.1.3.2 Conservation Equations.

The three common conservation equations seen in fluid dynamics are the continuity equation, the momentum equation, and the energy equation. A detailed derivation of these equations can be found in [12]. The continuity equation, shown in Equation 5, mathematically describes the local conservation of mass; mass cannot be created or destroyed. The momentum equation is the application of Newton's Second Law of Motion on a fluid, shown in Equation 6. The energy equation in is the application of the First Law of Thermodynamics that states that, like mass, energy cannot be created or destroyed. This is shown in Equation 7 [12, 13].

$$\partial_0[\rho] + \partial_i[\rho V_i] = 0 \tag{5}$$

$$\partial_0[\rho V_i] + \partial_j[\rho V_j V_i] = \rho g_i + \partial_j[T_{ji}] \tag{6}$$

$$\partial_0[\rho(\frac{V^2}{2} + e)] + \partial_i[\rho V_i(\frac{V^2}{2} + e)] - \partial[T_{ij}V_j] + \rho g_i V_i - \partial_i[q_i] = 0 \tag{7}$$

The integral forms of these three equations describe the time-rate of change of the quantity within a control volume. For steady flow in the JetCat P400 centrifugal compressor control volume in Figure 7, the continuity equation reduces to Equation 8. The constant mass flow rate is the product of the density and the dot product of the area and the mean velocity [4].

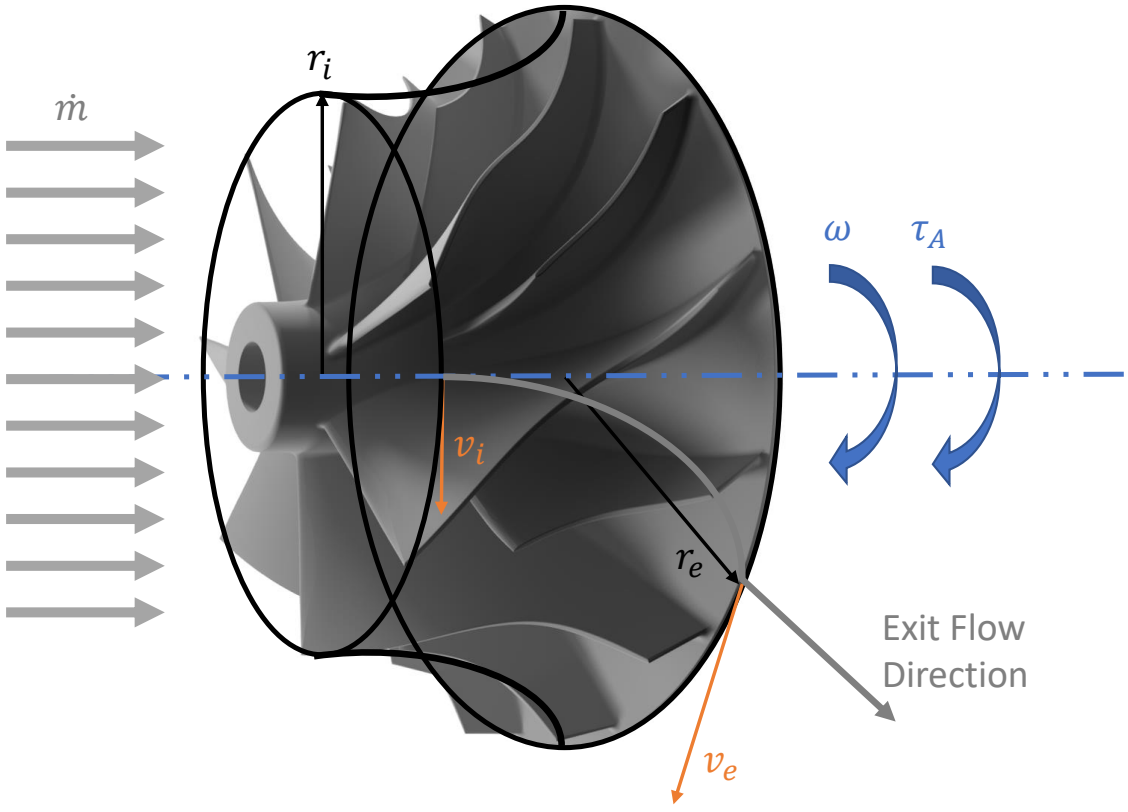

Figure 7. Control Volume for Centrifugal Compressor

$$\rho_i(A_i \bullet V_{m,i}) = \dot{m} = \rho_e(A_e \bullet V_{m,e}) \tag{8}$$

Assuming steady, invicid, and constant rotor exit velocity, the momentum equation reduces to a description of the applied torque relative to the fluid flow, Equation 9. Power is the product of torque and rotational speed. Multiplying Equation 9 by the speed leads to a description of the power required, shown in Equation 10 [4, 6].

$$\tau_A = \dot{m}(u_i r_i - w_e r_e) \tag{9}$$

$$\dot{W}_c = \dot{m}\omega(u_i r_i - w_e r_e) \tag{10}$$

The integral form of the energy equation states that the energy in the incoming flow and the heat transfer out of the control volume must equal the work done on the control volume and the energy leaving the flow. Assuming steady flow, no gravitational effects, and inviscid flow leads to Equation 11 [4], [6].

$$\dot{W}_c = \dot{m}(h_{t,e} - h_{t,i}) \tag{11}$$

Equating Equation 10 with Equation 11 leads to the Euler Pump Equation, which describes the change in the enthalpy of the flow as a function of the speed, radii, and the change in the velocities of the flow.

$$\omega(u_i r_i - w_e r_e) = (h_{t,e} - h_{t,i}) \tag{12}$$

Assuming a calorically-perfect gas with constant specific heats, can be shown to lead to Equation 13.

$$T_{t,e} - T_{t,i} = \frac{v_e U_t}{g c_p} \tag{13}$$

2.1.3.3 Nondimensionalization.

While Equation 13 can help determine the state of a specific compressor, knowing everything else about the compressor, the equation does not readily describe how two compressors compare. Additionally, the inclusion of units prevents a clean comparison to be made. The nondimensionalization process described in this section allows general comparisons to be made without regard to units, dimensions, and a whole array of other effects. The majority of all nondimensionalization is based on Buckingham's Pi Theory [14]. In this, all dimensions are broken into their three base dimensions: force, length, and time (Flt) or mass, length, and time (mlt). From this, Buckingham showed that the number of nondimensional variables was always fewer than the number of physical variables. The number of nondimensional "Π" terms is always equal to the number of physical variables minus the number of base dimensions needed to describe the system. The two most common Π terms seen in fluid dynamics are the Reynolds number and the Mach number (In this case, the machine Ma). Typical equations for these and a common interpretation of the Π term is shown in Equations 14-15 [13].

$$\Pi_1 = Re = \frac{\rho U D}{\mu} = \frac{\rho \omega D^2}{\mu} = \frac{\text{Inertial Forces}}{\text{Viscous Forces}} \tag{14}$$

$$\Pi_2 = Ma = \frac{U}{a} = \frac{\omega D}{a} = \frac{\text{Inertial Forces}}{\text{Compressibility Forces}} \tag{15}$$

Three more nondimensional parameters are common when determining compressor performance. They are the Flow Coefficient (Equation 16), the Head Coefficient (Equation 17), and the Power Coefficient (Equation 18) [2].

$$\Pi_3 = \phi = \frac{Q}{UA} = \frac{C_m}{U} = \frac{C_m}{\omega D} \tag{16}$$

$$\Pi_4 = \psi = \frac{\Delta h_t}{U^2} = \frac{\Delta h_t}{(\omega D)^2} \tag{17}$$

$$\Pi_5 = C_{\dot{W}} = \frac{\dot{W}}{\rho \omega^3 D^5} \text{ or } \frac{\Delta h_t}{h_{t_1}} \tag{18}$$

Because these five Π terms fully describe the compressor behavior, there will be similarity between two compressors with the same parameters. Because of this, geometric scaling of compressors cannot completely happen. This is clearly shown by the presence of varying $\omega^a D^b$ terms. For Ma, ϕ, and ψ, a and b are 1.0. This means that to scale the diameter to twice the original size, the speed must be reduced in half. However, for Re, $a = 1$ but $b = 2$. This means that to double the diameter, the speed must be quartered to match Re. Finally, $C_{\dot{W}}$ has an $a = 3$ and a $b = 5$, fixing the diameter-speed ratio to some other ratio. Typically, $a = 1$ and $b = 1$ to match the majority of parameters and Re is not scaled [2, 4].

Another common type of nondimensional parameter is dimensionless reference conditions. Because any thermodynamic system can be described by two intrinsic thermodynamic properties, only two base nondimensional parameters are required: dimensionless pressure and temperature, shown in Equation 19-20. Other pressures, temperatures, mass flow rates, and speeds can be corrected (noted with a subscript "c") using these two base parameters. These are shown in Equations 21-24.

$$\delta = \frac{P_{t_0}}{P_{ref}} \tag{19}$$

$$\theta = \frac{T_{t_0}}{T_{ref}} \tag{20}$$

$$P_{c_i} = \frac{P_i}{\delta} \tag{21}$$

$$T_{c_i} = \frac{T_i}{\theta} \tag{22}$$

$$\dot{m}_c = \frac{\dot{m}\sqrt{\theta}}{\delta} \tag{23}$$

$$\omega_c = \frac{\omega}{\sqrt{\theta}} \tag{24}$$

Two additional nondimensional parameters are the specific speed in Equation 25 and the specific diameter in Equation 26. Both parameters are some ratio of the flow coefficient to the head coefficient, describing the amount of flow compared to the amount of energy put into the flow.

$$\omega_s = \frac{\phi^{1/2}}{\psi^{3/4}} = \frac{\omega Q^{1/2}}{(gH)^{3/4}} \tag{25}$$

$$D_s = \frac{\psi^{1/4}}{\phi^{1/2}} = \frac{D(gH)^{1/4}}{Q^{1/2}} \tag{26}$$

Figure 8 shows a map for a centrifugal compressor relating the ω_s to the D_s and inesntropic efficiency (η) at a set Re. An island of higher efficiency appears between specific speeds of 60-1,500 RPM and specific diameters of 0.5-2.0. If the specific speed increases past this region of higher efficiency, an axial-flow compressor would be a preferred solution [15].

One of the commonly referenced plots regarding specific speed is shown in Figure 9. This plot shows the polytropic efficiency of the impeller as a function of the specific speed. Data for three ranges of blade backsweep are shown. One thing of note is that the maximum efficiency for centrifugal compressors appears to be 95% primarily for backsweep angles between 25-50° and specific speeds between 0.6 and 0.8 [3]. The optimum ω_s leads to higher speeds. However, by lowering the speed, the same mass-flow can be reached at a slight loss of compressor efficiency [16].

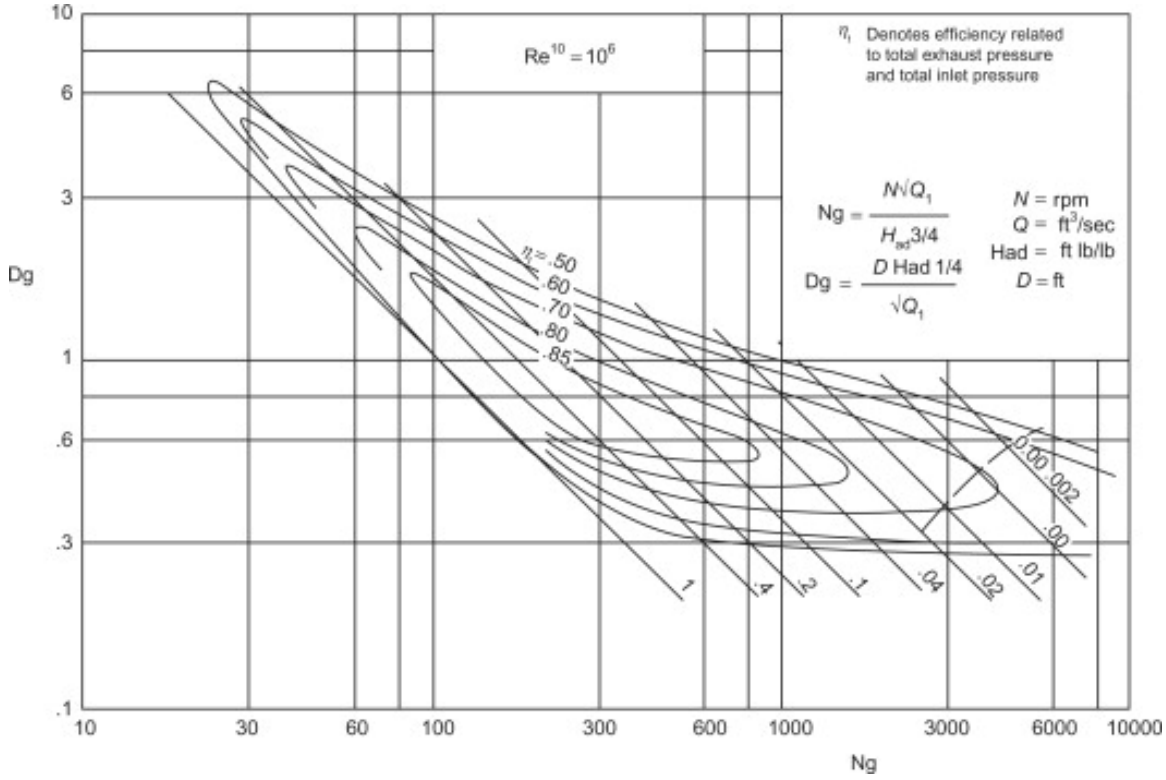

Figure 8. Centrifugal Compressor Specific Speed and Diameter Map [15]

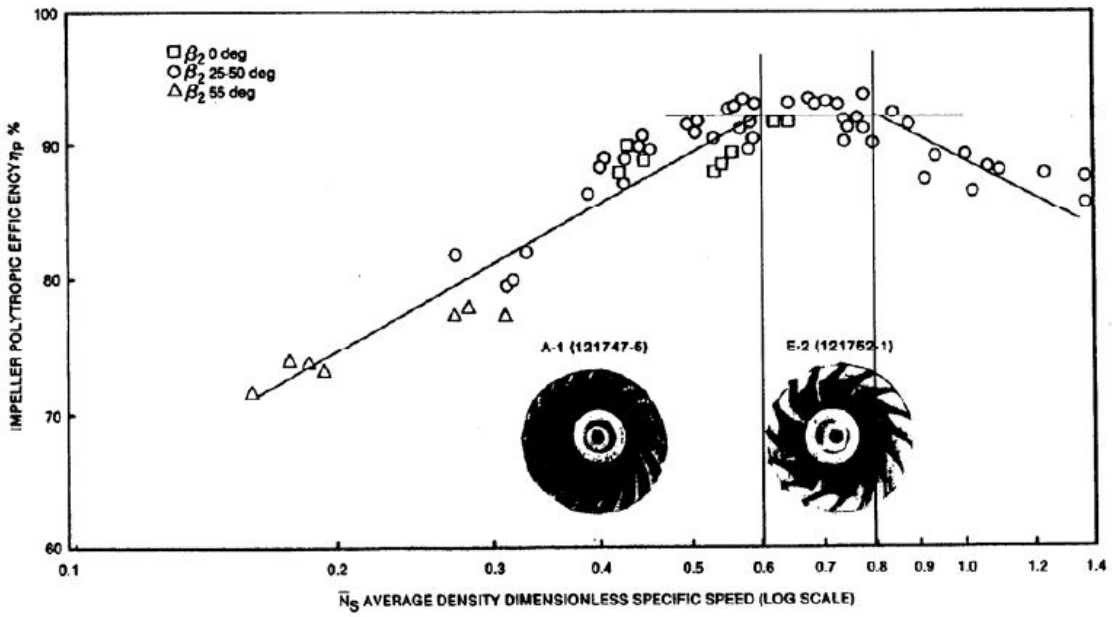

Figure 9. Centrifugal Compressor Specific Speed Versus Efficiency [3]

A common nondimensional parameter for centrifugal compressors is the slip factor (ε). This is defined as the ratio of the exiting swirl velocity to the rotor tip speed, $\varepsilon \equiv v_e/U_t$. An analytically-derived common slip factor is found in [4]. Other slip factors can be found either analytically or through correlations. A list of the more common slip factors is shown in Table 3. Using this definition, Equation 13 can be rewritten into Equation 27, and the pressure ratio can be described using Equation 28. All of the slip factor correlations in Table 3 predict an increased slip factor with increasing the number of blades. This demonstrates one of the faults of ignoring the viscous effects in compressor analysis. The slip factor is balanced by high blade counts to improve performance while a lower blade count is desired to minimize viscous drag on the blades [6].

$$T_{t,e} - T_{t,i} = \frac{\varepsilon U_t}{g c_p} \tag{27}$$

$$\pi_c = \frac{P_{t,e}}{P_{t,i}} = \left(1 + \frac{\eta_c \varepsilon U_t^2}{g c_p T_{t,i}}\right)^{\gamma/(\gamma-1)} \tag{28}$$

Table 3. Common Equations for Slip Factor

Originator	Slip Factor, $\varepsilon =$
Logan [4]	$1 - \pi U_2 sin\beta_2 / N_{blades}$
Mattingly [6]	$1 - 2/N_{blades}$
Balje [17]	$1 - 0.75\pi sin\beta_2 / N_{blades}$
Busemann [18]	$1 - 2.4/N_{blades}$
Eck [19]	$[1 + 2sin\beta_2/(N_{blades}[1 - (D_{1S}/D_2)])]^{-1}$
Pfleiderer [20]	$[1 + 8(k + 0.6sin\beta_2)/(3N_{blades})]^{-1}$
Stodola [21]	$1 - \pi/N_{blades} * [sin\beta_2/(1 - \phi_2 cot\beta_2)]$
Stanitz [21]	$1 - 0.63\pi/N_{blades} * [1/(1 - \phi_2 cot\beta_2)]$

A final non-dimensional parameter to wrap up this discussion is likely the most well-known non-dimensional parameter. The ratio of the output power to the input power is one description of efficiency. A second description of efficiency is the ratio of the ideal input power to the actual input power. This second form is typically

seen in the discussion of compressors. For isentropic compression, the temperature ratio should rise by isentropic pressure ratio, as seen in Equation 29. This is the ideal amount of work imparted into the flow. The actual amount of work imparted into the fluid is the actual rise in temperature, τ_c. For any non-isentropic system, the temperature ratio will be greater than the isentropic temperature ratio based on the pressure ratio. The ratio of these two is the isentropic efficiency, shown in Equation 30 [2, 4, 6].

$$\tau_{c,isentropic} = \pi_c^{\frac{\gamma-1}{\gamma}} \tag{29}$$

$$\eta_c = \frac{\pi_c^{\frac{\gamma-1}{\gamma}} - 1}{\tau_c - 1} \tag{30}$$

2.1.4 Structural Limits.

The incredible geometrical complexity of centrifugal compressors makes it near impossible to analytically predict failure. For any actual failure prediction, finite element analysis (Section 3.2) is a much more reliable method. A multitude of conflicting material properties must be considered including strength, stiffness, corrosion resistance, fatigue strength, ductility, toughness, and density. A comparison of materials is seen in Section 2.2. The aerodynamic desire for large flow passages demand thin blades and the effects of surface roughness tend to limit complex geometries [2].

Figure 10 depicts the results from a characteristic FEA study and the seven areas of possible failure seen in centrifugal compressors [2]. It is estimated that almost 98% of all stresses within a compressor are due to the centrifugal loading. The pressure forces account for around 0.25% and the thermal stresses account for a constant 2% [22]. While the thermal stresses are minimal, the effects of the thermal profile are not. Region 4 in Figure 10 is the region of highest expected temperature. Japikse [2] lists four more observations to the stress analysis shown in Figure 10. The first is the

high buckling load anticipated in the blade-body interface near the outer diameter. The second is that the high bore stresses in the disk could lead to a burst failure. The third is that the blade roots are not subject to high stresses due to the thickness distribution of the blades. The final is that the cutout shaping of the backface of the compressor both decreases the peak stresses and shifts the location away from the bore.

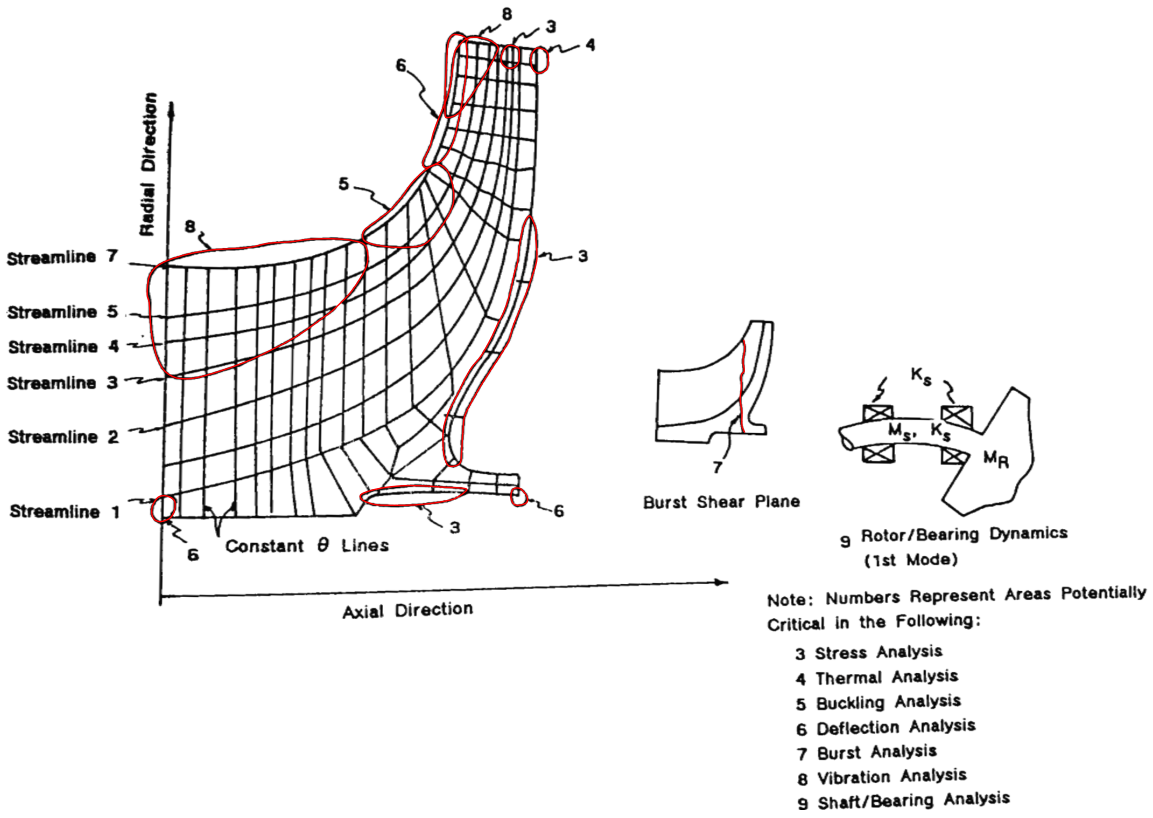

Figure 10. Critical Zones of Stress for a Centrifugal Compressor [2]

The following two sections delve deeper into compressor failure. Section 2.1.4.1 analyzes the literature surrounding turbocharger and centrifugal compressor failures. Section 2.1.4.2 is the derivation of two simplified structural solutions that provide similarity solutions when scaling material properties.

2.1.4.1 Turbocharger Compressor Wheel Burst.

Wheel burst occurs when the experienced stresses overcome the material's ability to hold together. While wheel burst is typically seen in the turbine due to the significantly hotter temperatures, novel designs, untested materials, and random flaws can lead to compressor burst. In this research, the relatively high specific strength of aluminum is likely to be replaced with a lower specific strength material. This will push the compressor much closer to the edge of its operating region and compressor failure is likely to occur [23]. There are three locations where compressor overspin failures commonly occur. The first, and most prevalent, is through the bore, shown in Figure 11a. This failure typically leads to three or more large fragments simultaneously separating from the shaft [23]. Wheel burst failure is due to higher average tangential stresses near the hub than the material can withstand [24]. The second failure is at the blade tips, shown in Figure 11b. This failure is due to a combination of higher tip temperatures [2] and bending stresses on the compressor back wall [25].

Figure 11. Centrifugal Compressor Failure. a.) Bore Failure. b.) Outer Blade Tip Failure [25]

The final common failure is on the blades. Figure 12a depicts a failure of the outer rim of the compressors. This leads to the blades' catestrophic removal. Figure 12b shows the compressor blade tip failing. Japikse predicts that this failure was due

to excessive vibration, shown in Region 8 of Figure 10 [2]. The final blade failure, not pictured, is where the compressor blades peel completely off of the compressor body starting at the large stress concentration at the top of the blades [23]. Because compressor failure tends to introduce material fragments downstream, compressor failure can lead to total engine failure.

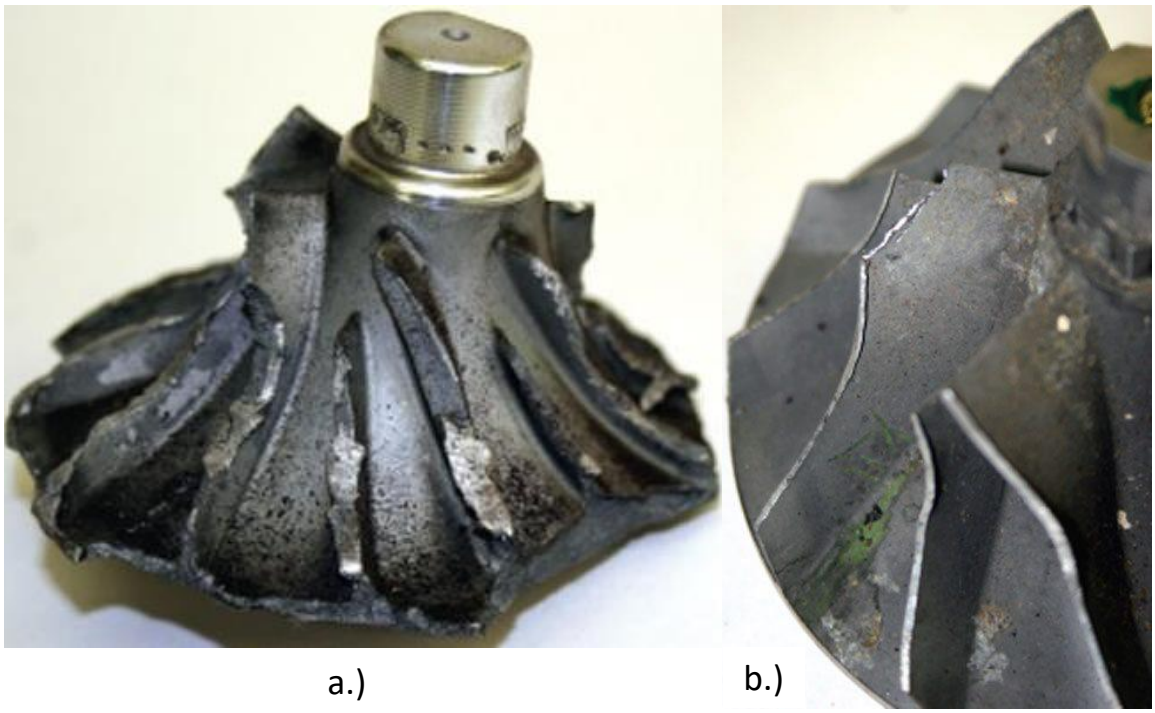

Figure 12. Centrifugal Compressor Failure. a.) Wheel and Blade Failure. b.) Blade Tip Failure [25]

2.1.4.2 Simplified Solution.

While axial compressors can rely on an AN^2 approach (cross-section times rotational speed, squared) to initially predict failure [6], centrifugal compressor geometries are too complicated to completely use this technique. By splitting the structural problem into two regions, two of the likely regions of failure can be analyzed and some important conclusions can be reached. Two assumptions apply to the following analysis: isotropic material properties, and a homogeneous compressor model.

The first simplified region is the connection between the blades and the body of the compressor in the inducer region. This region is almost exclusively in tension and can be treated to the same AN^2 analysis seen in [6]. Figure 13 is a compressor that had been cut to the beginning of the blades. The thickness of the blades (t) and the length of the blades (L) is known and the predicted point of highest stress is at the root of the blade.

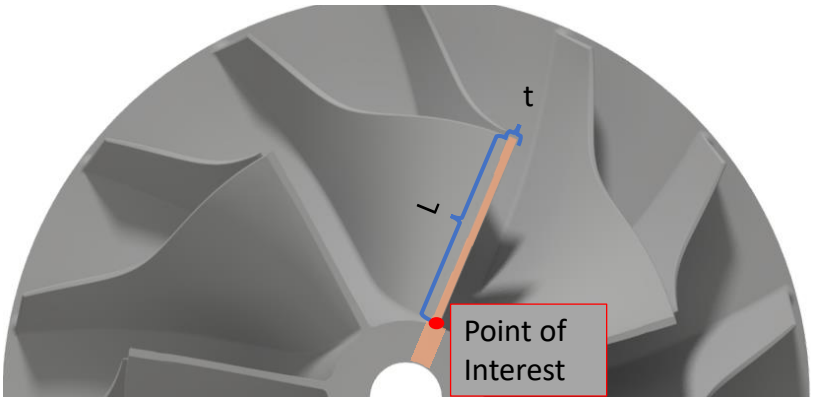

Figure 13. Simplified Compressor Blades

The likely location of failure in this simplified region's analysis is in the blade-disk interface; this is the point of interest labeled in Figure 13. The blade-disk interface in Figure 13 will fail when the centrifugal stress, σ_c, exceeds the ultimate stress, σ_u of the material. From Mattingly [6], the forces at the hub of the blade are described by Equation 31, where A_b is the thickness times a small depth z. If this z can be considered "small", it is factored into the σ_c. For constant thickness blades, the stress is calculated in Equation 32. By solving the integral and rearranging terms, Equation 33 is found. At failure, $\sigma_c = \sigma_u$. The form of this equation is important because it divides the material properties (ρ and σ_u) on the left and the designed properties (ω and r) on the right. If the compressor design is unaltered, to prevent failure, the same specific strength must be maintained. Halving the specific strength requires the speed to decrease to $\approx 71\%$ of the original speed to prevent failure.

$$F_c = \int_{r_h}^{r_t} \rho\omega^2 A_b r dr \tag{31}$$

$$\sigma_c = \rho\omega^2 \int_{r_h}^{r_t} r dr \tag{32}$$

$$\frac{\sigma_u}{\rho} = \frac{\omega^2(r_t^2 - r_h^2)}{2} \tag{33}$$

The second region that can benefit from simplified analysis is the burst shear plane; this is Region 7 from Figure 10. This plane is showed in Figure 14. Rotating disks such as this have two components of stress: the radial and the tangential. The radial stress is due to the material further away from the center of rotation pulling on the more inner regions. The tangential stress is the stress in the tangential direction due to the material resisting expansion outward.

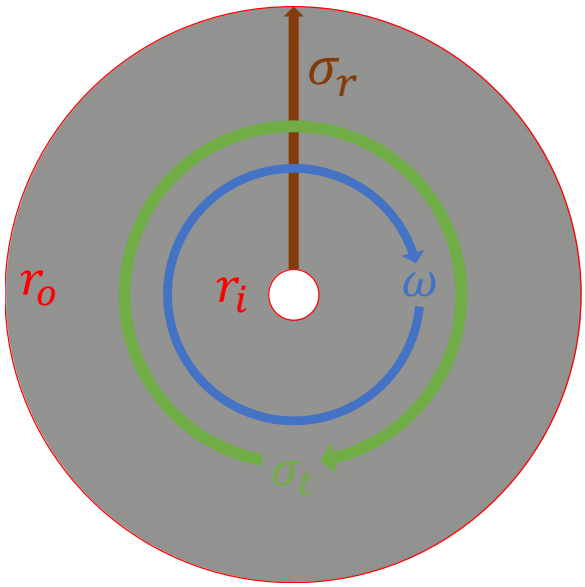

Figure 14. Simplified Compressor Body

Assuming a constant thickness annular disk, Roark provides formulae for calculating the radial and tangential stresses, [26]. It can be shown that the maximum radial stress ($\sigma_{r,max}$) occurs at the geometric mean of the radii: $r = \sqrt{r_i r_o}$. The max-

imum tangential stress ($\sigma_{t,max}$) occurs at r_i. Evaluating Roark's equations at these respective locations leads to Equations 34 and 35.

$$\sigma_{r,max} = \frac{3+\nu}{8}\frac{\rho\omega^2}{2}(r_o - r_i)^2 \tag{34}$$

$$\sigma_{t,max} = \frac{\rho\omega^2}{4}[(3+\nu)r_o^2 + (1-\nu)r_i^2] \tag{35}$$

Evaluating at failure, $\sigma_u = \sigma_{r,max} = \sigma_{t,max}$. Similar to above, the specific strength is important to preventing a disk burst. However, the Poisson's ratio (ν) makes it difficult to reformat both equations into a side with material properties (σ_y, ρ, and ν) and a side with purely design properties (ω, r_i, r_o). The maximum radial and tangential stresses are shown in Equations 36 and 37. Note that ν still appears in the right hand side of Equation 37.

$$\frac{\sigma_u}{\rho(3+\nu)} = \frac{\omega^2}{16}(r_o - r_i)^2 \tag{36}$$

$$\frac{\sigma_u}{\rho(3+\nu)} = \frac{\omega^2}{4}\left(r_o^2 + \frac{1-\nu}{3+\nu}r_i^2\right) \tag{37}$$

A cursory overview of the materials that might be used in replacement compressors (metals and stiff polymers) suggests that the expected range of Poisson's ratios lies between 0.28 and 0.46 [27]. This leads to values of $(1-\nu)/(3+\nu)$ between 0.22 and 0.16, respectively. Because $r_o^2 >> r_i^2$, completely ignoring the $f(\nu)r_i^2$ term only affects Equation 37 by approximately 0.18%. This leads Equation 38.

$$\frac{\sigma_u}{\rho(3+\nu)} = \left(\frac{\omega r_o}{2}\right)^2 \tag{38}$$

For the P400 design, Table 4 substitutes the material and design parameters into the three failure equations derived above (Equations 33, 36, and 38). From these,

it is predicted that the ultimate strength will be exceed first in the inside wall of the shaft. However, exceeding the tensile ultimate strength in compression does not necessitate failure. Instead, plastic and elastic deformations will shift the stresses around to prevent failure from occurring. This will continue to happen until there is a region of failure from one surface to another, leading to the burst shear plane seen in Region 7 of Figure 10 [28].

Table 4. Al 7075-T6 Material Properties, Jet P400 Compressor Design Properties, and Evaluated Simple Failure Equations [29]

σ_u	572 MPa		r_h	0.0127 m
ρ	2,810 kg/m^3		r_t	0.038 m
ν	0.33		r_i	0.0048 m
ω	10300 rad/s		r_o	0.0686 m
	Material Property		Designed Property	
Region	Equation	Evaluated	Equation	Evaluated
Blade	$\frac{\sigma_u}{\rho}$	$2 * 10^5$ m^2/s^2	$\frac{\omega^2(r_t^2 - r_h^2)}{2}$	$0.68 * 10^5$ m^2/s^2
Radial	$\frac{\sigma_u}{\rho(3+\nu)}$	$0.6 * 10^5$ m^2/s^2	$\frac{\omega^2}{16}(r_o - r_i)^2$	$0.31 * 10^5$ m^2/s^2
Tangential	$\frac{\sigma_u}{\rho(3+\nu)}$	$0.6 * 10^5$ m^2/s^2	$\left(\frac{\omega r_o}{2}\right)^2$	$1.24 * 10^5$ m^2/s^2

2.1.5 Relevant Design Considerations.

While the research into improving compressor performance is vast, three primary regions of interest appeared to have a strong likelihood of affecting compressor design. The first region is the effects of tip clearance on compressor efficiency (Section 2.1.5.1). This is of interest because the accuracy of many AM machines is significantly lower than CNC 5-axis milling machines typically used in compressor fabrication. The lower accuracy leads to designs with larger tip clearances. The second region of interest in the surface roughness effects on compressor efficiency and stall (Section 2.1.5.2). Because AM methods all deposit material in layers, surface roughness tends to be significantly higher in the build direction rather than the build plane. The

final region of interest is the expected temperature boundaries on the surface of the compressor (Section 2.1.5.3).

2.1.5.1 Tip Clearance.

Some clearance between the compressor blades and the shroud is required in order to allow for the smooth rotation of the impeller. Too small of a tip clearance will lead to blade impingement on the surface of the shroud as the compressor rapidly spins and loads the blades. If the materials have similar hardness values, the blades can dig into the shroud, leading to broken blades and a sudden stopping of the compressor rotor. However, too much of a tip clearance will allow high pressure air post-compressor to flow upstream. This high pressure air will mix with the low pressure air, leading to large losses [2]. Tip clearance is commonly nondimensionalized into the relative tip clearance ratio, shown in Equation 39. t is the distance between the tip of the blade to the surface of the shroud, and r_t is the distance from the center of rotation to the blade tip [30].

$$c_t = \frac{t}{t + r_t} \tag{39}$$

The relatively constant tip clearances in axial compressors allows a simple empirical equation to be used to model tip clearances. These tip clearance losses are modeled as a drag term (c_{D_t}) and are dependent on the tip clearance, the blade height, and the lift coefficient of the blade. This is shown in Equation 40 [4].

$$c_{D_t} = \frac{0.29t}{r_t - r_h} c_L^{3/2} \tag{40}$$

A common empirical relationship between tip clearance and efficiency drop for a centrifugal compressor is shown in Equation 41. This equation states that the relative

drop in efficiency is a function of the average relative tip clearances at the entrance and exit of the compressor, and a constant, a [30].

$$-\frac{\Delta\eta}{\eta_o} = \frac{a}{2}(c_{t,i} + c_{t,e}) \tag{41}$$

Equation 41 is a deceptively simple equation, suggesting that the losses can easily be modelled knowing the tip clearances and the constant. However, this constant is highly variable, as shown in Figure 15. For each compressor, the slope is relatively constant within a compressor but varies from $a = 1.05$ to $a = 0.2$ between different compressors. No single parameter explains the variation in tip losses. However, many parameters provide insight into the varying effects of tip clearances. Higher mass flow rates tend to have higher tip clearance effects [31]. Specific speed does not correlate to a. Blade height is negatively correlated to a, but with a low R^2 of 0.33. Diffusion ratio is positively correlated to a, $R^2 = 0.48$. Finally, blade number is positively correlated to a, with $R^2 = 0.2$ [30].

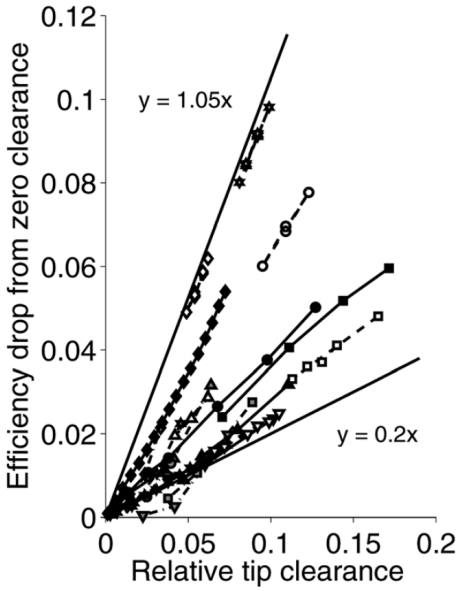

Figure 15. Change in Compressor Tip Losses for Various Compressors. [30]

The tip clearance effect becomes increasing prevalent as the compressor is dimensionally scaled down. This is because the effect is predicted from the relative tip clearance but manufacturing methods tend to have a fixed accuracy, making the tip clearance a larger percentage of the vane [32].

2.1.5.2 Surface Roughness.

A fluid flowing over a surface will always impart some viscous drag on the surface. This viscous drag is due to the no-slip condition at the wall and is dependent on the local velocity gradient at the wall and the viscosity of the fluid. There is a region close to the surface in which the velocity profile is linear called the viscous sublayer [12]. Modelling a surface with a viscous sublayer demands that there are no microstructures at the same scale as the sublayer.

Research into surface roughness has been closely tied with correlation related to the roughness of a grain of sand; one common unit describing surface roughness is the equivalent sand grain roughness, k_s. To determine the primary mechanism of surface drag, a roughness Reynolds number is defined in Equation 42 as the ratio of roughness forces to viscous forces, with u_τ being the friction velocity. Like the aerodynamic Re, Re_k is split into three regions. From 0-5, the surface is considered "perfectly smooth" and the effects of any roughness can be ignored. From 5-70, the surface is "transitionally rough." In this regime, the effects of roughness are present, but so are the viscous effects. An Re_k greater than 70 implies that the surface is "fully rough." In this region, the viscous sublayer has complete disappeared. This is because the size of the viscous sublayer is smaller than the roughness elements and never develops. Rather than viscous drag, the source of drag is now pressure drag as the fluid particles impart their momentum to the roughness elements [33].

$$Re_k = \frac{u_\tau k_s}{\nu} = \frac{\text{Roughness Forces}}{\text{Viscous Forces}} \tag{42}$$

There are slight modifications to the roughness analysis when applied to compressors. Re_k changes to include the inlet relative velocity (V_1R), shown in Equation 43. The transition number changes from 70 to 90; any Re_k greater than 90 is considered rough. A proposed relationship describing the peak change in efficiency in centrifugal compressors is shown in Equation 44, with Ra_w being the weight average physical roughness, and b_2 being the exit width of the impeller [34]. A relationship between k_s and Ra is shown in Equation 45 [35].

$$Re_k = \frac{k_s V_{1R}}{\nu_1} \tag{43}$$

$$\Delta\eta_{peak} = 0.0570963 \log_{10} \frac{Ra_w}{b_2} + 0.0322204 \tag{44}$$

$$Ra = \frac{k_s}{11.03} \tag{45}$$

While measuring the surface roughness of a complex shape could prove difficult, an expression for the surface roughness, Ra, of extruded plastic parts is shown in the three equations below, with roughness and thickness in the same units of length. From angles between 0° (vertical) and 70°, Equation 46 applies. From 70° and 90° (horizontal), the roughness is a linear approximation between the roughness at 70° and 90°, shown in Equation 47. For a flat surface, the roughness was approximated as connected hemispheres, shown in Equation 48. Finally, the back surface was corrected from the original roughness by multiplying by 1.2. This is shown in Equation 49.

$$Ra = 0.082 \frac{t}{\cos\theta} \; for \; 0° \leq \theta < 70° \tag{46}$$

$$Ra = (0.68 - 0.127\theta)t \; for \; 70^\circ \leq \theta < 90^\circ \tag{47}$$

$$Ra = 0.1125t \; for \; \theta = 90^\circ \tag{48}$$

$$Ra = 1.2Ra_{0-90^\circ} \; for \; \theta > 90^\circ \tag{49}$$

2.1.5.3 Temperature Boundaries.

The temperature rise due to the compression of the air can be found by rearranging the isentropic efficiency calculated in Equation 30. By assuming an efficiency typical of the P400 centrifugal compressor ($\cong$ 70-90%), a temperature rise can be determined. This is shown in Equation 50. However, the total temperature is not as indicative of the surface temperatures compared to the static temperature. Using the isentropic relationship between the total and static temperatures converts Equation 50 into Equation 51.

$$T_{t,e} = T_{t,i}\left(\frac{\pi_c^{(\gamma-1)/\gamma} - 1}{\eta_c} + 1\right) \tag{50}$$

$$T_{s,e} = T_{t,i}\left(\frac{\pi_c^{(\gamma-1)/\gamma} - 1}{\eta_c} + 1\right)\left(1 + \frac{\gamma - 1}{2}Ma_e^2\right)^{-1} \tag{51}$$

Plotting the static exit temperature as a function of Ma for a variety of pressure ratios and efficiencies leads to Figure 16. While the pressure ratio can be determined and the efficiency calculated to some accuracy, the exit Ma is highly uncertain. This leads to differences between T_t and T_s of up to 120 K. For the JetCat P400 compressor, static exit temperatures range between 360-487 K. As expected, increasing the pressure ratio or decreasing the efficiency both lead to an increase in the exit temperature. For this range of π_c and η_c, raising the pressure ratio by 0.3 has the same effect as a 10% decrease in efficiency on exit temperature.

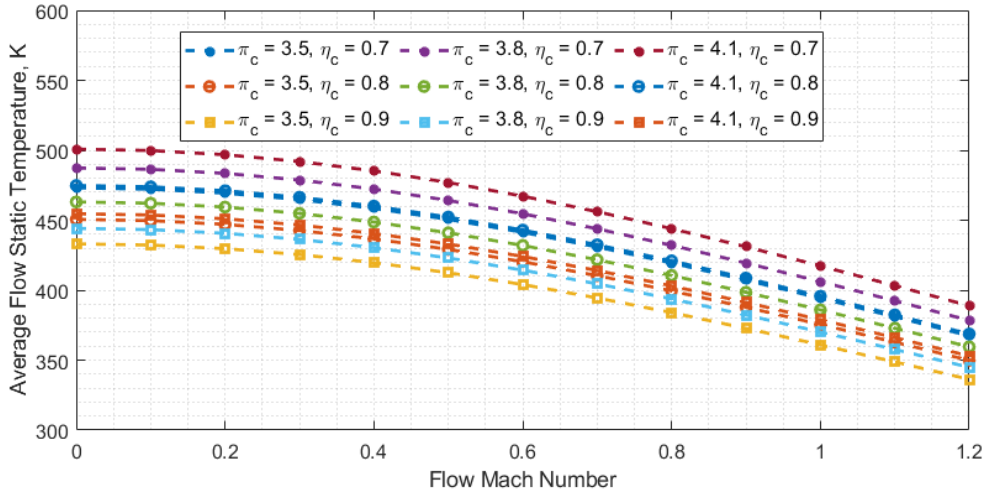

Figure 16. Estimated Static Exit Temperature.

However, because $Ma = \sqrt{\gamma RT_s}$, Equation 51 can be further reduced to Equation 52, assuming $\gamma = 1.4$ and $R = 287$ J/(kgK). Using a pressure ratio of 3.8, a slip factor of 0.6 (from Equation 28 and Table 3), an exit velocity of 729 m/s, an efficiency of 72%, and an incoming air temperature of 293 K, the predicted average static temperature is $\cong$ 400 K.

$$T_{s3}^2 + \left[\frac{v^2}{2009} - T_{t2}\left(\frac{\pi_c^{2/7} - 1}{\eta_c} + 1\right)\right] T_{s3} = T_{s3}^2 + AT_{s3} = 0 \rightarrow T_{s3} = -A \tag{52}$$

A FEA model presented in Japikse [2], shown in Figure 17, provided a temperature distribution map of a centrifugal compressor. However, the characteristics of the centrifugal compressor were not given, and the caveat, "the boundary conditions on the back-face are quite difficult to specify." However, the peak temperature falls within the previous range at 444 K [2].

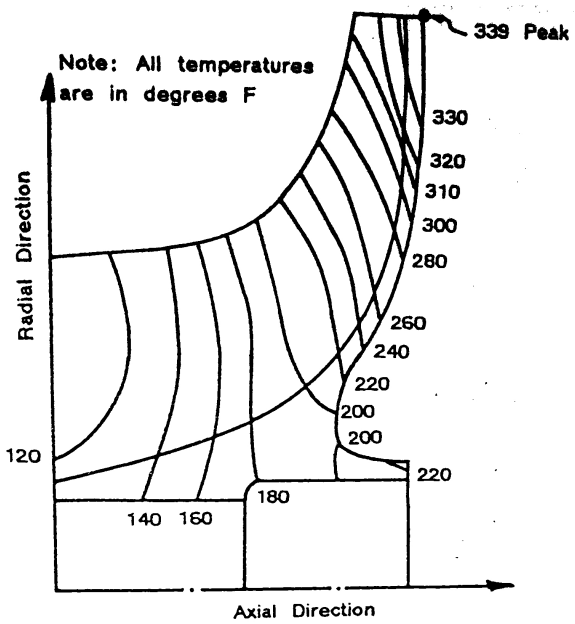

Figure 17. Temperature Distribution for FEA Model [2].

2.1.6 Trends in Small Centrifugal Compressor Performance.

From [16], the compressor efficiency as a function of absolute flow rate and pressure ratio for a multitude of compressors is shown in Figure 18. The Jetcat P400 published operating pressure and mass flow rate is designated with the star [10]. Two notable efficiency trends are demonstrated in this figure. The first is that increasing the pressure while holding the mass flow rate constant decreases the efficiency, while increasing mass flow rate holding the pressure ratio constant improves the efficiency. The second trend is that the maximum achievable efficiency drops with increasing pressure ratio, regardless of flow rate.

The compressor performance map is a plot relating the pressure ratio, mass flow rate, operating speeds, and efficiencies of a single compressor. The compressor map for the GTX5008R is shown in Figure 19. This map shows the operating region of the compressor [6]. The bottom bound is the only soft limit; below this speed, the compressor performance and efficiency is too small to include. The top bound is the maximum safe speed of the compressor. For this compressor, the maximum speed

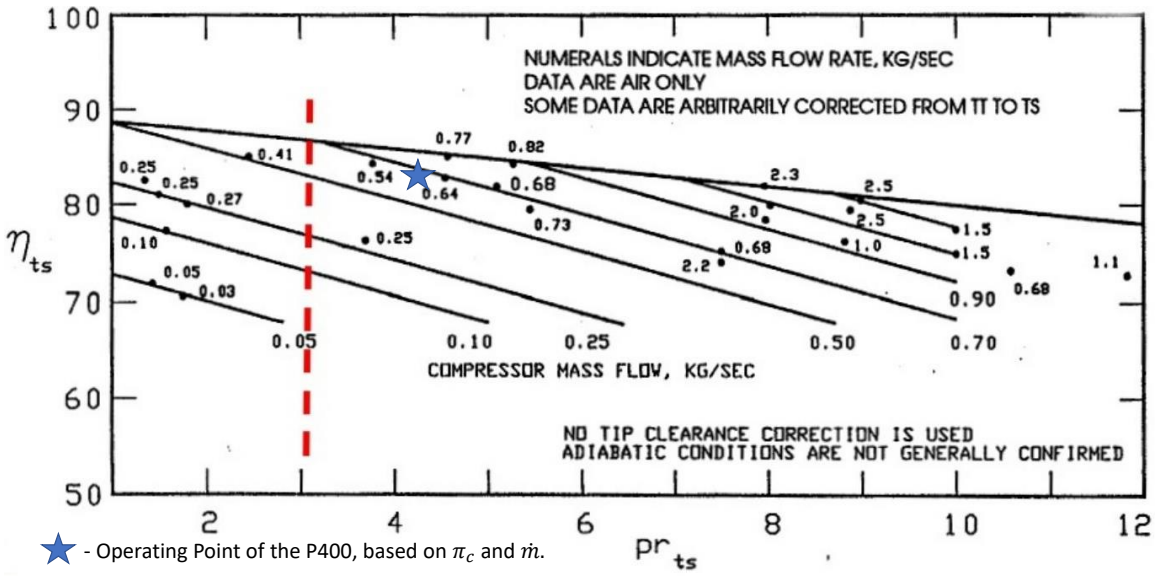

Figure 18. Centrifugal Compressor Pressure Ratio vs. Efficiency at Various Flow Rates. P400 Data Overlaid. Dashed Line Demonstrates Decreasing η_c with decreasing $\dot{m}$. [10, 16]

is 100 kRPM. Exceeding this speed will lead to compressor failure. The two other bounds are limited by the aerodynamics of the blades. The maximum mass flow rate is controlled by the choking of either the throat of the inducer or the throat of the impeller. The inducer choked mass flow rate is independent of rotational speed while the maximum mass flow rate of the impeller increases with U_t^8 [4]. The left bound is controlled by a phenomena known as surge. Surge occurs when too high of a pressure ratio is forced on too small of a mass flow rate. The high relative angle leads to blade stalling. Surge in a centrifugal compressor is due to the Coriolis forces present when turning the flow from axial to radial. These forces detach the flow, leading to blade stall. The sudden loss of pressure generation produces a reverse-flow situation [2]. The reverse flow drops the pressure ratio, allowing mass to begin flowing back into the compressor, where the buildup of mass leads to a subsequent stall. This effect repeats until the mass flow is allowed to increase or else a catastrophic failure can occur [4].

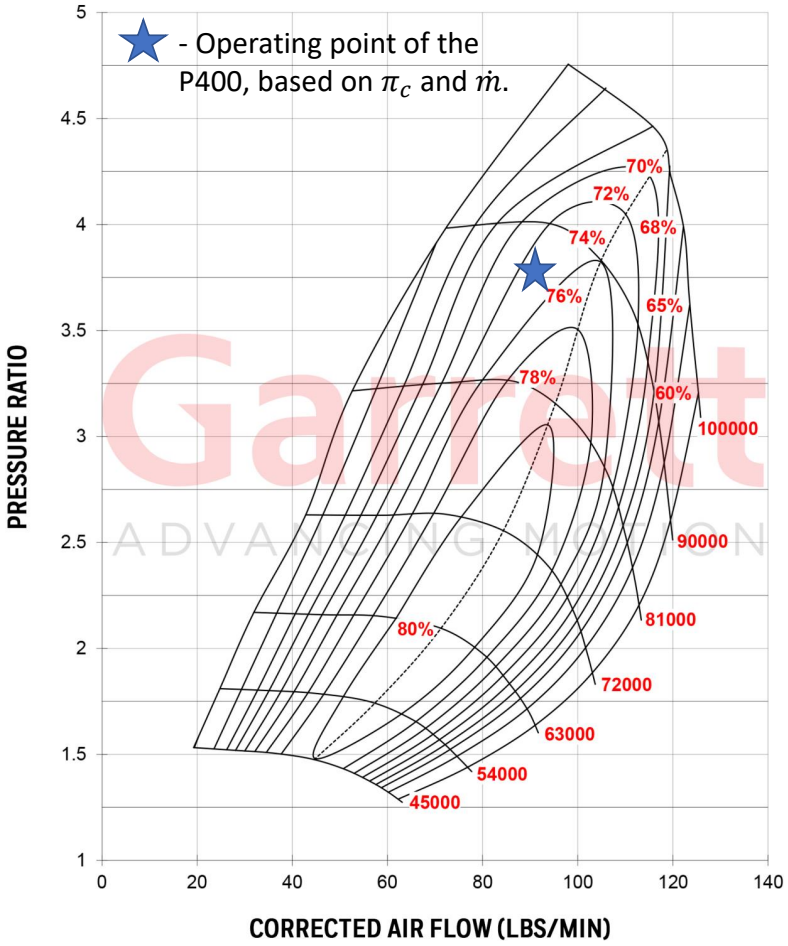

Figure 19. Compressor Map for GTX5008R. P400 Data Overlaid [10, 11].

Grannan et. al. [36] suggests that the results of testing a micro-gas turbine compressor can be overlaid on top of a similar turbocharger compressor map, shown in Figure 20. If the geometry and operating conditions are similar, results regarding relative efficiency can be reached. The JetCat P400 compressor is remarkably similar to automotive turbocharger compressors. This is considered beneficial because there is a large body of supporting work regarding the performance, safety, and production of these compressors. However, by using a compressor designed for a lower pressure ratio and mass flow rate, the P400 operates on the outer edge of the compressor map for its full thrust performance. The outer edge corresponds to significantly lower efficiency than peak efficiency of this compressor size, 72% versus a maximum of 85%,

as seen in Figure 18. A more desirable compressor would have a long, thin compressor map that shifts the peak efficiency towards the operating conditions [36]

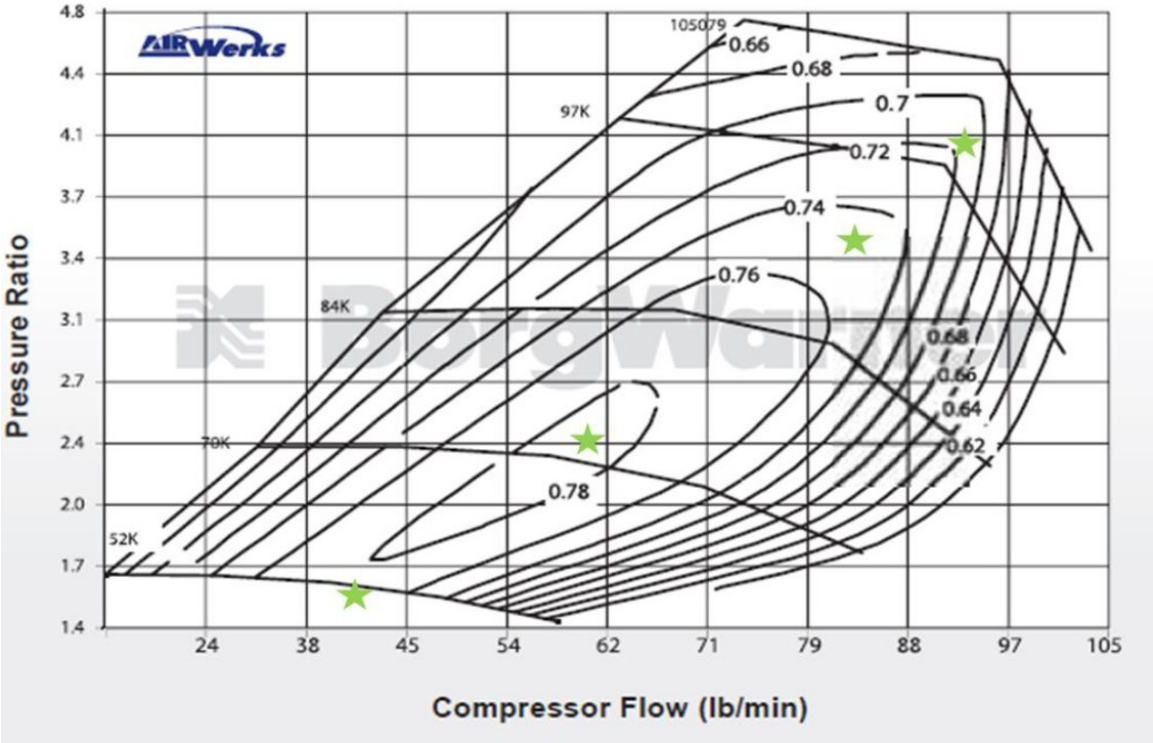

Figure 20. P400 Operating Line Overlaid on S400SX3 Compressor Map [36].

2.1.7 Additively-Manufactured Compressor Research.

One notable instance of plastic compressors in turbine engines is the Rolls-Royce RB162. This engine was built in the 1960s to supply power to a vertical-takeoff and landing aircraft. This engine used a glass-fiber reinforce epoxy-polymer composite. Typical expected air temperatures were around 420 K [37].

A mixed axial-centrifugal compressor has been built for a small (200 mm diameter) jet engine. This engine was limited to low speeds of around 7,200 RPM before material rupture was a concern. This work was supported by a team of undergraduate students as part of their senior capstone for three years [38]. Also, impellers have been built

out of plastic for moving fluids, displaying significant savings in cost and time to manufacture [39].

A metal AM vaned diffusor was produced at Purdue in 2019 [40]. This research was completed primarily to demonstrate the ability of AM to decrease design cycle time and total manufacturing cost. Additionally, integrated sensor ports were designed directly into the diffusor to minimize the effects of data collection on the flow [40].

Axial compressors have been printed using the many metal-AM processes. One such compressor was only able to reach 25,000 RPM before structural concerns were reached. This research was focused on the aerodynamic design of the compressor with the structural capability secondary [41].

Finally, impellers have been produced using metal AM methods. A Ti-Al6-V4 impeller was additively-manufactured. The purpose of this research was to produce a lattice compressor to drastically reduce the weight. This topological optimization produced a lighter, stronger compressor out of titanium. The residual stresses due to the cooling metal was corrected in order to print a compressor that shrunk to the desired dimensions [42]. More research using topological optimization produced a working impeller that decreased the experienced stresses by around 30% of the baseline design [43].

From a thorough investigation of AIAA, ASME, Elsevier, and Springer published works, a substitute gas turbine engine compressor from a lightweight plastic capable of full-range operations has not been attempted. This research, if successfully completed, will fill in a void that has prevented compressor design from progressing quickly. The decrease in cost associated with plastics and the decrease in design cycle time associated with AM technology will aid in novel compressor designs.

2.2 Materials

While aerodynamics are a huge part in what makes a compressor build a success, it cannot fully be successful if the operating speed is limited by the materials. As a large part of this research was to use AM technology to create a compressor, Section 2.2.1 covers the seven primary types of additive manufacturing. From this Section 2.2.2 compares viable material candidates with a focus on specific strength, thermal capability, cost, and build time. Finally, Section 2.2.3 covers the published standard regarding material tensile testing.

2.2.1 Additive Manufacturing Methods.

Additive manufacturing is the term used for the collection of manufacturing methods that take a Three-Dimensional (3D), Computer Aided Design (CAD) and fabricates it by the addition of Two-Dimensional (2D) cross-sections of a finite thickness. AM is often contrasted to conventional, or subtractive, manufacturing methods. Gibson [1] lists six comparisons between AM and CNC machining summarized below. 1.) The available materials is more limited than CNC machining methods. While CNC can be used on almost every material to some extent, AM can only be used on favorable materials such as thermoplastics with certain thermal and viscous properties, metals with the ability to be ground ultra-fine, or curable materials. 2.) AM processes typically add material slower than CNC machining methods can remove the same amount of material. However, the entire design-program-build loop is much quicker for AM than CNC machining. Additionally, the speed of AM if dependent almost exclusively on volume versus the dependence on complexity of the build displayed by CNC machining. 3.) AM methods can easily produce much more complex objects than CNC machining. Hollow, twisting cooling passages for turbines are a prime example. 4.) The comparison of the accuracy of the build is dependent on the

method used. While hobby-level printers commonly display the distinct build-layer lines, the higher quality printers have resolutions the diameter of a fine laser. 5.) Geometric complexity does not limit most AM prints. While large overhangs, hollow sections, and sharp internal corners can be difficult for CNC machining, there is no increase in AM difficulty. 6.) Programming a CNC machine is a highly-involved task, taking tens of hours of skilled labor to ensure the part will be created correctly without wrecking the part or the machine. AM printers typically have only a few settings and incorrectly selecting them will only leave a poor print and a small mess [1].

The standard axis definitions for AM technologies is shown in Figure 21. The XY plane is the build platform and the Z-direction is vertical. As mentioned before, AM works by stacking 2D cuts of a model until the final product is achieved. The 2D cut is produced in the XY build plane and the thickness is in the Z-direction out of the build plane. After the XY layer is laid down, the next layer is produced vertically adjacent to it; this is repeated until the final model is made. Because of the anisotropy associated with AM, different build directions demonstrate varying material properties. This leads to the requirement that the build direction is defined when describing a print. The three common methods of describing a print are shown by the test specimens in Figure 21. AM material properties are typically published in the ZX and XZ direction to demonstrate the bounds of the material strength [44].

While the general idea encapsulating AM is just laying down one layer of material at a time until the final product is formed, there are a vast array of complex methods to achieve this idea. The ASTM F42 Committe on Additive Manufacturing Technologies classifies all types of AM under seven categories. These are 1.) Sheet Lamination, 2.) Binder Jetting, 3.) Material Jetting, 4.) Directed Energy Deposition, 5.) Powder Bed Fusion, 6.) Vat Photopolymerization, and 7.) Material Extrusion. Each method

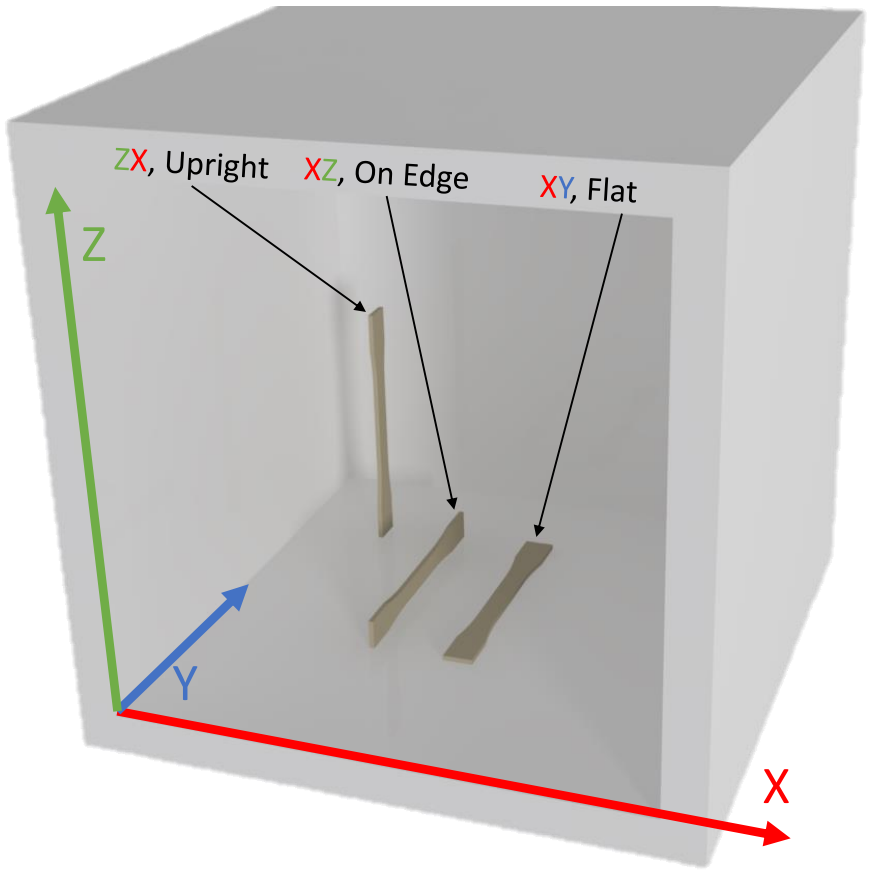

Figure 21. Common Axis Definitions and Build Directions

has a collection of positive and negative aspects that can make one method more suited than another for specific applications. Additionally, the materials available to each method vary greatly and even the mechanical properties of the same material can vary greatly between methods.

2.2.1.1 Sheet Lamination.

Sheet lamination is a process that stacks 2D sections of a material and adheres each layer together at once, shown in Figure 22a. The fours steps to the form-then-bond process are 1.) Positioning the material onto the build plate. 2.) The 2D cross section is cut out from the layer of material, commonly with a laser or a knife. 3.) The cut cross section is bonded to the previous layer. 4.) The next layer of

material is laid on top and the process is repeated [45]. The bond-then-form version of sheet lamination switches steps 2.) and 3.). Typical materials are papers (such as the vase in Figure 22b), thermoplastics, and some metals. Bonding is achieved with an adhesive, thermal bonding, clamping, or ultrasonic welding [1]. There are two notable benefits of this method. The first is the increased speed as each print layer depends only on the circumferential cutting rather than the area. The second is the low cost of materials, primarily due to the limit in available materials. The negative aspects of sheet lamination are the lower surface finish and, as mentioned before, the limited material available [45]. While this is one of the older AM processes, it is still relatively primitive in comparison to the other methods.

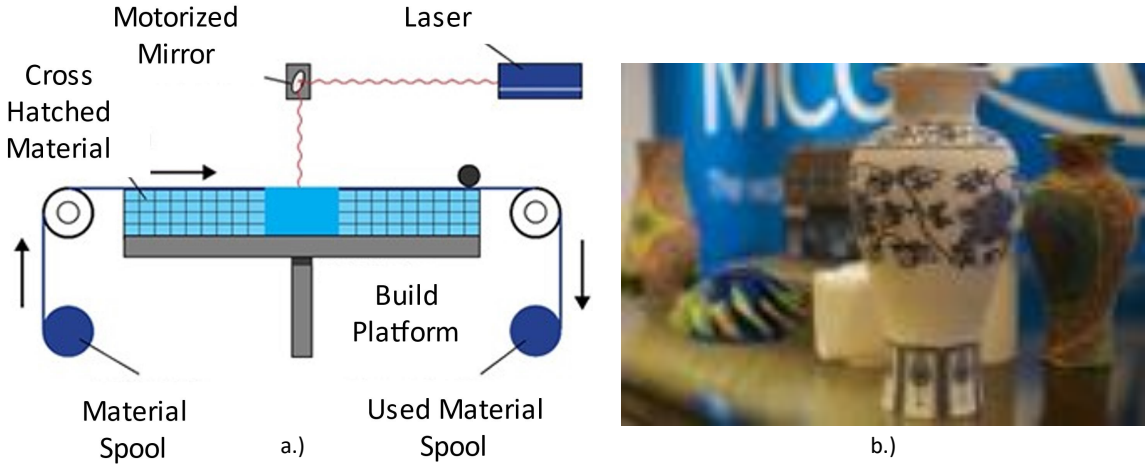

Figure 22. Sheet Lamination. a.) Graphical Depiction [45]. b.) Colorful Printed Paper Vases [46].

2.2.1.2 Binder Jetting.

Binder jetting is the process of jetting a binder onto a layer of powder. By selectively jetting the binder, a cross section can be created. This is shown in Figure 23a. There are three steps to binder jetting. 1.) A roller spreads out a thin layer of powder onto the build platform. 2.) The print head passes over, selectively jetting binder onto the powder in the locations determined by the 2D cross section. 3.) The build

platform is lowered and the process repeats [45]. The part is usually left undisturbed for the binder to fully set. For metal prints, the part is either sintered to melt the metal together and remove the binder or is impregnated with a lower-melting point metal. Because this process uses a binder, essentially all materials that can be finely ground can be used for printing. Materials of interest are metals, ceramics, glasses, wax, and polymers [1]. The largest advantages to this process is the speed, available materials, and the range of print settings. Because each layer is bonded with a single pass of the print head, the print speed primarily depends on the length of the part. The variety of print materials allows a near-infinite number of combinations to be obtained with a variety of material properties. The range of colors allows objects such as the spheres shown in Figure 23b. However, the binder severely limits the application of this method to any use besides cosmetic prints and the additional cure time can increase both the downtime of the machine and the length to build each part [45].

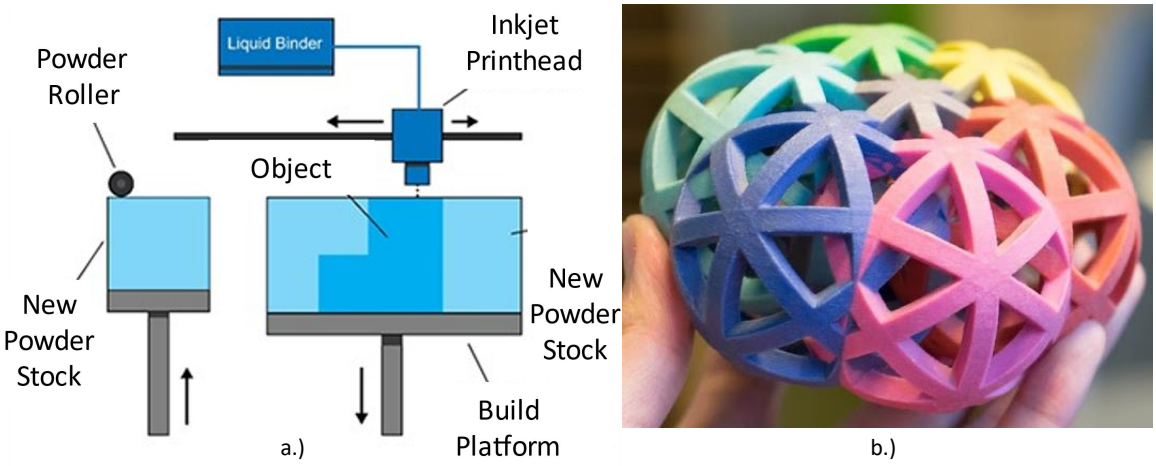

Figure 23. Binder Jetting. a.) Graphical Depiction [45]. b.) Multicolored, Interlocked Spheres [47].

2.2.1.3 Material Jetting.

Material jetting is a similar process to binder jetting except the binder acts as the material and is typically cured after each pass with an ultraviolet (UV) light. The process follows the position-deposit-solidify method seen in binder jetting [45]. The four common ways of depositing the material are deposit-cure, melt-deposit-harden, strain-deposit-harden, and suspend-deposit-evaporate. Deposit-cure jets a UV-curable material and follows with a UV light, shown in Figure 24a. Melt-deposit-harden melts the material, such as wax, and the material hardens on the previous layer. Strain-deposit-harden relies on shear-thinning Bingham plastics that flow easily under high stress. When this stress is removed upon deposition, the material thickens significantly. Finally, the suspend-deposit-evaporate method suspends particles of the material, such as ceramics or metals, in a liquid, such as methylated spirits, deposits the suspension onto the build platform and allows the liquid to evaporate off [1]. The two primary advantages are the incredibly high accuracy in comparison to the other methods and the large, intense range of colors, seen in Figure 24b [45]. The disadvantages are the material limits and the required support material.

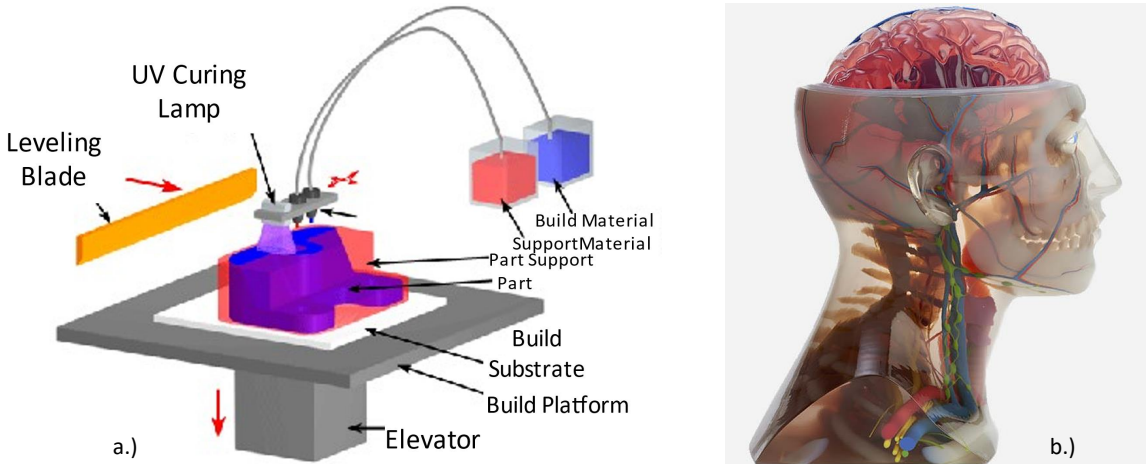

Figure 24. Material Jetting. a.) Graphical Depiction [45]. b.) Full-Color, 3D Model of Human Head Anatomy [48].

2.2.1.4 Direct Energy Deposition.

Direct energy deposition (DED) is less commonly used to produce virgin objects. Rather, it is used to repair or modify already produced objects. This process deposits material by either intersecting a metal wire or powder with a laser or electron beam. This directed energy source quickly heats the material beyond its melting point and the material is deposited onto the build surface [45]. This process is depicted in Figure 25a. Although commonly used with metals, polymers and ceramics can be printed using this method. Despite this process's similarity to a CNC welder, the application is usually for more complicated shapes than simply joining two sections of metal together. By controlling the amount of energy imparted into the material, both the microstructure and the layer adhesion can be controlled. An additional benefit to this method is that build speed can be sacrificed in order to achieve more accurate and ideal microstructure. Drawbacks are the limited materials and the low surface quality of the final build [1]. The DED process is shown with a powder deposition in Figure 25b.

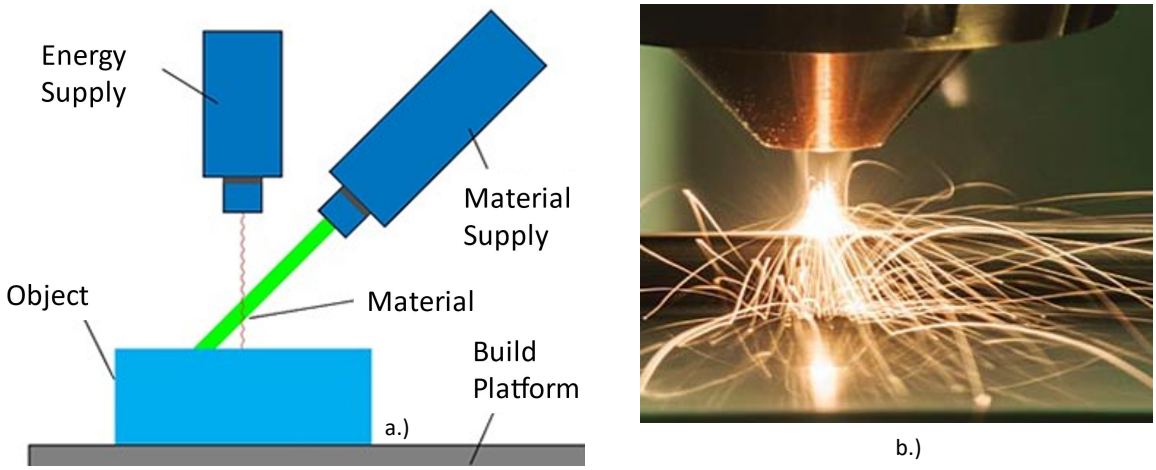

Figure 25. Directed Energy Deposition. a.) Graphical Depiction [45]. b.) Metal Deposition Using DED [49].

2.2.1.5 Powder Bed Fusion.

Powder bed fusion (PBF) is similar to the binder jetting process. Rather than jetting a binder, a laser is used to melt the powder into coherent shapes. After melting the powder layer, the build layer lowers and a roller deposits fresh powder on top of the model. This is shown in Figure 26a. By preheating the entire build region, the thermal warping can be minimized as it takes less energy to melt the powder and the object will only cool a smaller amount before the subsequent layer is deposited. Common materials are thermoplastics, ceramics, and weldable metals. Aluminum is typically difficult to process due to the quickly forming oxide layer, but can be printed by holding the powder in an inert gas during processing. After fusion, the part is commonly sintered to decrease the porosity of the microstructure. By holding the parts just beneath their melting temperature, the drive to minimize the free energy creates regions with a minimized surface area to volume ratio [1]. The benefits of this method are the lower costs relative to CNC machining parts, the support structure provided by unprocessed powder, and the large range of materials available. Drawback include the significantly slower print relative to other methods, the large drop in material properties, build size limitations, high power use from both the laser and the heater, and the hazard presented by the fine particles when post-processing the build [45]. This is the method used to produce the axial compressor shown in Figure 26 [41].

2.2.1.6 Vat Photopolymerization.

Vat photopolymerization (VP) uses specific materials that are liquids until exposed to UV light. After exposing the top layer of the vat to a specific pattern of UV light, the build platform is lowered, allowing a fresh layer of photopolymer liquid to flow over the surface of the part. This process is repeated until the final part is

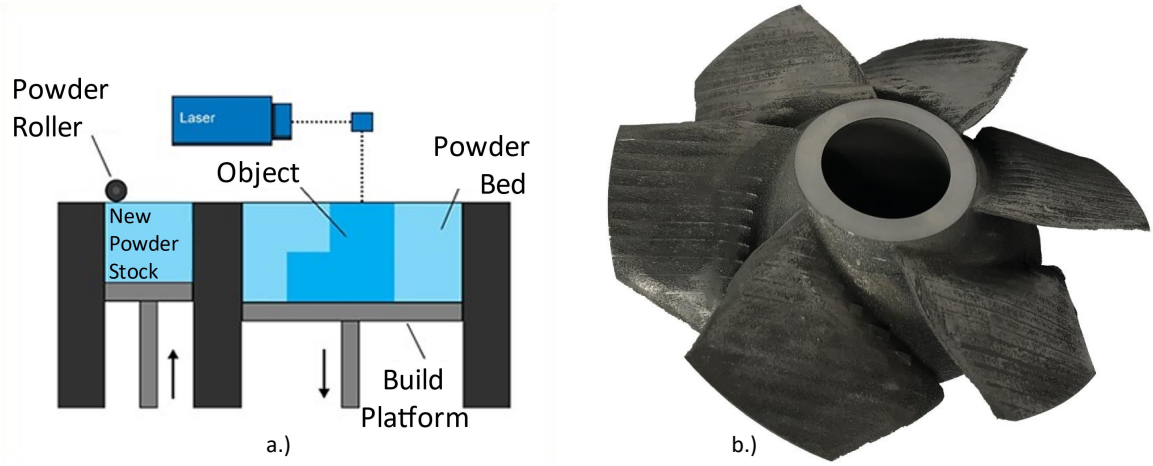

Figure 26. Powder Bed Fusion. a.) Graphical Depiction [45]. b.) Axial Compressor [41].

complete, as seen in Figure 27a [45]. Afterwards, the part is commonly put into a UV curing box to strength the print. Rather than a UV laser, a projector can be used to flash an entire layer, curing a layer simultaneously. This both significantly improves build time and aids in removing anisotropic properties from that layer. The only material that can work in this process is photo-curable polymers [1]. The advantages of this process are the speed, the high accuracy and smooth finish, and the ability to have a large build volume. Disadvantages are expensive materials, lengthy post-processing, and the requirement for support structures [45]. The compressor in Figure 27b was made using this method.

2.2.1.7 Material Extrusion.

Material extrusion (ME), commonly known as fused deposition modeling (FDM) was initially patented by Scott Crump, the founder of the Stratasys Company. [1]. Per ASTM standards, FDM is "a material extrusion process used to make thermoplastic parts through heated extrusion and deposition of materials layer by layer" [50]. Hobbyist printers typically just have one extrusion head, but more expensive, industrial-level printers have two or more extrusion heads. This makes it possible

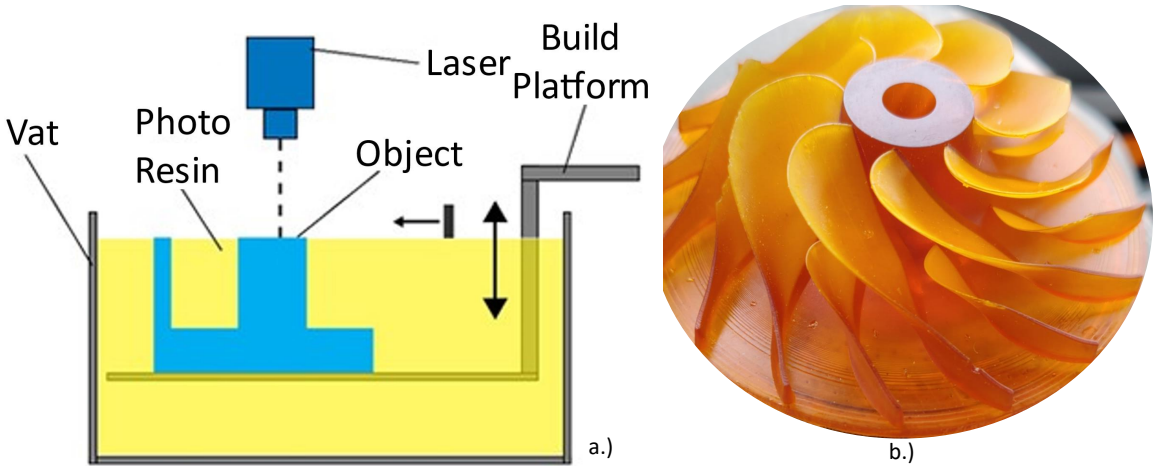

Figure 27. Vat Photopolymerization. a.) Graphical Depiction [45]. b.) Small, 3D Printed Compressor, 300-AMB.

for both a modeling material and a support material to be extruded; the support material is then able to be removed due to poor adhesion between modeling material and support material or through a chemical reaction or dissolving in a liquid.

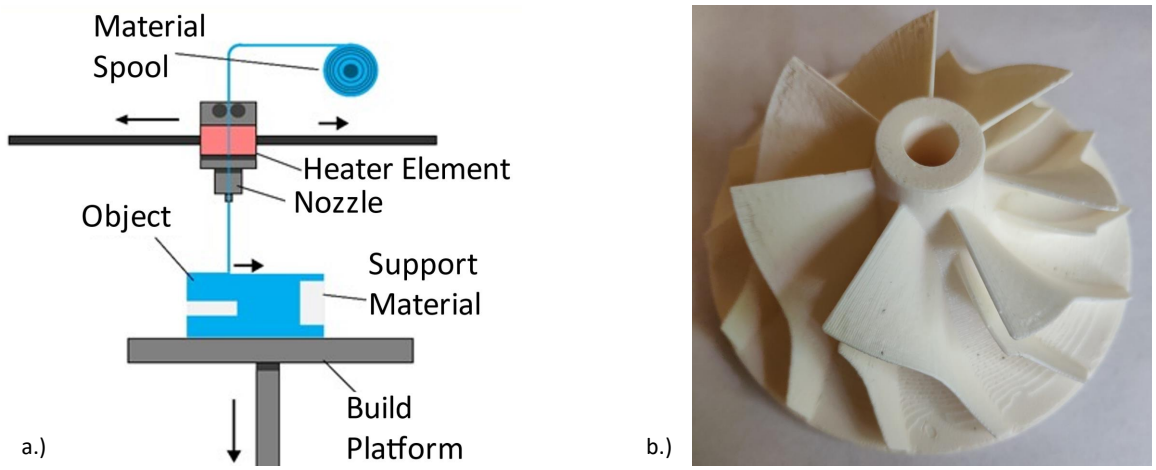

Figure 28. Material Extrusion. a.) Graphical Depiction [45]. b.) Centrifugal Compressor Printed in ABS.

A basic illustration of how material extrusion works is shown in Figure 28a. The filament, typically a thermoplastic, is pushed by driving wheels down into the extrusion head. Here, the material is heated past its glass transition temperature until it is able to flow and adhere to previous layers of the material. The pressure of the solid

filament as it is forced into the extrusion head forces the semi-liquid material out of the extrusion tip and onto the part. The extrusion head first moves parallel to the build platform to lay down a single layer of material. After the layer is complete, the head is raised to begin the subsequent layer. This process is repeated until the model is complete. Some printers, such as Stratasys' Fortus series has dual extrusion heads. This allows both the modeling material and a support material to be printed without purging material. An Acrylonitrile Butadiene Styrene (ABS) compressor shown in Figure 28b was printed on a Fortus printer.

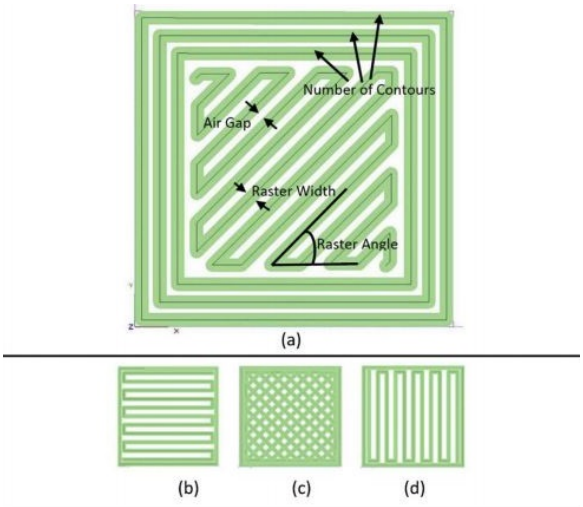

Figure 29. Material Extrusion Parameters. a.) Air Gap, Contours, Raster Width and Angle. b.) Horizontal Fill Pattern. c.) Cross-Hatch Fill Pattern. d.) Vertical Fill Pattern. [51]

FDM is typically considered the quickest, easiest, and least costly of the many types of AM. Model strength is heavily process dependent and highly anisotropic [52]. The material is strongest in the plane parallel to the print bed and significantly weaker in the vertical direction [44]. Important parameters affecting material properties are air gaps, raster orientation and angle, layer thickness, number of contours, printing speed, feed rate, build direction, and print temperature [51]. Many of these parameters are shown in Figure 29. The air gap is the space between lines of material with maximum strength occurring with a negative air gap. This means that the lines

of material overlap to some extent. While this is beneficial to strength, it can be detrimental to model accuracy. The number of contours describes how many times the layer is outlined before a rastering occurs. After the layer is contoured, a raster occurs. The raster is the quick, predefined way that the FDM machine fills in the part and can be described by the raster width and the angle. Figure 29(a-d) have raster angles of +45° 0°, ±45°, and 90°, respectively. Material extrusion is one of the strongest polymer-based AM methods [1].

2.2.2 Material Comparisons.

While a complete set of temperature-dependent properties is not available for the vast majority of all novel materials, baseline properties such as strength and modulus are commonly published with most marketable materials. In this section, material properties such as specific strength, specific stiffness, fracture toughness, maximum temperature, thermal conductivity, thermal expansion, cost, and manufacturing time are compared for a variety of materials of interest.

Three common turbomachinery metals were chosen as baselines. The Al 7075-T6 is the material used in the JetCat P400 [28]. A titanium alloy, Ti 6Al-4V, is a common, high-grade titanium used in turbomachinery [2]. The final material is Inconel 625, a nickel-steel alloy used in many turbines due to its favorable thermal properties. These materials must be either cast or CNC machined to produce compressors. The properties for these materials are sourced from MATWEB [29]. Two powder-bed fusion materials are compared, an aluminum, AlSi10Mg, and Inconel Ni 625, both sold by 3D Systems [53]. ABS and Polylactic Acid (PLA) represent the common, "hobbyist-grade" material extrusion plastics, produced by Stratasys [44]. Five "engineering-grade" material extrusion plastics are compared: two Polyetherimide (PEI) plastics, ULTEM 1010, and ULTEM 9085; a polyetheretherketone plastic,

Antero 800NA; and two chopped carbon fiber reinforced nylons, Nylon 12CF and Onyx. The first four are produced by Stratasys [44] and the Onyx is produced by Markforged [54]. Three material extrusion, continuous fiber (ME-CF) filaments are shown. Onyx-Carbon Fiber, Onyx-Kevlar, and Onyx-Fiberglass, produced by Markforged [54]. The final material analyzed was the 300-AMB photopolymer produced by 3D Systems [53].

The two most important parameters for successful compressor design are the specific strength and the thermal "resistance" of a material [2]. Figure 30 depicts the specific ultimate strength at a cold temperature versus the transition temperature. For metals, this was the melting point and for polymers, this was the glass transition temperature. The blue vertical line is the conservative estimated temperature and the red vertical line was the highest expected temperature from Section 2.1.5.3. The dashed horizontal lines depict various specific speeds, scaled $\sigma_u/\rho = C\omega^2$, as in Section 2.1.4.2. These speeds are the 100% speed, the 70% speed, and the 50% speeds. The 100% speed was placed through the Al 7075-T6 material used in the JetCat P400.

All metals were well above the "hot" line. However, only titanium had a higher specific strength than Al 7075-T6. The hobbyist plastics had both too low a specific strength and too low of a transition temperature. The engineering plastics performed better, but not on the same level as the metals. It is predicted than all of them but Onyx could get to half of the failure speed of an Al 7075-T6 compressor. Both ULTEM materials and the Onyx had adequate transition temperatures, close to or exceeding the "hot" temperature. The specific strength of the Onyx-fiber material had both adequate transition temperatures and specific strengths on par with the turbomachinery metals. This figure down-selects the range of materials to ULTEM 9085, 300-AMB, and a fiber-reinforced Onyx.

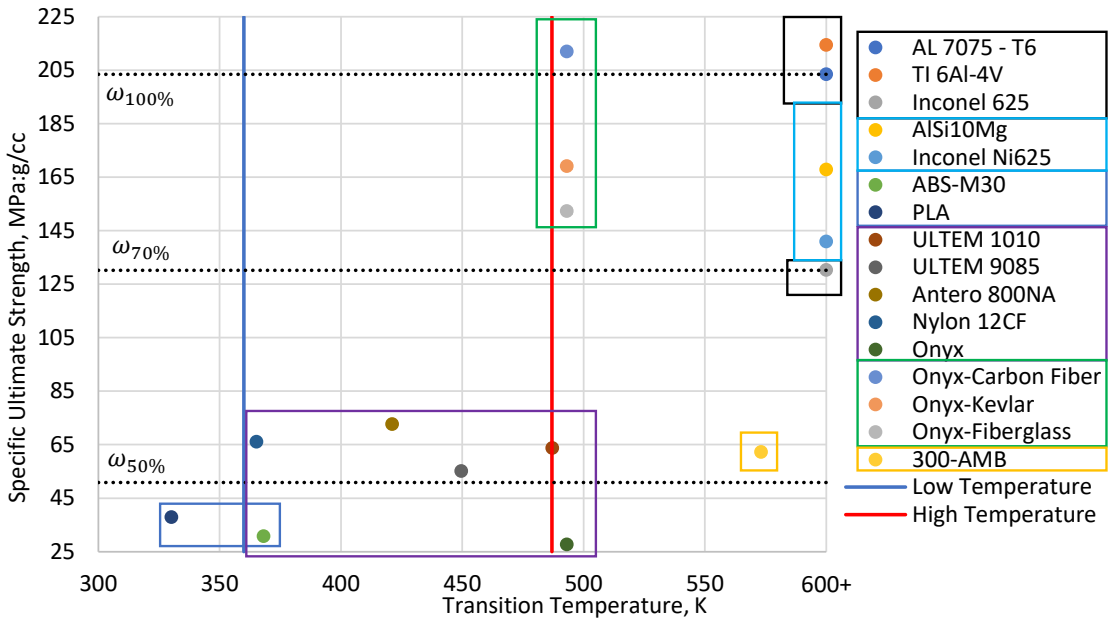

Figure 30. Specific Strength vs. Transition Temperature

Adequate specific strengths and transition temperatures would allow a compressor to be produced with AM. However, if the method cost more or took longer to complete than conventional CNC machining, AM would have to be pushed to the sidelines of research. Figure 31 depicts the cost versus time for the materials of interest. The cost is the cost to produce a single compressor. This eliminates the benefits seen from batch production and is more representative of the one-off compressors expected in research. This cost is determined either from predictions from the manufacturers [44, 53, 54] or a conversation with a trained machinist who had recently completed a one-off compressor of a similar size. The time to produce a single compressor was calculated from the acquiring of the CAD file from the skilled technician until the compressor was completed. The bottom point represents the amount of time requiring a skilled technician while the top point represents the total amount of time needed from start to finish.

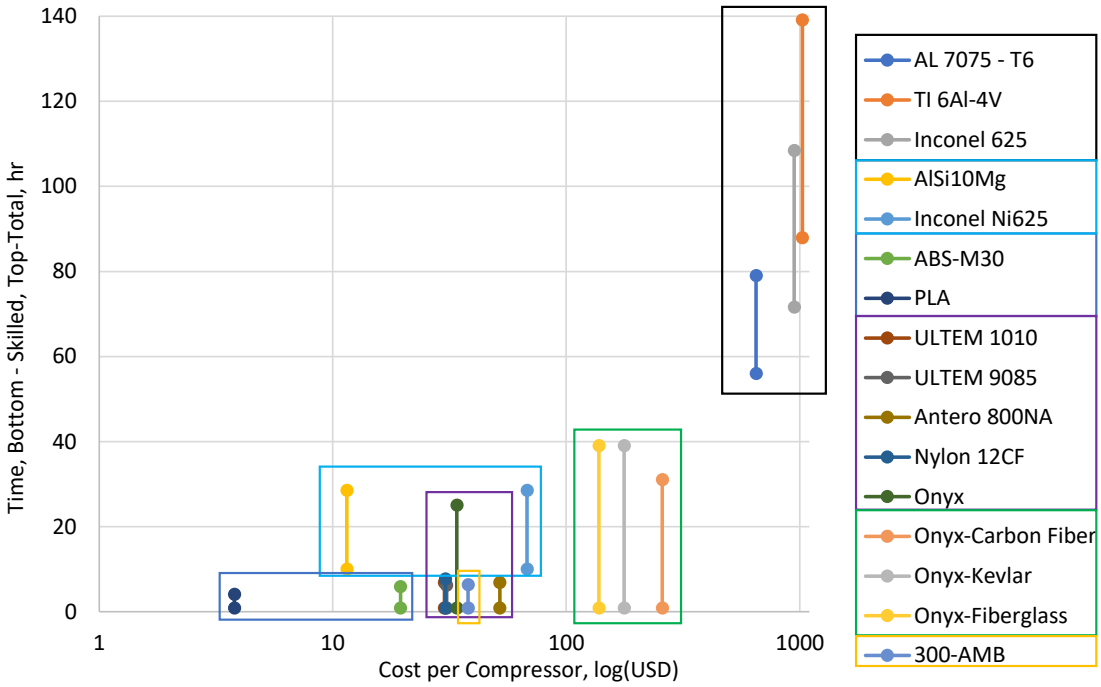

Figure 31. Cost and Time to Produce a One-off Compressor

The CNC-machined metals were both the most expensive (by 1-2 orders of magnitude) and the most time-consuming. Each method took more than an entire week of a dedicated machinist's time to program and use the CNC machine. The complexity of the programming process is what makes a one-off compressor so costly. The PBF metals needed roughly 10 hours of skilled labor, mostly in the pre- and post-processing sections. All other AM methods took less than an hour to get a compressor printing. The Stratasys and the 300-AMB took roughly five hours to print while the Markforged printer ranged from a day (pure Onyx) to 40 hours for the fiber reinforcement. While the fiber plastics were costly and time-consuming, the lack of skilled labor decreases the total cost significantly. The printer continues to produce long after the laborer has left.

Two more physical properties that are important to design are the specific stiffness and the resistance to stress concentrations. These properties are shown for the selected materials in Figure 32. Because metals and plastics respond to stress concen-

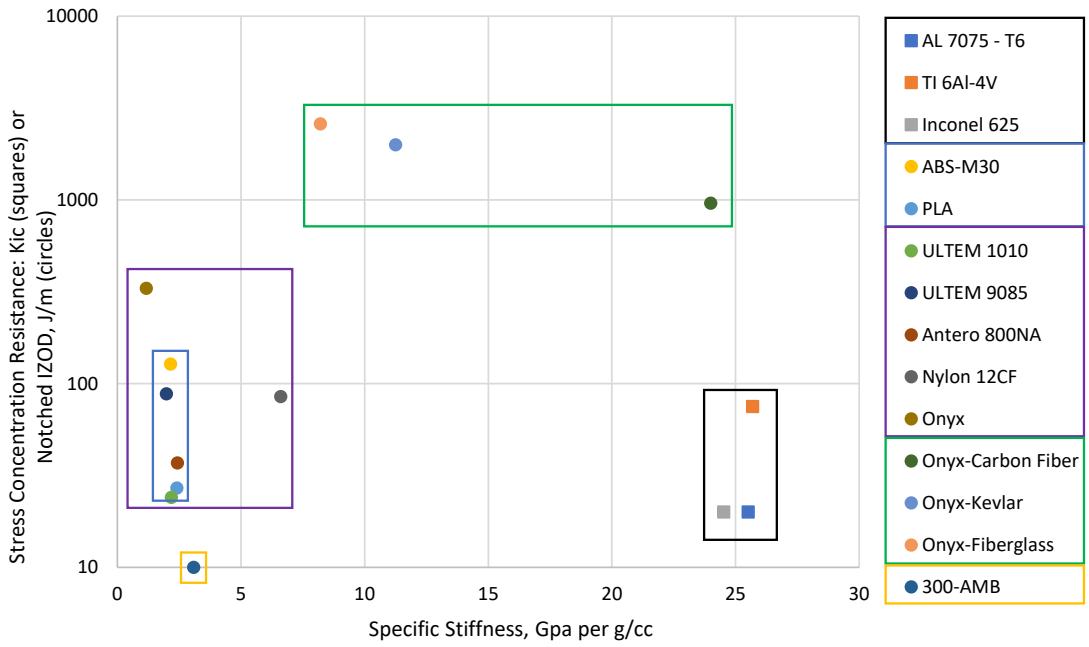

Figure 32. Specific Modulus of Elasticity versus Stress Concentration Resistance

trations differently, two distinct tests are typically performed. Metals use a K_{IC} while plastics use the IZOD impact test. While not as critical to match as specific strength, specific stiffness simplifies the redesign process as the compressor would be expected to deform similarly. The metals had a high specific strength, the pure plastics were around 10-20% of the metals, and the fiber-reinforced plastics ranged between the two.

The way the material responds to changes in temperature is summarized in Figure 33. High thermal conductivity allows more cooling to occur, conducting heat away from the compressor blade tips in to the regions cooled by oncoming air. Excessive thermal deformation would lead to higher thermal stresses and would make the FEA model less accurate. Metals have both the high thermal conductivity and the low coefficient of thermal expansion (α) desired. The engineering plastics had a lower α but lower thermal conductivity. The carbon fiber displayed a high level of ther-

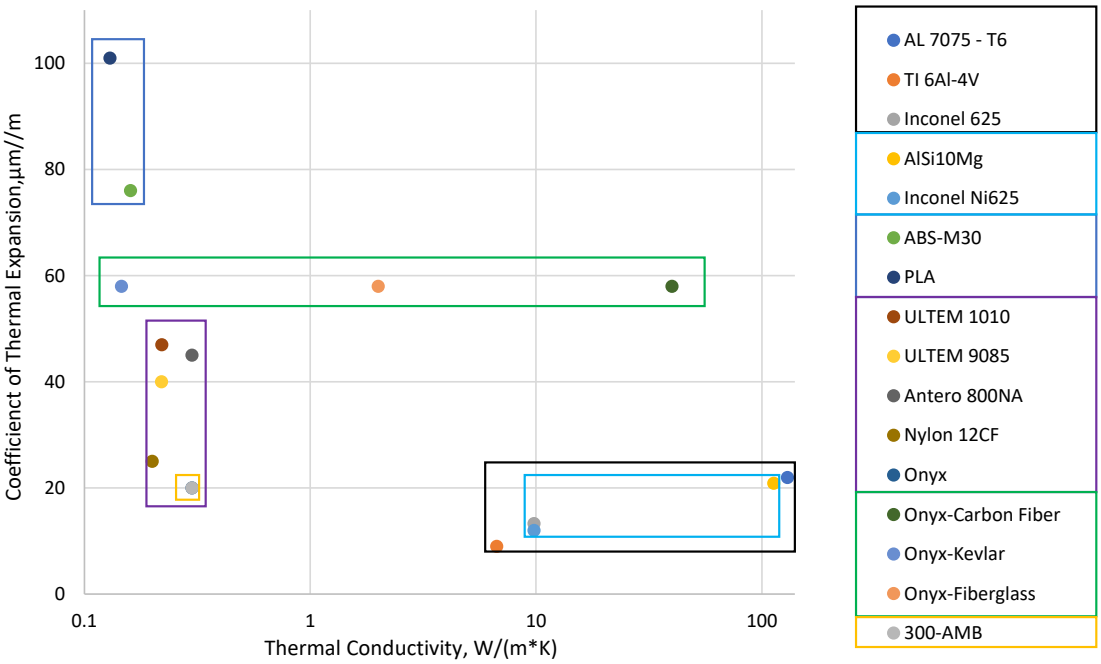

Figure 33. Thermal Conductivity versus Coefficient of Thermal Expansion

mal conductivity. However, that conductivity was only in the longitudinal direction. Conduction between layers is closer to the Onyx.

A summary of the materials' methods, manufacturers, machines, and minimum resolutions is shown in Table 5. The favorable resolution of some methods will decrease the surface roughness effects discussed in Section 2.1.5.2. This metric is how CNC currently vastly outperforms all AM methods. If 2.5 μm resolution is needed, CNC is currently the only option.

2.2.3 Material Testing.

While working with a complete set of published material properties would be preferred, there are no comprehensive sources that publish the desired material properties at numerous conditions. In order to improve the predictive FEA model, accurate material properties over a range of operating temperatures are required. The chosen materials did not have a complete set of material properties available, therefore,

Table 5. Material Method, Manufacturer, Machine, and Minimum Resolution

Material	Method	Manufacturer	Machine	Minimum Resolution, μm
AL 7075 - T6	CNC	n/a	CNC	2.54
TI 6Al-4V	CNC	n/a	CNC	2.54
Inconel 625	CNC	n/a	CNC	2.54
AlSi10Mg	PBF	3D-Systems	ProX DMP 320	10
Inconel Ni625	PBF	3D-Systems	ProX DMP 200	10
ABS-M30	ME	Stratasys	Fortus 450mc	254
PLA	ME	Stratasys	F370	254
ULTEM 1010	ME	Stratasys	Fortus 450mc	254
ULTEM 9085	ME	Stratasys	Fortus 450mc	254
Antero 800NA	ME	Stratasys	Fortus 450mc	254
Nylon 12CF	ME	Stratasys	Fortus 450mc	254
Onyx	ME	Markforged	Mark II	100
300-AMB	VP	3D-Systems	Figure 4	50
Onyx-Carbon Fiber	ME-CF	Markforged	Mark II	125
Onyx-Kevlar	ME-CF	Markforged	Mark II	100
Onyx-Fiberglass	ME-CF	Markforged	Mark II	100

tensile testing was required. The ASTM standard for testing both reinforced and unreinforced plastics is ASTM D638, Standard Test Method for Tensile Properties of Plastics [55].

Material properties vary greatly due to manufacturing and testing conditions. By limiting the variability, unnecessary errors can be prevented. Figure 34 details the required dimensions for the test specimen. The Type I specimen was chosen because it can be used to test rigid, semirigid, and reinforced plastics [55].

Because the material testing is primarily to aid in the predictive capability of the FEA model, rigid adherence to the testing is less important than completing the test. While the ASTM test standard suggests testing with five test specimens, all free of visible damage, in all anisotropic directions, relaxing these constraints would still provide usable results. If three materials at five temperatures were to be tested following ASTM 638, 225 tests would have to be performed. The displacement rate for the Type I test specimen is prescribed at 5$\pm$0.25% mm/min, with testing expected to

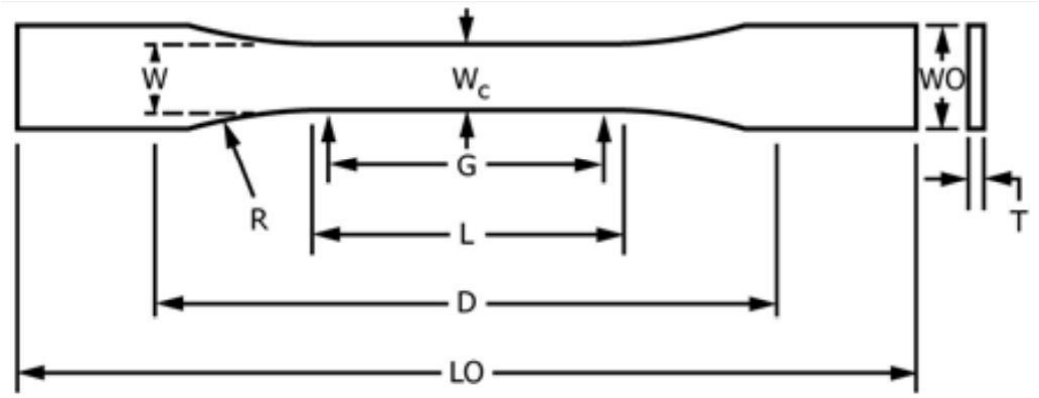

Specimen Dimensions for Thickness, *T*, mm (in.)[A]

Dimensions (see drawings)	7 (0.28) Type I	Tolerances
W—Width of narrow section[E,F]	13 (0.50)	±0.5 (±0.02)[B,C]
L—Length of narrow section	57 (2.25)	±0.5 (±0.02)[C]
WO—Width overall, min[G]	19 (0.75)	+ 6.4 (+ 0.25)
WO—Width overall, min[G]	...	+ 3.18 (+ 0.125)
LO—Length overall, min[H]	165 (6.5)	no max (no max)
G—Gage length[I]	50 (2.00)	±0.25 (±0.010)[C]
G—Gage length[I]	...	±0.13 (±0.005)
D—Distance between grips	115 (4.5)	±5 (±0.2)
R—Radius of fillet	76 (3.00)	±1 (±0.04)[C]
RO—Outer radius (Type IV)	...	±1 (±0.04)

Figure 34. ASTM 638 Tensile Specimen, Type I [55]

last between 0.5-5 minutes per specimen. The desired material properties include the yield and ultimate strengths, the modulus of elasticity, and the Poisson's ratio [55]. Although Poisson's ratio for plastics is known to typically increase with increasing temperature, the range for most metals, ceramics, and engineering plastics is between 0.25 and 0.35 [56].

2.3 Finite Element Analysis

The second goal of this research was to determine if FEA modeling could predict the failure speed of the AM-produced compressors. While FEA is commonly used

to model the failure speed, temperature profile, deformation, and even the modal response of centrifugal compressors [24], the complexities of AM decrease the validity of the FEA solutions. Because this was merely an initial look into using FEA on AM centrifugal compressors and not a research into significantly improving FEA, this section will be limited to the basic theory.

Numeric solvers including finite element analysis and computational fluid dynamics use basic laws of nature, expressed in the conservation and transfer of state variables summed up in one or more mathematical equations. These variables are properties within a region that are of some interest [57]. Some common equations already seen are the continuity equation (Equation 5), the momentum equation (Equation 6) and the energy equation (Equation 7). One common attribute in these equations is that they are in the differential form and thus, apply to every point in the domain. The balance of linear momentum leads is shown in Equation 53. This equation states that the divergence of the stresses is equal to the applied body forces. Applying boundary conditions allows highly simplified problems to be solved [58].

$$\partial_i \sigma_i + F_i = 0 \tag{53}$$

In the infinite variety of analytically unsolvable problems, an approximate solution is better than no solution at all. By dividing up the domain into a set of finite elements, a number of trial functions can be used to reach the approximate solution [58]. The set of finite elements is often referred to as the mesh due to its mesh-like appearance. The study of proper meshing is an entire subfield of research. An example mesh is shown in Figure 35. Because this mesh was adaptively generated, the size of each element was determined based on the complexity of the local geometry [28].

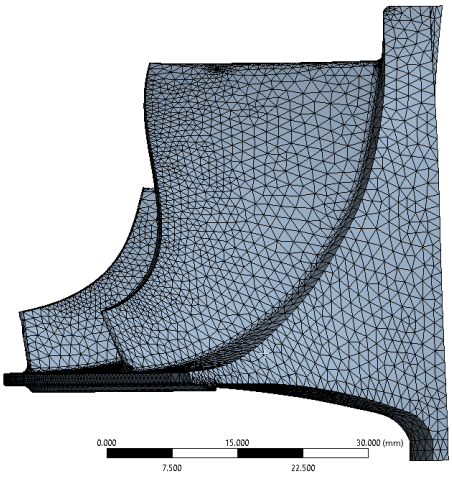

Figure 35. Example Finite Element Analysis Mesh on a Centrifugal Compressor

If this mesh is too large, it will poorly represent the physics of the problem and the solution will be errant. As the number of finite elements is increased, the grid is said to become more refined. The goal of this refinement is to reduced the error of the approximation. There is an inherent difficulty in determining this error. Because it relies on knowledge of the true solution, it can only be accurately calculated when an analytical solution exists. However, by seeing how much the approximate solution changes with increased refinements, an understanding of the error can be reached without knowing the true solution [57].

It is expected that, by taking smaller steps, a better approximation is produced. By subtracting the global results from one resolution from another set of global results at another resolution, a "residual" error is calculated. The smaller this residual is after each refinement, the less the refinement aided is reaching the true solution. The study of the residual is a large area in FEA and CFD [59].

A theoretical way to eliminate any error is to increase the mesh size to a near-infinite number of nodes. While the solution using this method would be incredibly accurate, the near-infinite number of calculations would have to take a near-infinite amount of time to compute. This balance between accuracy and cost leads to a

large assortment of varying methods, each with their own collection of benefits and drawbacks [57, 59].

While FEA is to be used merely as a tool in the initial phase of model validation, knowledge regarding the fundamental nature of the tool allows for improved results. The primary source for all FEA modeling was an expert in the field [28].

2.4 Sensors

While theoretical and computational support for a solution provides a quick and certain result declaring the success or failure of said solution, the many assumptions and linearizations made to convert the real-world problem to a solvable problem leads to errors that can only be observed through experimental testing. Assuming the properties of the fluid are known (c_p, γ, and R), six primary measurements are needed in order to characterize the actual performance of a compressor. The total pressure (Section 2.4.1) and total temperature (Section 2.4.2) should be measured upstream and downstream of the component. With these four values, the compressor efficiency can be determined using Equation 30. To find the required power input, $\dot{m}$ (Section 2.4.3) and ω (Section 2.4.4) must be measured. The power can be calculated using Equation 12. In order to determine how the results from one study relate to other studies, the uncertainty analysis described in Section 2.4.5 should be considered.

2.4.1 Pressure Sensors.

One assertion in thermodynamics is that knowledge of two intensive (mass-independent) properties of simple, compressible system fixes the other intensive properties. Examples of intensive properties are pressure (P), temperature (T), density or specific volume (ρ or v), enthalpy (h), and entropy (s) [13]. By inspection of the units of pressure, shown in Equation (54), it can be shown that pressure describes the "energy

Table 6. Common Pressure Measurement Devices [60]

Type	Lower Limit	Upper Limit
Ionization Gauge	1.0 μP	100 mPa
Pirani Gauge	10 mPa	100 Pa
McLeod Gauge	100 μPa	100 Pa
Manometer	10 Pa	1.0 MPa
Piezoelectric Transducer	10 kPa	100 MPa
Bellows-type Gauge	1.0 KPa	1.0 MPa
Diaphram Gauge	100 Pa	100 MPa
Bourdon Gauge	100 Pa	1.0 GPa
Resistance Gauge	1.0 MPa	100 GPa

density" of a fluid. Pressure measurements are typically split between an absolute pressure (or pressure relative to a vacuum) and a gauge pressure (pressure relative to a reference pressure).

$$\frac{F}{L^2} = \frac{FL}{L^3} = \frac{E}{\forall} \tag{54}$$

A list of commonly used pressure sensors and their measurement ranges is shown in Table 6. Expected gauge pressure ranges for testing of centrifugal compressors is 1-5 MPa. The first three sensors are used for much more fine pressure measurements.

Pressure transducers are a class of pressure measurement devices that convert the analog pressure signal to a digital signal. Four types discussed below are pressure tubes with bonded strain gauges, diaphragm-type transducers, capacitance pressure transducers, and piezoelectric pressure transducer [60].

The pressure tube with a bonded strain gauge is shown in Figure 36. This tube is one of a predetermined thickness, one end connected to the pressure source while the other is capped with a thick plug. Due to the design of the tube, the hoop stress is significant enough to deform the tube. This deformation is detected using a strain gauge. The dummy gauge shown accounts for thermal stresses from fluctuations between the temperature when the gauges were applied and the temperatures under

operation. Due to the thick size of the plug, any strain exhibited by the gauge is due to thermal stresses and should be subtracted from the active gauge [60].

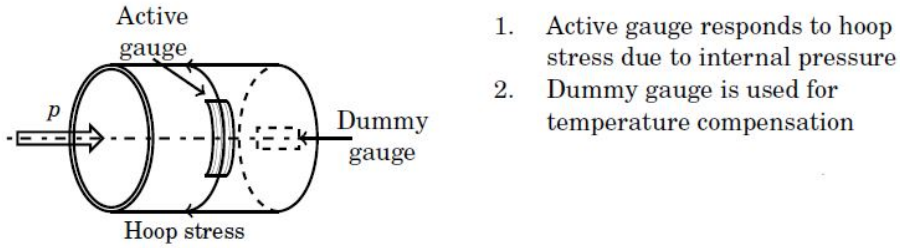

Figure 36. Schematic of a Pressure Tube [60]

The second type of pressure transducer is the diaphragm-type transducer. This transducer, shown in Figures 37-38, relies on the elastic deformation of a diaphragm. The linear voltage differential transformer determines the position of the magnetic core relative to the coils by an electro-magnetic effect. The strain gauge transducer measures the strain of the diaphragm as it relates to pressure [60].

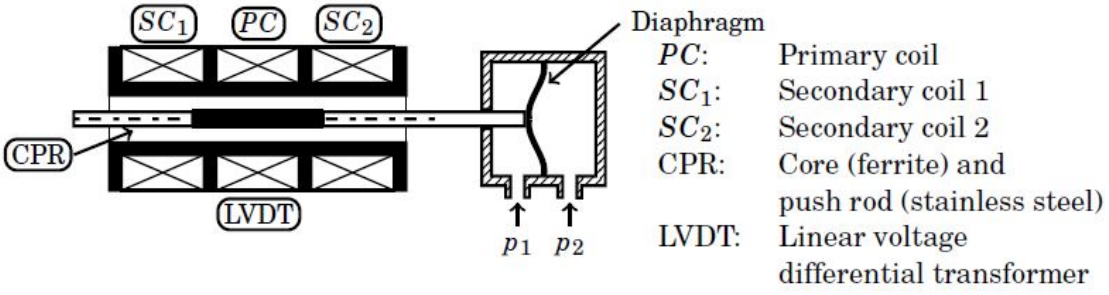

Figure 37. Schematic of a Diaphragm LDVT Pressure Transducer [60]

Capacitance pressure transducers, shown in Figure 39, are similar to the other diaphragm pressure transducers except they measure the capacitance between the diaphragm and the anvil. The capacitance is shown to vary with the inverse of the square of the distance [60].

Piezoelectric pressure transducers use the piezoelectric force transducer, in which the piezoelectric crystal induces a voltage when a strain is induced. Piezoelectric

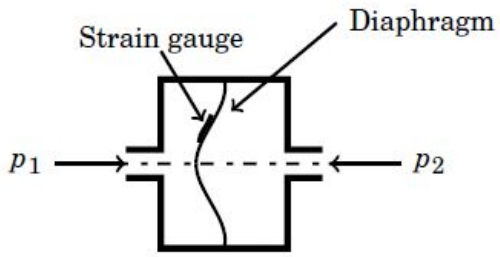

Figure 38. Schematic of a Diaphragm Strain Gauge Pressure Transducer [60]

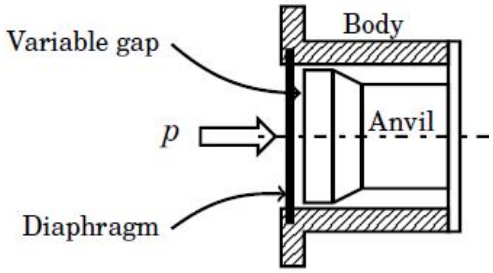

Figure 39. Schematic of a Diaphragm Capacitance Pressure Transducer [60]

transducers are able to display transient pressures in high temperature applications [60].

While measuring both the total and static pressures is typically desired, the process of fully stagnating the pressure can be difficult. One method is using either a Pitot or Kiel probe facing the oncoming flow. This method requires the direction of the flow be known and does not display transient effects [61]. Another method is to locate the pressure transducer in a place of low-speed flow and assume the static pressure is close to the total pressure. This is because the relationship between static and total pressure, shown in Equation 55, states that the difference between total and static pressure is below 5% until around $Ma = 0.23$ [6].

$$\frac{P_t}{P_s} = \left(1 + \frac{\gamma - 1}{\gamma} Ma^2\right)^{\frac{\gamma}{\gamma - 1}} \tag{55}$$

The American Institute of Chemical Engineering (AIChE) procedure for testing centrifugal compressors [62] defines a standard method for testing centrifugal compressors - many of which will be attempted to be followed in the testing. AIChE recommends measuring temperature and pressure at two or more locations on both the upstream and downstream flow. The pressure measurements should also be located 10-20 diameters downstream to allow for laminar flow to develop and after the last flow distortion to minimize swirl and pressure drops.

2.4.2 Temperature Sensors.

As mentioned in Section 2.4.1, two intensive properties are necessary to determine the remaining properties of an ideal gas. Pressure and temperature are typically chosen because of the many material and physical changes directly associated with temperature and pressure fluctuations. This allows a variety of sensors to be made to measure these changes. While pressure could be described as the potential energy of a stationary fluid, temperature actually is a representation of the mean kinetic energy of the individual particles in a gas. This is shown in Equation 56, with k being the Boltzmann constant [63].

$$KE = \frac{3}{2}kT \tag{56}$$

Temperature measurement devices are typically classified by at least seven characteristics: minimum and maximum temperature, resolution, time constant, cost, durability, and size. Each of the following types of thermometers has unique combinations of these characteristics that makes them ideal for certain applications [64].

There are four primary effects that are typically used to measure temperature.These are the thermal expansion effect, the infrared effect, the resistance effect, and the Seebeck effect. Each effect and associated sensors have unique combinations of the above

characteristics and each solves a specific problem better than the others[64]. However, this research only used thermocouples operating under the Seebeck effect, discussed below.

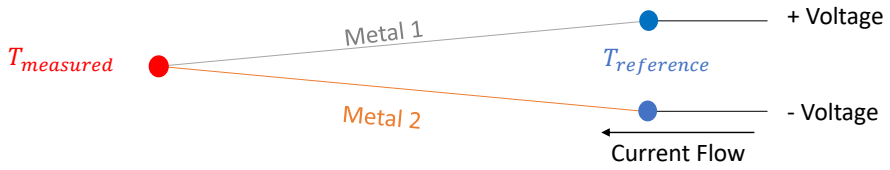

Figure 40. Schematic of a Thermocouple under the Seebeck Effect.

The final temperature effect is the Seebeck effect. The Seebeck effect is in the family of thermoelectric effects including the Peltier effect (formation of a temperature gradient between two electrically charged dissimilar metals) and the Thomson effect (the movement of thermal energy by moving electrons). The Seebeck effect occurs when two dissimilar metals are place in contact with one another and subjected to a temperature gradient. This temperature gradient creates a voltage that can be measured and varies in magnitude with increased temperature differential. This is shown in Figure 40. The thermocouple (TC) measures the temperature at the measurement junction between metals "1" and "2" compared to the temperature at the reference junction. Because the Seebeck effect occurs between any two dissimilar metals in contact, the Seebeck voltage is ideally only dependent on the junctions. However, damaged wires and heating other sections of dissimilar metals lead to changes to the Seebeck voltage [64].

There are three standard classes of TCs. First are the rare-metal TCs. These include types B, R, and S. These are typically used in harsher environments because of their chemical stability and minimal metallurgical changes across a wide temperature range. While they typically provide the best measurements at the widest range of temperatures, their high cost can become a significant factor [64].

The second class of TCs include the base-metal TCs. These include types T, J, K, E, and N. Because they all use nickel to some extent, they all oxidize easily and display metallurgical changes at higher temperatures - for some types, this cannot be reversed. However, when the ambient conditions are not heavily oxidative or measurement is taken only over a smaller range, the much lower cost makes them a preferred choice over the rare-metal TCs. While rare-metal TCs are accurate to tenths of a °C over a wide range, base-metal TCs can only be used over wide ranges when errors up to 10 °C. Each type of base-metal TC has a specific environment that it excels at compared to other TCs.

The final class of TCs are the non-standard TCs. These include G, C, and D type. These TCs are typically only chosen as the only available TC for a certain harsh environment - such as immersion in hot reactive gases. Because of the numerous negative aspects of the non-standard TCs including drift, cost, brittleness, and non-linearity, they are typically the final option left for temperature measurement [64].

Table 7 outlines temperature ranges and associated tolerances for a variety of the discussed TCs [64]. The manufacturer, RS Components Ltd. lists the five TCs that they sell (J, K, N, T, and R). The highest accuracy for temperatures below 670 K is the type T themocouple. They also recommend that for a wide range of conditions, if only one TC is selected it should be the type K [65].

2.4.3 Mass Air Flow Sensors.

If the temperature and pressure are known both before and after the compressor, the efficiency can be determined. However, to actually size a compressor to meet a specific need, the amount of air passing through the system needs to be determined. This can be done a multitude of ways, but four specific methods are discussed below. While the mass flow rate is typically the desired value, the measured quantities -

Table 7. Tolerance Classes for Thermocouples, Reference Junction at 273 K [64].

	Tolerance Class		
Type	Class 1	Class 2	Class 3
Type T, Temperature Range, K	230-620	230-620	70-310
Tolerance, ±	1.5 K, 0.4%	2.5 K, 0.75 %	2.5 K, 1.5%
Type E, Temperature Range, K	230-1070	230-1170	70-310
Type J, Temperature Range, K	230-1020	230-1020	-
Type K, Temperature Range, K	230-1270	230-1470	70-310
Type N, Temperature Range, K	230-1270	230-1470	70-310
Tolerance, ±	1 K+0.3%(T-1100) K	1.5 K, 0.25%	4 K, 0.5%
Type R or S, Temperature Range, K	270-1870	270-1870	-
Type B, Temperature Range, K	-	870-1970	870-1970

typically temperature and pressure - more often lead to a velocity measurement at a point. The velocity then is assumed to be representative of the cross section of the tube. The mass flow rate is found be a conservation of mass through the cross-sectional area, shown in Equation 57, with the ideal gas law applied [60].

$$\dot{m} = \rho A V = \frac{P_s A V}{R T_s} \tag{57}$$

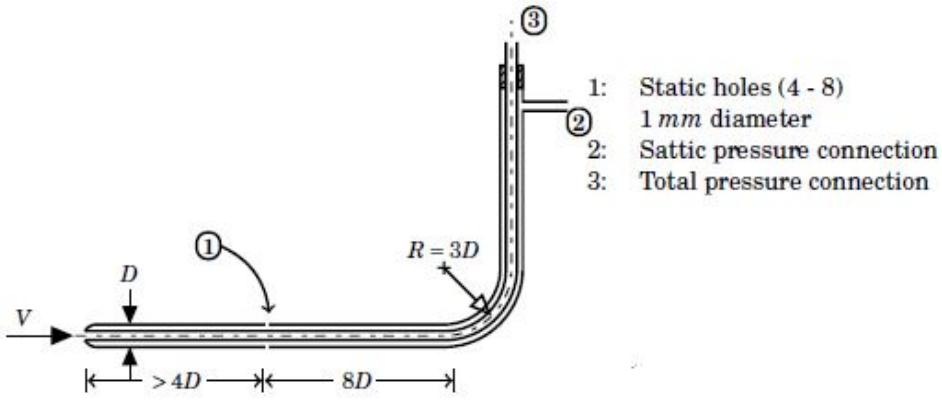

Figure 41. Diagram of a Pitot-Static Probe [60]

The first way to determine mass air flow is based on pressure measurements. A Pitot static probe, shown in Figure 41, measures both the stagnated pressure and the

static pressure. For low-speed, steady, incompressible flow, Bernoulli's principle leads to Equation 58. Combining Equation 57 with Equation 58 leads to a solution for the mass flow rate from the Pitot static probe measurement [60].

$$V = \sqrt{\frac{2(P_t - P_s)}{\rho}} = \sqrt{\frac{2RT(P_t - P_s)}{P_s}} \tag{58}$$

$$\dot{m} = A\sqrt{\frac{2P_s(P_t - P_s)}{RT}} \tag{59}$$

If the flow is compressible ($Ma > 0.3$), the Ma can be found by the isentropic relationship between total and static pressure, shown in Equation refeq:TotaltoStaticMach [60].

$$Ma = \sqrt{\frac{2}{\gamma - 1}\left[\left(\frac{P_t}{P_s}\right)^{\frac{\gamma-1}{\gamma}} - 1\right]} \tag{60}$$

The second method is a temperature-based method. The most common being constant-temperature anemometry (CTA), shown in Figure 42. CTA works by measuring the voltage required to keep a constant current flowing through a section of wire a constant resistance, and thus, a constant temperature. The CTA wire is typically the PRT discussed in Section 2.4.2. It can be shown that the relationship between the voltage (E), flow velocity (V), resistances (R), and the temperature coefficient of resistance (α) is Equation 61 [60].

$$A + BV^n = \frac{E^2 R_{ref}\alpha}{R_{wire}(R_{wire} - R_{ref})} \tag{61}$$

Because all of the values besides V and E are constant, it can be shown that the velocity-voltage relationship can be accurately approximated by a fourth-order polynomial, shown in Equation 62 [60].

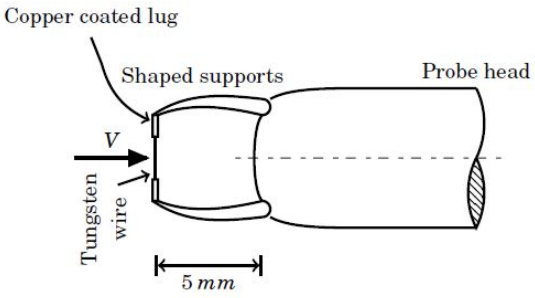

Figure 42. Diagram of a Constant-Temperature Anemometry Probe [60]

$$V = C_1E^4 + C_2E^3 + C_3E^2 + C_4E + C_5 = \sum_{i=0}^{4} C_iE^i \tag{62}$$

Combining Equation 57 with Equation 62 leads to an expression for the mass flow rate based on the output voltage, pressure, temperature, and cross sectional area [60].

$$\dot{m} = \frac{P_sA}{RT_s}\sum_{i=0}^{4} C_iE^i \tag{63}$$

For many mass air flow sensors, the CTA and Pitot static probe are combined into one sensor to be able to measure all necessary components at one cross section to achieve a more accurate mass flow rate.

The final two methods rely on properties of waves of sound or light. The first method measures the Doppler shift (or "red shift") of a wave as it is moved along a medium. When a sound wave is outputted into a flowing medium, it has a tendency to "stretch" and lower in frequency. By knowing the initial frequency, the final frequency, and the angle between the source and the direction of flow, the velocity can be determined. The last method measures the time, t, it takes for an acoustic signal to travel a known length, L, from a source to a sensor. Because the speed of sound, a, is only a function of temperature, any increase or decrease in this speed is purely from the bulk motion of the air. This is shown in Equation 64 [60].

$$V_{bulk} = V_{signal} - a = \frac{L}{t} - \sqrt{\gamma R T_s} \tag{64}$$

Converting to a mass flow rate, assuming a constant area for flow and minimal frictional losses, leads to Equation 65. Ideally, this method would remove the point measurement problem of the Pitot-static and CTA probes because the velocity would be carried by all particles to reach the sensor. Problems associated with this method include noisy signal and difficulty inputting an acoustic signal in line with the flow to a sensor in line with the flow without interrupting the flow [60].

$$\dot{m} = \frac{P_s A}{R T_s} \left(\frac{L}{t} - \sqrt{\gamma R T_s} \right) \tag{65}$$

2.4.4 Rotational Motion Sensors.

The final property required to fully characterize the performance of a centrifugal compressor is the rotational speed. This value is part of the specific speed equation seen in Section 2.1.3.3 that describes how suited the compressor is to its application. In this research, the rotational speed upon failure is needed to determine if the proposed solution would be successful in the desired application. Measurement would either be on the turbocharger turbine or the centrifugal compressor. Likely, the sensor will measure the turbine to minimize the likelihood of damage by compressor fragments. The way most tachometers (devices that measure rotational speed) is by detecting some interruption of a reference signal. Three common types of contact-less tachometers are proximity, magnetic, and reflective optical sensors.

The proximity tachometer measures the electric currents created by a moving magnetic field. This is due to the Hall effect. A Hall-effect sensor is placed between a permanent magnetic and the rotating turbine blades. When there is a gap between blades, the magnetic field passes through the sensor. As a blade approaches, less of

Table 8. Tachometer Sensor Characteristics [68]

Sensor Type	Range, RPM	Distance, m	Minimum Target, m	Range, K
Proximity	1-60,000	0.005	0.001	250-330
Magnetic	1-99,999	0.0001	0.003	200-380
Optical	1-250,000	1.0	n.a.	250-340

the magnetic field passes through the Hall sensor, and an interruption is detected. [66]. The magnitude of the interruption is purely based on the distance from the sensor. Additionally, the number of pulses per revolution is equal to the number of blades that pass close to the sensor. This sensor needs some change in radius of the rotating component to measure an interruption [67].

The magnetic sensor relies on permanent magnets lying within the rotating component. As the magnet passes the pickup sensor, it changes the magnetic flux and induces a current, which is measured. The relationship between the accuracy and operational range is determined by the number of embedded magnets. Two primary problems with this technique are that magnets need to be within the rotating component and that, at higher speeds, the pickup signals begin to overlap [66].

The final common tachometer is the reflective optical sensor. A light source, usually infrared light, is emitted towards a reflective section of the component. A sensor measures the intensity of this wavelength of light. As the reflective section passes by, it is detected. The same tradeoff between accuracy and detection range is through the number of reflective sections [66]. A summary of the three aforementioned sensors is in Table 8 below

Two less common types of tachometers are acoustic measurements and high-speed imaging. An acoustic measurement, such as [69], measures the acoustic signal through a device. This signal is then analyzed for frequencies relating to the speed of the device. Because the passage of a blade through the air creates an acoustic wave, a microphone could be used to determine how many times a blade passes through

a region. The primary problem with this technique is the large ratio of noise-to-information. The high-speed imaging technique is similar to the reflective optical sensor technique. Some point on an exposed component would be visually marked. By counting the number frames required to move a certain angular distance, and knowing the frame rate, the rotational speed can be determined. This method is beneficial because it can provide both a more exact failure speed than the other sensors and insight into the failure location. However, it requires the part be visually exposed and expensive hardware.

2.4.5 Uncertainty Analysis.

Put simply, the goal of uncertainty analysis is to provide confidence that differences in measurements were not purely the result of random chance. Moffat defines error as the difference between a measurement's true value and its measured value [70]. However, the true value is rarely actually known. The uncertainty of a measurement is the quantification of the statistical bounds of this error. One set of uncertainty analysis focus on the two equations below [70].

$$X_i = X_i(measured) \pm \delta X_i \qquad (20:1) \tag{66}$$

$$\delta R = \sqrt{\sum_{i=1}^{N} \left(\frac{\partial R}{\partial X_i} \delta X_i \right)^2} \tag{67}$$

Equation 66 is interpreted to mean that the best estimate of X_i is $X_i(measured)$ with a 20:1 odds that the uncertainty is not larger than δX_i. This is a statistical confidence interval and is typically expected when reporting any measurements. Equation 67 is a formula for calculating the uncertainty of a collection of results, R. The uncertainty of one variable, δX_i, affects the uncertainty of the results, δR, through the sensitivity coefficient, $\frac{\partial R}{\partial X_i}$, which is how much R changes with a small change in X_i.

There are three requirements before Equation 67 can be used. The first is that the the variables, X_i, must be independent. The second is that each X_i must be from a Gaussian distribution. The third requirement is that the odds of each individual uncertainty must be the same for each input [71]. Equation 66 provides a general way to describe both the mean and the uncertainty of any measurement and Equation 67 provides an equation for calculating this error [70].

In addition to providing an equation to calculate error, Moffat discusses two primary types of error: bias errors and precision errors. Bias error is a constant offset of the measured value from the true value. These errors affect the accuracy of a measurement. However, once known, they are relatively easy to correct. By measuring the output at a "known" value, the bias becomes the difference between the known and the measured values. Correcting the measurement then simply becomes adding the original difference to every measurement. The second error is the precision error, otherwise known as the "noise" of the data. While the bias was assumed to be a constant offset with zero fluctuations, the precision has a zero mean with many fluctuations. The best way to correct this error is with a filter of some design. A common technique is to average a large sample of data, because precision errors are assumed to have no offset errors, a large sample will display a measured mean equal to the true value [70].

While errors stemming from the bias and precision of a measurement device are commonly recognized, a less common source of error is the system-sensor interaction. These errors are created by the disruption of the unmeasured experiment by some measurement devices. For instance, while measuring temperature in a flow field, some thermocouple is inserted into the flow. This thermocouple causes the local flow to change, leading to a change in the heat transfer, changing the local temperature at that point. These errors are typically more difficult to correct because they require

a deep understanding of the physics surrounding the experiment. Additionally, the equations made to estimate the error typically rely on material constants that each have their own errors [70].

By stating that "The reported value is the best estimate for the result, and, with 95 percent confidence, the true value is believed to lie within ±XX of that value," there is no murkiness regarding the mean and the uncertainty of the data reported. The common mistake of over-inflating uncertainties in order to match other published work allows erroneous data to continue to exist unchallenged. Underestimating the uncertainty perpetuates the problem and causes unnecessary arguments [70].

III. Experimental Setup

There were three primary objectives for this project that influenced the amount and types of experimental testing that was required. The first objective was to create a low cost, additively-manufactured centrifugal compressor that could be made lighter, quicker, and cheaper than the current compressors. The second objective was to determine if the failure conditions could be accurately modeled using FEA; ideally matching both the failure speed and the initial location of failure. The third objective was to determine the effects of AM on the compressor performance.

While the various experimental setups could be pursued in parallel to some extent, the material testing, Section 3.1, influenced the direction that the design process took. Section 3.2 details the FEA performed to predict the compressor failures. Section 3.3 describes the physical testing of the compressors.

3.1 Material Testing

While essentially every manufacturer publishes material properties [44, 53, 54], they rarely publish material properties at a wide range of temperatures. Instead, they often characterize the thermal "strength" with either the glass-transition temperature (GTT), the temperature that the material transitions from a brittle, stiff solid to a viscous liquid [27], or the heat deflection temperature (HDT), the temperature that a stress (commonly 0.455 MPa or 1.82 MPa) causes a deflection of 0.25 mm [72]. While these values provide some indication of the range of operating temperatures, they fail to indicate how much the material properties, such as ultimate strength or elastic modulus, varies with temperature.

If the published material properties were used in the FEA model, the analysis would be considered "cold". This would ignore the thermal effects of compressing the

air and any back-conduction from the heated side, leading to actual failure occurring before the predicted failure. By collecting basic material properties such as ultimate strength and modulus of elasticity across a range of temperatures, the FEA model could account for the thermal effects and its accuracy could be improved.

Three materials were tested in this section that had favorable characteristics discussed in Section 2.2.2. The sections below detail the process used to collect the variable material properties. Section 3.1.1 describes the test rig used, Section 3.1.2 explores the temperature profile over which testing occurred, Section 3.1.3 discusses the various tensile test specimen designs, Section 3.1.4 provides the testing profile and testing matrix used, and Section 3.1.5 examines the data reduction methods used to convert the force-displacement data to material properties.

3.1.1 Tensile Test Rig.

The test rig used, shown in Figure 43, was a 810 Material Test System (MTS) capable of pulling with a force of up to 22 kip with a max error of 0.37% of the reading along the full range of the system [73]. The displacement was determined using the internal measurement capabilities of the system, with a full range of 5 inches with a maximum error of 1.67% of the reading [74]. The heaters surrounding the test area were MTS Model 653.01 heaters. These heaters were capable of heating the specimen up to 1673 K with a control point stability of ± 1 K [75].

3.1.2 Temperature Profile.

The driving purpose when designing the temperature profile was ensuring that the complete range of likely temperatures was tested while minimizing any additional testing. The low temperature was 300 K, representing the expected ambient temperature in the testing environment. The high temperature was 435 K. This ensured

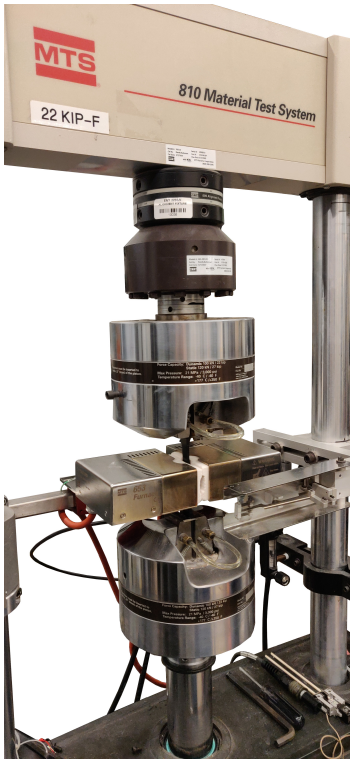

Figure 43. Heated Material Test System with ULTEM 9085 Test Specimen

Table 9. Initial Tensile Test Specimen Matrix

Material	Temperature					Specimen Count
	300 K	330 K	365 K	400 K	435 K	
ULTEM 9085, XZ	2	2	2	2	1	9
ULTEM 9085, ZX	1	1	1	1	1	5
Onyx, XZ, Kevlar	2	0	0	0	1	3
300-AMB, XZ	2	2	2	2	2	10

that the testing exceeded the 400 K temperature expected in Section 2.1.5.3. Five temperatures were initially chosen within these bounds as seen in Table 9.

3.1.3 Test Specimens.

The test specimens used for material testing were based on the ASTM D638 Standard: Standard Test Method for Tensile Properties of Plastics [55]. The Type I specimen was chosen because it "is the preferred specimen and shall be used where sufficient material having a thickness of 7 mm (0.28 in.) or less is available" [55]. The

original Type I test specimen is shown in Figure 44. This test specimen was modified to adjust for variations in the specimens' materials and the physical limitations of the test system.

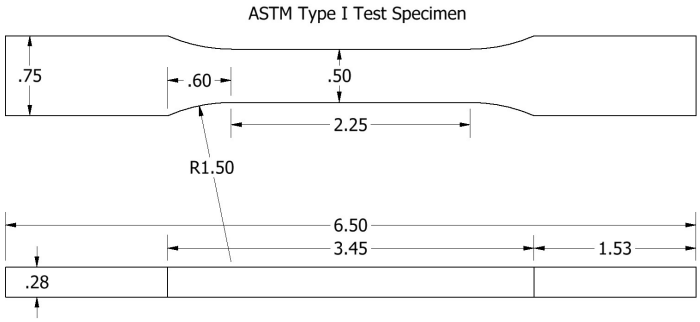

Figure 44. ASTM Type I Tensile Test Specimen

The first material tested was ULTEM 9085 by Stratasys. This material was printed in both the XZ and ZX direction in an attempt to characterize anisotropic material properties. These were printed with default settings besides changing it to 100% infill according to the Stratasys software. Fifteen ZX specimens were attempted, but only five specimens successfully printed. The second material tested was Onyx by Markforged. This material was printed in the XZ direction, with three samples printed with two Kevlar lines on each layer, two shells, and 100% infill. Both materials used the same test specimen model shown in Figure 45, modified from the ASTM Type I model. The specimen was lengthened to ensure that it fit in the provided MTS machine. The region in the grips was thickened to fit in the fully closed grips of the MTS machine. The middle section was thinned to ensure failure occurred in the desired region. A large fillet connected the two regions, reducing the stress concentration.

Due to the physical limitations of the 300-AMB printer, these test specimens required alterations in order to fit within the build volume of the printer. The altered test specimen is shown in Figure 46 and was printed in both the XZ and ZX direction.

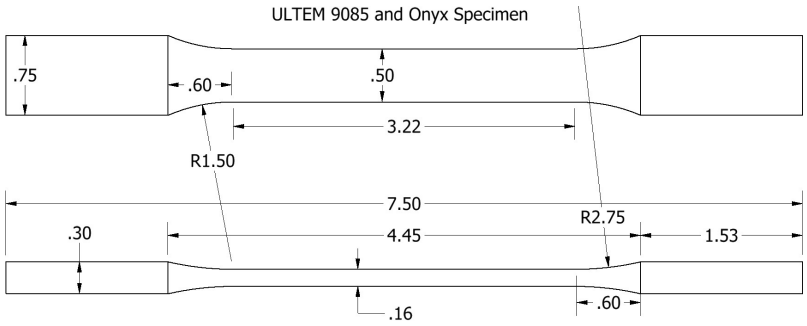

Figure 45. Tensile Test Specimen for ULTEM 9085 and Onyx

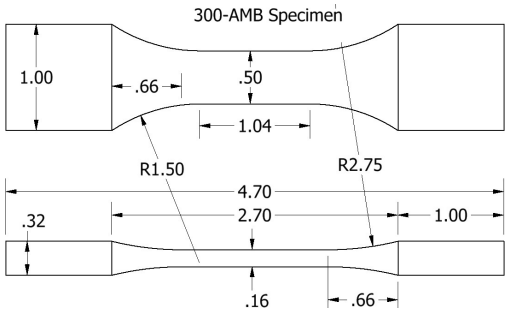

Figure 46. Tensile Test Specimen for 300-AMB

3.1.4 Testing Profile and Test Matrix.

The testing profile began with the two heaters warming up to the desired temperature at a rate of 0.25 K/s. Once both heaters had reached this temperature, a fifteen-minute thermal soak occurred - allowing the specimens to reach the desired temperature. Finally, the specimens were pulled apart at less than 5 mm/min, in accordance with ASTM 638 [55]. While the ASTM 638 standard required five specimens in each of the two anisotropic directions, fewer were used. This was because the total number of samples quickly exceeded the time constraint available for testing. The testing matrix used is seen in Table 9. Ideally, far more than five specimens would be tested over a larger range of temperatures. The accuracy of the specimens limit the accuracy of the FEA model.

3.1.5 Data Reduction.

The data recorded by the MTS machine included the force in N and the displacement in mm, trimmed to only include positive stress. The stress for each specimen was found with Equation 68, with the area calculated by the average of 5 measurements of both the width (w_i) and thickness (t_i) of the individual specimen. For the unheated specimens, the strain was found by dividing the measured displacement (δ) by the original length (L_o) of the thin section. The strain was corrected to ensure that zero strain (ε_o) occurred at the first data point, corresponding to zero stress. Equation 69 shows these calculations. The modulus of elasticity (E) was the slope of the first 800 data points, shown in Equation 70. Finally, the maximum stress was the ultimate strength.

$$\sigma = \frac{F}{\Sigma_{i=1}^{5}(w_i/5) * \Sigma_{i=1}^{5}(t_i/5)} \tag{68}$$

$$\varepsilon = \frac{\delta}{L_o} - \varepsilon_o \tag{69}$$

$$E = \frac{\sigma_{800} - \sigma_1}{\varepsilon_{800} - \varepsilon_1} \tag{70}$$

While the heated section was only roughly one inch long, the displacement occurred along the whole length of the specimen. If the displacement was assumed to occur equally over the whole length as before, there would be more strain for the same stress, leading to a lower E. Alternatively, assuming the displacement only occurred within the heated section would ignore the displacement in the unheated sections. The lower strain would lead to a higher E. A third option used the original E found in the unheated sections (E_u) to predict the displacement due to stress in the unheated section (δ_u). This displacement was removed from the measured displacement to estimate the displacement within the heated section (δ_h). This process is shown in Equations 71-73. While this method assumed distinct temperature regions (no

conduction), it corrected the much worse assumption of constant displacement across the specimen.

$$\delta_u = \frac{\sigma L_u}{E_u} \tag{71}$$

$$\delta_h = \delta - \delta_u \tag{72}$$

$$E_h = \frac{\sigma L_h}{\delta_h} \tag{73}$$

3.2 Finite Element Analysis

Because centrifugal compressors have a vast array of design features and complex geometries, there is no analytical equation that can be used to predict failure speed. When temperature-dependent material properties become desired in the analysis, a simple equation becomes even less realistic. Numerical methods, such as FEA, take a complex problem and convert it to a large collection of basic fundamental equations. The complicated shape, i.e. the compressor, is broken apart into many interconnecting nodes. Each node is connected to other nodes and experiences body forces (centripetal acceleration) and forces from interactions with surrounding nodes that are experiencing their own body forces. By solving the large number of smaller equations describing these nodes, a close approximation to the actual solution can be obtained.

While FEA seems to provide a definitive answer to what is happening to the compressor, hidden assumptions mean that the answer may not correspond to reality. The purpose of this section is to describe the FEA method that was used to predict the speed and location of failure. Two compressors were analyzed, the JetCat P400 compressor and the Garrett GTX5008R compressor. The P400 compressor was used to meet the first objective of the project to create an AM substitute compressor in a

micro-turbine while the GTX5008R compressor was used to determine the effects of AM on compressor performance. These compressors are seen in Figure 47.

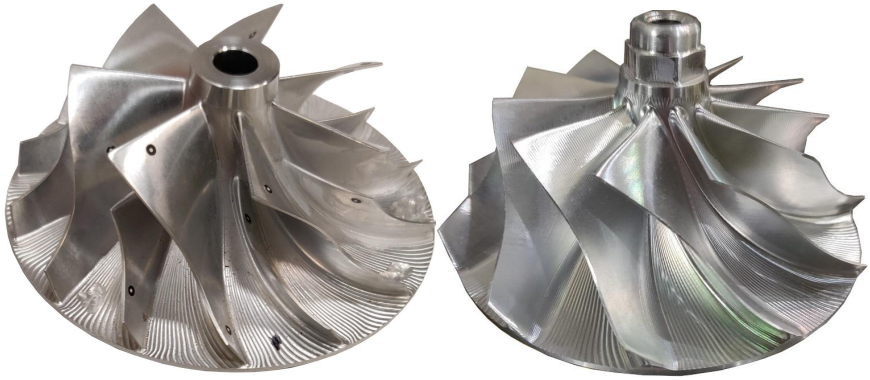

Figure 47. Stock P400 (left) and GTX5008R (right) Compressors

Section 3.2.1 discusses the process to go from a physical compressor to a CAD-capable compressor. Section 3.2.2 describes the process used to create the mesh. Section 3.2.3 details the need for a variable temperature model and the temperature boundaries used. Section 3.2.4 explains the structural boundaries and how failure was determined.

3.2.1 Model Creation.

These compressors were scanned using a white light method to create a point cloud. A point cloud is a collection of points representing the detected positions of surface. This is shown in Figure 48. While the point cloud could have been used for printing, it offered limited opportunity for modification and was less "clean" than desired. Marks for the original manufacturing and random holes/planes were leftover from the scanning. Additionally, the solid interiors of the compressors were absent [28].

In order to get an editable model, the point cloud needed to be converted to a closed model. The closed model was made by connecting the points into curves and simple shapes. Erroneous planes were removed while required planes were added into

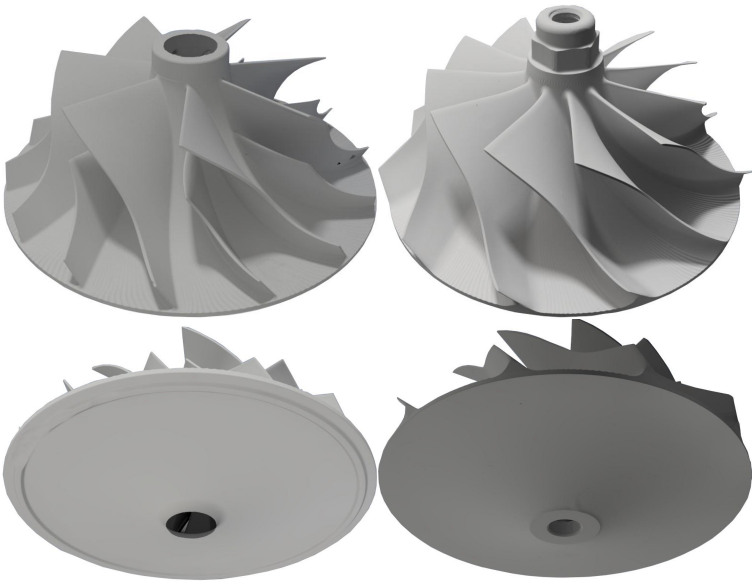

Figure 48. Point Cloud of P400 (left) GTX5008R (right) Compressors.

the model. Key dimensions were measured and drawn into the model. Finally, all of the blades were made identical to one another. The closed models are shown in Figure 49 [28].

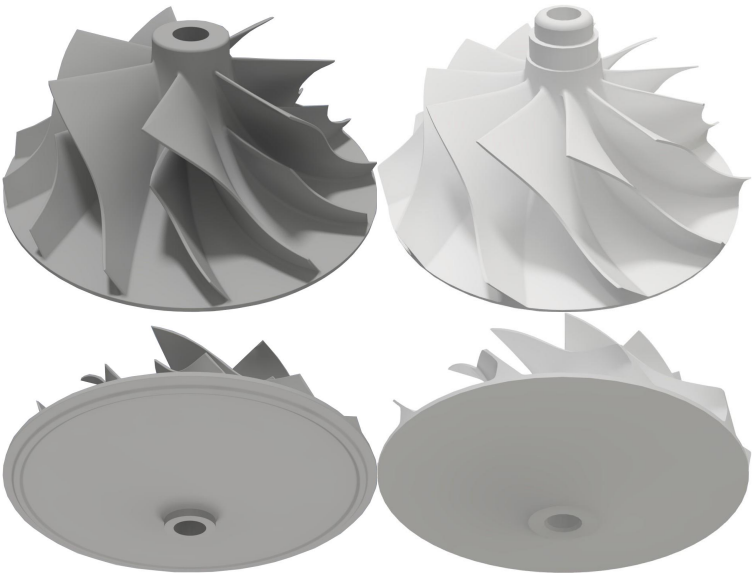

Figure 49. Closed Models of Compressors

3.2.2 Mesh Creation.

One of the first steps in computing an FEA model is to create a mesh. This mesh is one of the driving factors of a models accuracy. As the number of nodes increases, the degrees of freedom also increase. While a perfect model could be created by matching the number of nodes to the number of atoms, the solution would become both impossible to compute and unnecessary. As with most problems, a balance of both accuracy and cost must be met. The more accurate the model, the higher the cost, which in this case was computational time. ANSYS's adaptive meshing feature was used to ensure a large number of nodes were present in regions that were predicted to have more complicated stresses while minimizing the node count in flat regions to speed up the convergence. The mesh obtained through this method on the P400 compressor is shown in Figure 50.

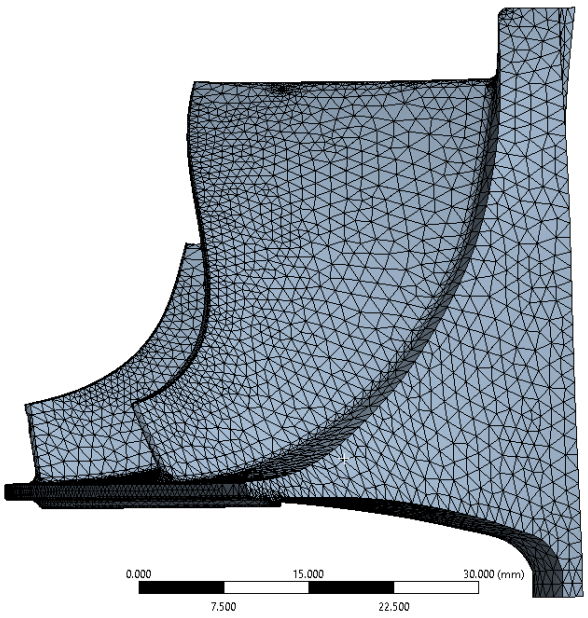

Figure 50. Adaptive Mesh for Stock JetCat P400

3.2.3 Temperature Profile.

While an isothermal analysis of the compressors would have provided insights into failure speeds and locations, this "cold" analysis would have ignored many of the driving factors of failure. The high temperatures seen in these compressors push the materials to the edge of their operating region. Because of the highly temperature-dependent ultimate strengths seen in the material testing, assuming the material maintained its published strength would lead to failure speeds below the predicted values.

ANSYS's Workbench Static Thermal module was used to create the thermal profile with the goal of closely matching the boundary conditions seen in Section 2.1.5.3. The incoming air was 293 K, the standard room temperature in the test cell. The section where the compressor contacted the turbocharger body was set at 335 K, set by the oil temperature seen during test runs of the turbocharger. Finally, the outer bounds of the compressor body were set at 400 K. This was the primary value not explicitly measured due to the difficulty in accurately measuring in the small passages. Published values for the thermal conductivity were used to create the temperature gradient.

Figure 51 depicts the thermal gradient for the P400 and the GTX5008R compressors. One apparently influential design difference between the P400 and the GTX5008R compressors is the effect of the radius of curvature on the thermal profile. The larger radius of curvature on the GTX5008R places more mass close to the hub which helps cool the bore more.

3.2.4 Structural Profile and Failure Analysis.

While the thermal analysis provided details on how the compressor transmitted heat, it did not describe how the compressor reacted to the high operating speeds

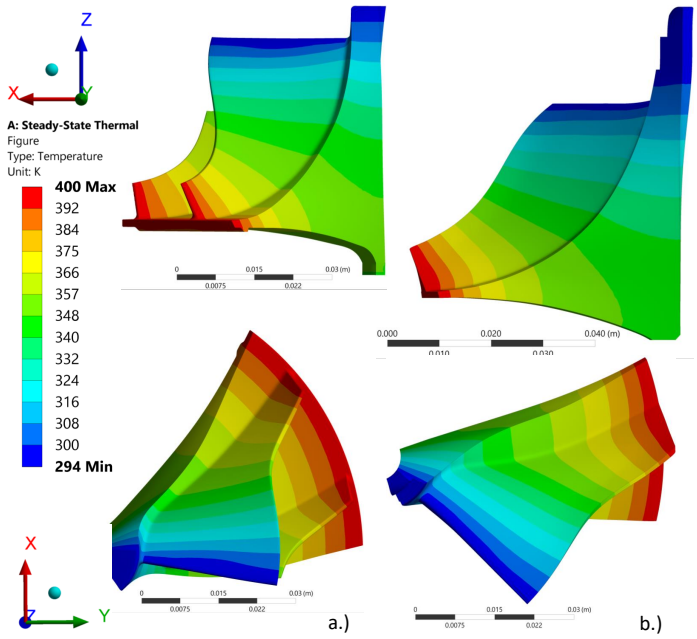

Figure 51. Compressor Thermal Profile. a.) P400. b.) GTX5008R.

within the turbocharger or jet engine. By subjecting the compressor to the body forces experienced due to acceleration, knowledge of both the internal stresses and the deformation was obtained. The internal stresses were calculated and then affected the deformation model through the temperature-dependent moduli of elasticity inputted earlier into the model [28].

Using ANSYS's Static Structural module, a rotational speed was applied to the model about its axial axis. Additionally, the top most surface was fixed in both the (z and r) direction in order to constrain the motion to purely about the axial axis. Finally, the temperature profile from Section 3.2.3 was applied to allow the temperature-dependent properties to affect the solution [28].

Although ANSYS could not include temperature-dependent ultimate strengths in its material definitions, a manual approach was taken to retain the temperature dependence. To demonstrate the process, the results from ULTEM 9085 with a speed of 98,000 RPM is shown in Figure 52. The temperature profile, seen in Figure 52a, was divided into six colors. These were the high temperature, the low temperature,

and four temperatures between the high and low. The four temperatures correlated with the temperatures at which the material strength was measured in Section 3.1. The results obtained are shown in Figure 52b. The colors chosen for the legend are similar to the temperature legend, the high stress, the low stress, and four stresses that correlate to the ultimate strength at the opposite temperature. For example, at 300 K, σ_u is 76.09 MPa while at 365 K, σ_u is 24.84 MPa. By graying out everywhere that is below σ_u at that location, Figure 52c is obtained. Wherever there is color, $\sigma > \sigma_u$ at that location [28].

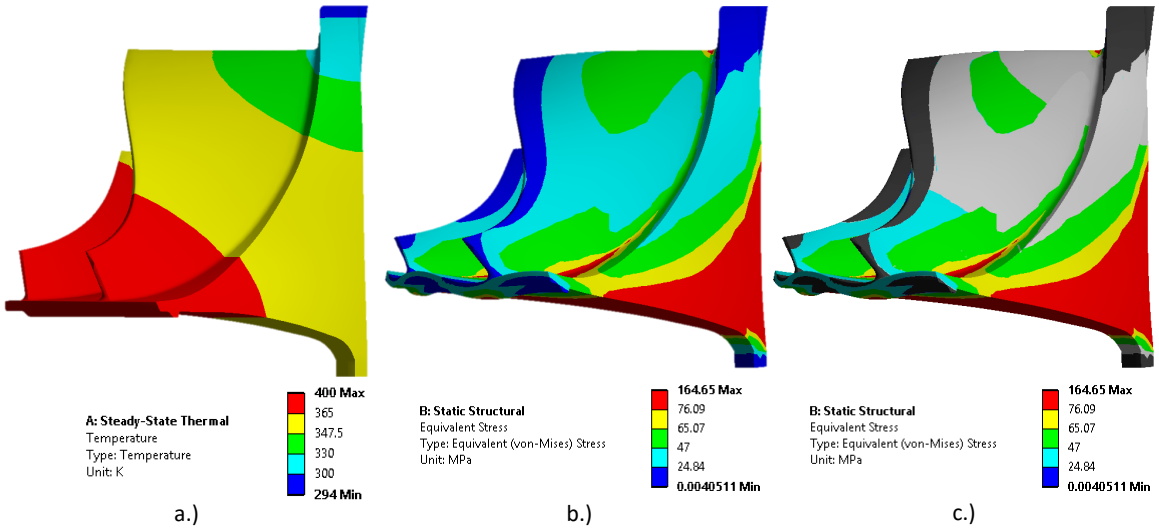

Figure 52. Post-Processing to Account for Temperature-Dependent Ultimate Strength

3.3 Physical Testing

Even though the results from the FEA in Section 3.2 appeared to provide conclusive answers, hidden simplifications and deviations from the actual compressor setup required physical testing to ensure the model did not simply omit any catastrophic feature. At least four primary simplifications were made in the FEA model that likely had at least some impact in the compressor failure. The first simplification was the surface forces on the compressor body due to pressure gradients and viscous shearing.

This was omitted because they accounted for less than 2% of the centrifugal forces [2]. The second simplification was that the compressor had reached steady-state in both the thermal and structural analysis. Thirdly, the material was considered isotropic for the FEA model while the layered method of material extrusion and vat photopolymerization create highly anisotropic materials. Finally, any forces from the blades rubbing were ignored despite knowing that the blades would likely rub on the shroud.

The discussion of the experimental test stand is split into two separate subsections. Section 3.3.1 describes the turbocharger test stand while Section 3.3.2 is focused on specifically the compressors.

3.3.1 Turbocharger Test Stand.

The similar size and shape of the P400 compressor to a turbocharger compressor, coupled with the difficulty of driving a 140 kW compressor at 98,000 RPM with any motor, made using a large (suited for 875 - 1700 hp vehicles) turbocharger the obvious choice [11]. The three following sections describe the initial test stand and measurement devices (3.3.1.1), shroud modifications (3.3.1.2), and additional modifications after testing began (3.3.1.3).

3.3.1.1 Initial Test Stand.

The test stand for physical testing of the centrifugal compressors was made using an automotive turbocharger powered by pressurized air. The turbocharger used the Garrett GTX5009R turbine and drove the GTX5008R and P400 compressors. Figure 53 provides an overview of the test setup. The following close ups of the various sections describe the various sensors.

The overall flow of air began with the turbine intake. The turbine intake was attached to the facility's high pressure air supply, capable of a maximum pressure

of over 100 psig, a maximum sustained flow rate above 2 kg/s, and flow heated to greater than 450 K. The high-pressure air entered and imparted energy to the turbine, then vented into the test cell. The imparted energy from the air spun the turbine which spun the compressor. The compressor drew in air through a filter, past a mass air flow sensor, down a stretch of tubing to help straighten the flow, and then into the compressor. The compressor spun the flow, added energy from the turbine side into the flow, and outputted it into the volute of the turbocharger to raise the static pressure by slowing the flow. The GTX5008R used its stock volute while the P400 used a modified GTX5009R volute, discussed in Section 3.3.1.2. The flow then exited the compressor housing, through a stretch of tubing with a butterfly valve at the end. This valve provided a back-pressure to the compressor to vary the mass flow rate, allowing any point within the compressors' operational map to be reached.

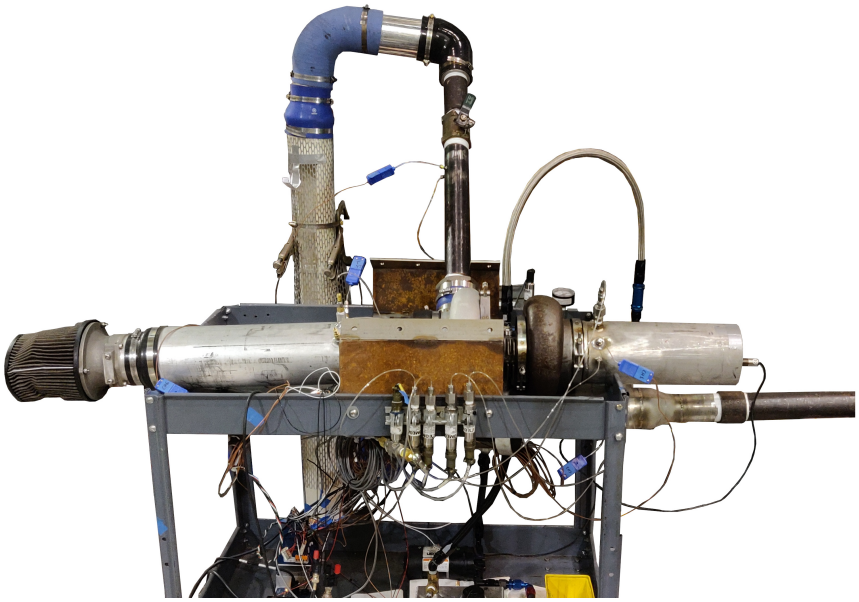

Figure 53. Compressor Test Stand

Figure 54 shows the turbine air intake and exhaust pipes. The intake pipe was a combination of a 75 mm diameter, 150 mm long steel pipe welded to another 50 mm diameter, 150 mm long steel pipe, connected with an expander section. There were

three sensors collecting data on the intake flow, attached to the 75 mm diameter pipe. The top sensor was a T-type thermocouple placed radially in the middle of the flow. This type of thermocouple was used for every temperature measurement because of the higher accuracy at temperatures within the expected temperature ranges, with a range of 75-645 K, an accuracy of $\pm 0.75\%$ of the measured value, and a response time of 0.6 seconds [68]. Because this thermocouple integrated the flow around it axially, the measurement was a combination of the static and total temperatures. The middle sensor was a Kiel probe to measure the stagnation pressure, placed radially in the middle of the flow, with the opening facing the oncoming flow. This probe was connected to a pressure gauge with a range of 0-250 psia $\pm 0.05\%$. The bottom port was for static pressure measurements. It was a small, open, and smooth hole to minimally disrupt the flow yet provide the static pressure of the flow. This port was connected to a pressure gauge with a range of 0-250$\pm$0.02 psia [76]. Both the Kiel probe and the static port also were connected to a differential pressure sensor, capable of more fine measurements of 15$\pm$0.012 psig between the two pressures. Assuming a linear velocity profile, these values allowed the velocity and mass flow rate of the air to be approximated.

Figure 54 shows the turbine air exhaust. The exhaust pipe was a 120 mm diameter steel pipe, 330 mm long. Like the intake, there were three sensors present for measuring the temperature and pressure, placed into the flow in identical ways to the turbine intake. The top sensor was a T-type thermocouple placed radially in the middle of the flow. The Kiel probe connected to a pressure gauge with a range of 0-50$\pm$0.04 psia [76]. The static pressure connected to a similar gauge.

While automotive turbochargers typically detect rotational speed through the use of a magnetic flux sensor located near the compressor, an infrared (IR) interruption sensor was used to detect the rotational speed of the turbocharger. This was done

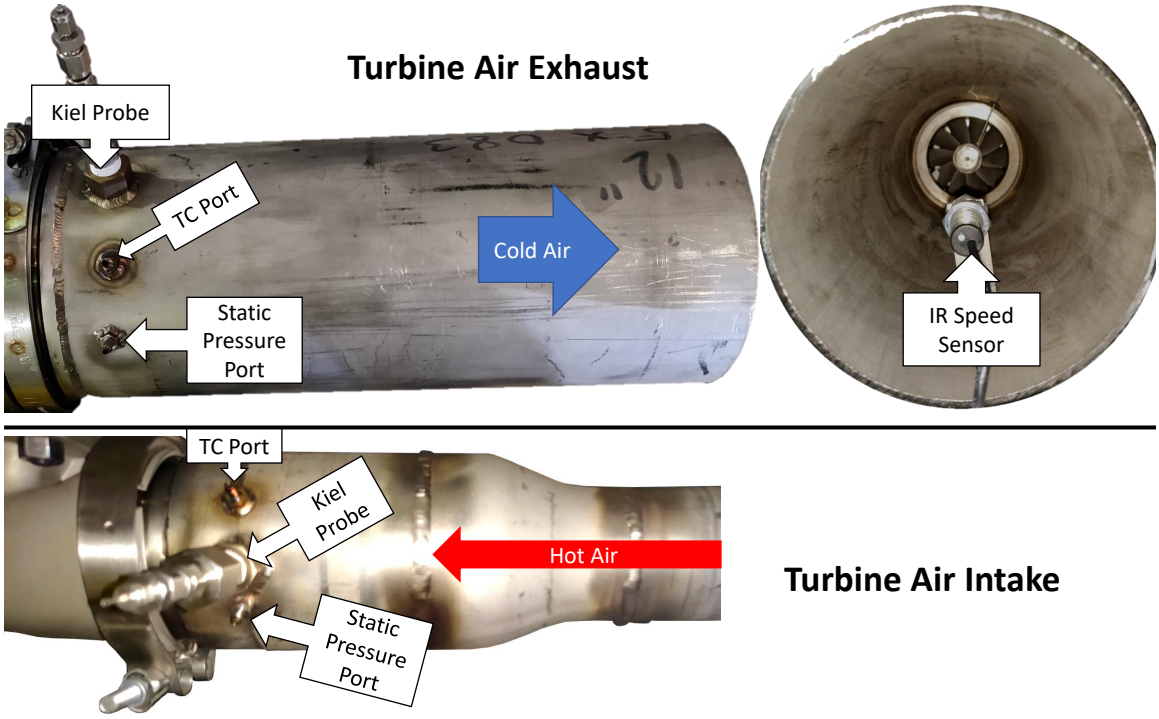

Figure 54. Test Stand Turbine Air Exhaust, Exhaust from Back, and Intake

for two reasons. The first was that the use of plastic for the compressor eliminated any magnetic flux for detection. The second reason was that the use of cooler turbine supply gas allowed a sensor to be placed in line with the turbine. This is shown in Figure 54. The sensor was angled to point at a section of reflective tape located at the hub of one of the blades. The sensor used was the Monarch Instrument ROS capable of measuring rotational speeds from 1-250,000 RPM [77].

The turbine section was made up of the GTX5009R turbine and the associated turbine housing. The compressor housing, Figure 55a, directed air in from the left and exhausted it upward. The shaft of the turbocharger for the compressor was a fixed length of 57.7 mm and a diameter of 9.47 mm, seen in Figure 55b. This shaft was an important design dimension because if the hole was either too large or too small, the compressor would not attach correctly. The turbine, seen in Figure 55c, extracted the energy from the flow. The turbine housing, Figure 55d, connected underneath

the test rig to the air supply and exhausted to the right. Oil was pumped through the system to maintain lubrication and to center the bearings. The oil system was gravity-fed so the orientation of the turbocharger needed to ensure the oil intake was from above. All of these connections were with V-bands, with mating connectors welded to pipes.

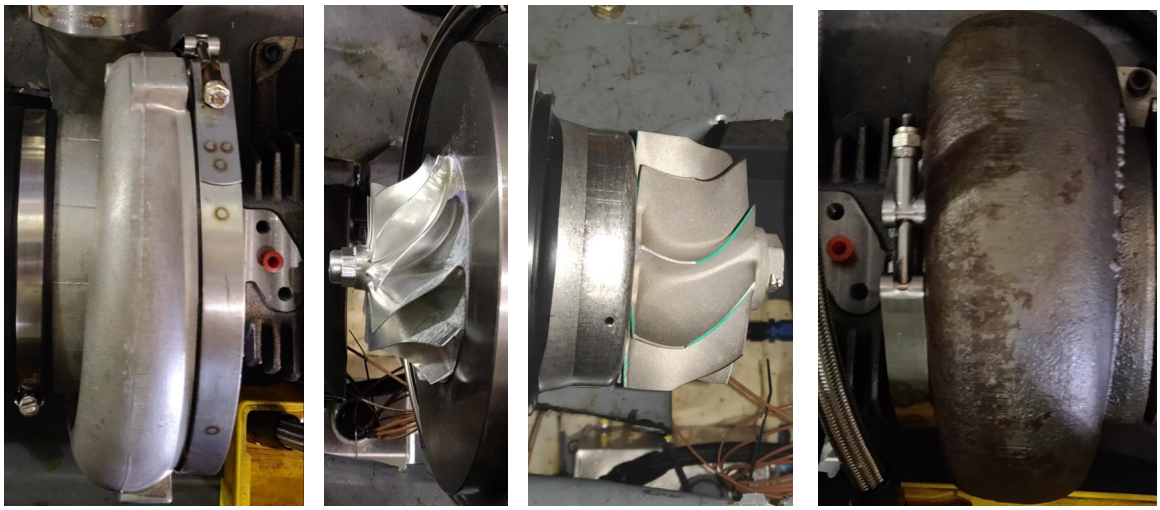

Figure 55. GTX5009R Turbocharger. a) GTX5008R Compressor and Backplate. b) GTX5009R Turbine. c) Compressor Housing. d) Turbine Housing.

The air intake for the compressor side of the turbocharger began with a Pro-M Racing 92 Mass Air Flow Sensor (MAF). The filter was present to prevent foreign particles from entering the compressor intake. Although there was an associated pressure drop from the filter, it was minimal and allowed for more precise mass air flow. The filter and the MAF is shown in Figure 56.

After the MAF, the air flowed through a 600 mm long, 120 mm diameter aluminum tube. The set of sensors was aligned 400 mm from the MAF intake. Although this was not the standard 10 ft length for testing compressors, it allowed the flow to transition to at least a more stable state [62]. The three sensors were the same as the other sensors mentioned previously regarding the turbine intake and exhaust, with

the thermocouple at the top, the Kiel probe for the total pressure in the middle, and the static pressure port at the bottom. The Kiel probe was connected to a pressure gauge with a range of 0-30±0.024 psia and the static pressure port was connected to a a similar gauge [76]. The differential pressure gauge was a pressure gauge with a range of 0-15±0.012 psig. This is seen in Figure 56.

Figure 56. Test Stand Compressor Filter, MAF, and Intake.

The compressor air exhaust, seen in Figure 57a-b, had the same three ports for a T-type thermocouple, a Kiel probe for total pressure, and a static pressure port, from left to right. The Kiel probe was connected to a pressure gauge with a range of 0-150±0.12 psia and the static pressure port was connected to a similar pressure gauge [76]. These ports were welded 320 mm from the volute exhaust in a 55 mm diameter steel pipe.

A butterfly valve was installed at the end of the compressor exhaust tube. This is seen in Figure 57c. The purpose of this butterfly valve was to provide a back-pressure to the compressor. This allowed a continuous adjustment of air flow which allowed all regions of each compressor's operating map to be reached. When the valve was fixed in one location, a operating line of pressure vs. air flow was created as the rotational speed increases. While there were markings indicating the current angle of the butterfly valve, there was no way to control the valve during turbocharger operations. This led to a "guess-and-check" method to get the compressor on the desired operating line.

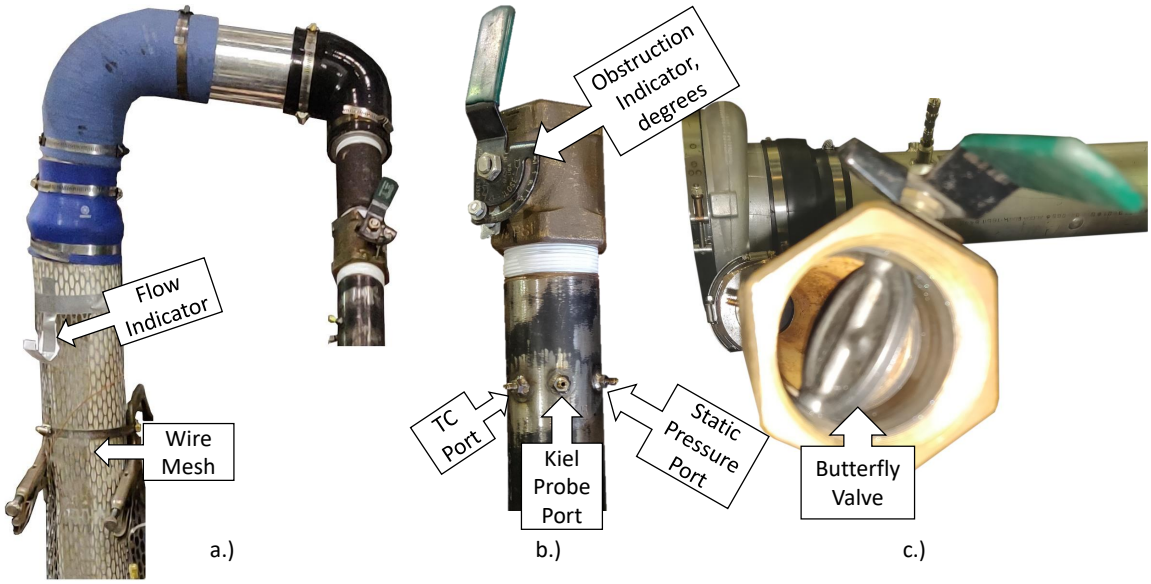

Figure 57. Test Stand Compressor Air Exhaust.

3.3.1.2 Shroud Modifications.

When a compressor is designed, it is typically assumed that a shroud closely matching the shape of the compressor will be used. If the shroud is too small, the compressor blades will impact the shroud; this would cause either excessive friction or a catastrophic failure. Alternatively, if the shroud is too large, the high pressure air will flow back upstream and mix with the low pressure air; this decreases the compressor efficiency. Because two distinct compressors were tested, two distinct shrouds needed to be used. The GTX5008R compressor had the benefit of already having the stock compressor housing that matched the compressor shape. However, the JetCat P400 compressor did not have a compressor housing that would both fit the compressor and mate up with the turbocharger. Rather than creating a new shroud, volute, and housing from scratch, an amalgamation of the P400 shroud from the engine and an extra GTX5009R compressor housing was made, shown in Figure 58. This met the two requirements: a shroud closely fitting the compressor and a housing that could mate up to the rest of the compressor.

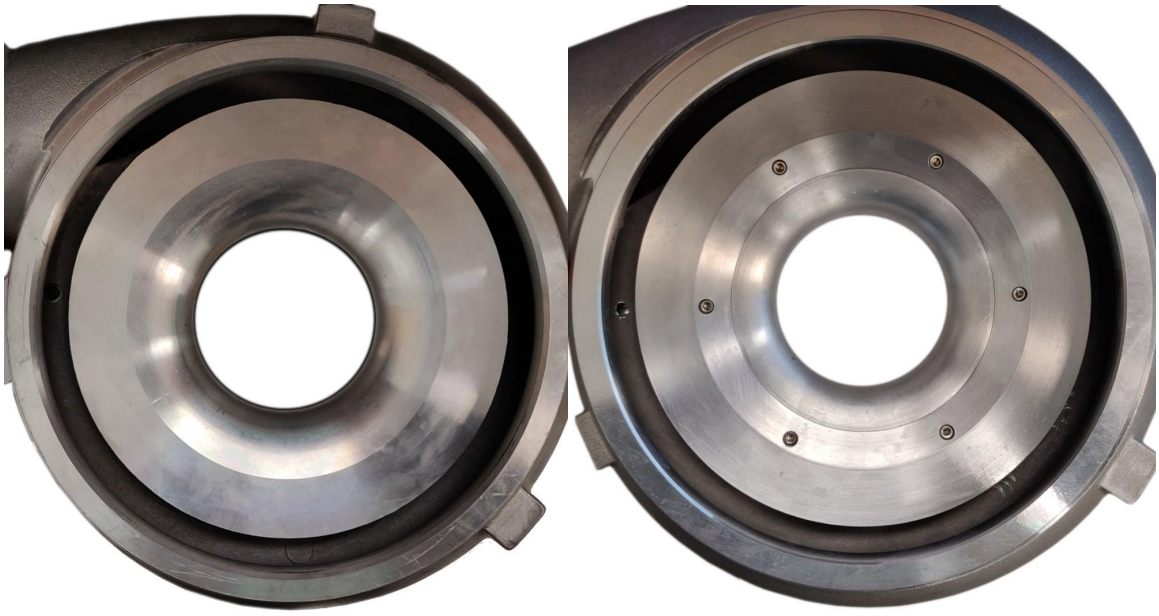

Figure 58. Compressor Housings. a.)Original GTX5008R. b) Modified for P400

3.3.1.3 Test Stand Modifications.

After the first catastrophic test of a compressor, additional modifications were made to improve the test stand and limit future turbocharger purchases. During this catastrophic test, achieving the desired back pressure was difficult due to the aforementioned manual butterfly valve. Upon compressor failure, the now-unloaded turbine overspun and the axial flow exiting the turbine quickly pulled the turbine out of the turbocharger. Because the air heaters needed a certain amount of air flowing past them to prevent them from melting, the air supply could not be quickly shut off. In an attempt to improve future compressor testing, three modifications were made to the test stand.

The first modification was the addition of a variable-position, electronically actuated, ball valve downstream of the compressor, seen in Figure 59a. This valve allowed a repeatable, remote controlling of the back-pressure, providing the ability to move

the compressor around its operating map during a test. This will be important when comparing the printed P400 compressor to the original compressor.

The second modification was the inclusion of a three-way, double acting, pneumatically-actuated ball valve, seen in Figure 59b. When the first compressor failed, it took about a second from the loss of pressure to the beginning on the turbine overspin. This ball valve has a cycle time of 0.12 seconds [78]. By venting the high-pressure air, the turbine stopped quicker than just shutting down the air due to the large vacuum it created.

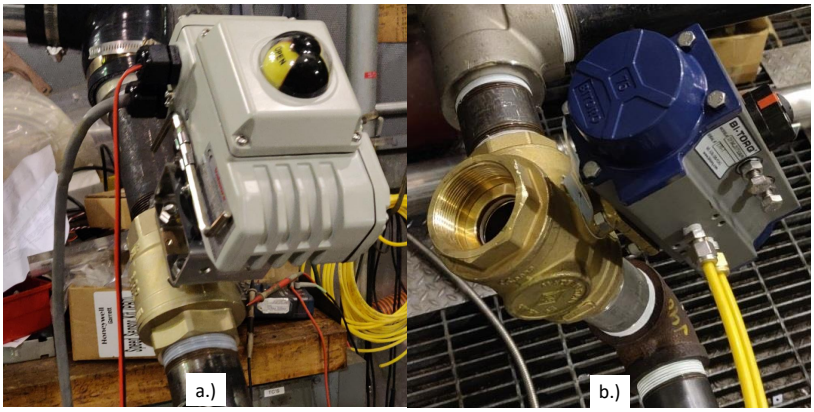

Figure 59. Modifications to Test Stand. a.) Electronic Variable Opening Globe Valve. b.) Pneumatic Three-Way Globe Valve.

A bolt was welded behind the turbine to prevent it from being ejected out the back end again. This is shown in Figure 60. The pointed end fit into a divot in the back of the turbine. If the turbine started to move axially, the bolt would prevent motion and aid in slowing the turbine down.

3.3.2 Compressor Fabrication.

Unlike most metal machining, AM methods vary widely in terms of print accuracy, resolution, and quality. The variations not only occur between methods but also occur within one method. One print is devoid of large voids and close to the desired dimensions while another is covered in print errors that likely affect the flow and

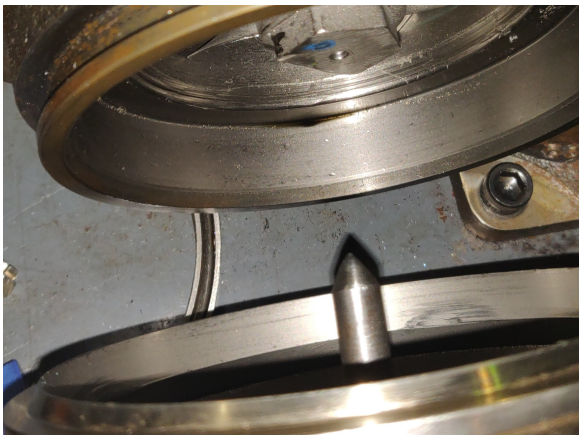

Figure 60. Turbine Axial Motion Limiter.

the compressor strength. Section 3.3.2.1 covers the broad settings used to print the compressors. Finally, Section 3.3.2.2 explains the balancing process that eliminated many additional forces present in an unbalanced system.

3.3.2.1 Compressor Printing.

The first printer used in this research to fabricate a compressor was the Stratasys Fortus 450mc, located within AFRL/RQ. This printer is one of the highest-end printers commercially available. This is due to the numerous automated features, large print volume, the heated printing chamber, and the multitude of materials available. The compressors printed with the Fortus 450mc were made out of ULTEM 9085, printed fully dense with the default Fortus settings.

The Onyx-CCF compressor was printed on the MarkForged Mark II printer, located at the Wright-Brothers Institute, Tech-edge. This printer is one of the few printers that can print a variety of continuous fibers separately from the matrix. It can print carbon fiber, Kevlar, fiberglass, and a high-strength, high temperature version of fiberglass. The matrix material, Onyx, is a nylon material reinforced with chopped carbon fiber.

The final material was 300-AMB by 3D-Systems in their Figure-4 printers, located at University of Dayton, Research Institute. These are vat photopolymerization printers that cure an entire layer at a time. Because the curing is done by a projector, it is both quicker than many material extrusion methods and has a significantly higher part resolution. The primary difficulty in using this printer is the relatively small build volume, 124.8 x 70.2 x 196 mm. This means that the compressor could not be printed in the "optimal" direction with the z-direction aligned with the axial direction.

3.3.2.2 Compressor Balancing.

As a rotating object spins, any imbalances in the mass create a force in the plane of rotation. If the center of mass is not aligned with the axis of rotation, a force from the axis to the center of mass must exist to balance the dynamic forces. As the mass rotates around the shaft, this force changes direction, leading to an oscillating stress. Oscillating stresses can cause failure by three mechanisms. The first mechanism is the cyclic loading in the part, the second is by creating a disturbance than can excite natural frequencies during the accelerating spin, and the third way is to cause the local stress to exceed the maximum stress allowed, even while the average stress is below the maximum. For the expected operation of the engines using these compressors, quickly going to full speed and holding there for the majority of the use, the first two mechanisms are of less concern than the third. Because these materials are all expected to be at or near their ultimate strength, any increase in the local stress could lead to a premature failure.

Compressor imbalances form when material deposition is asymmetric around the axis of rotation. Extra material or unplanned voids lead to a center of mass that is misaligned with the center of rotation. In order to shift the center of mass so that it aligns with the center of rotation, a specific amount of mass must be removed from a

specific location along the compressor. Although the process of removing mass is simple, determining how much mass to remove from what location is impossible without the aid of precise balancing machines. The balancing machine required measuring the mass and the diameter of both the compressor and the turbine/shaft, the nominal speed, and the number of turbine blades. The nominal speed and the mass is required to detect when the balancing is within the G-6.3 Balancing Standard. This standard, originating from ISO 1940/1, is recommended for assembled aircraft gas turbine rotors and is in units of mm/s. The looser standard is the G-16 test standard, adequate for individual components of IC engines, while the tighter standard would be the G-2.5 test standard, recommended for turbo-compressors and gas turbines [79].

The balancing stand used an IR interrupt laser to both detect speed and estimate the position of the imbalance. The laser, shown in Figure 61a, must be positioned to detect the reflective paint at the top of the rotation in order to accurately determine position. The balancing stand drove the turbocharger with compressed air and had attachments for oil to run through to prevent running dry. This is shown in Figure 61b. The balance stand, shown in Figure 61c, has precise strain gauges and springs to determine the magnitude and timing of imbalances.

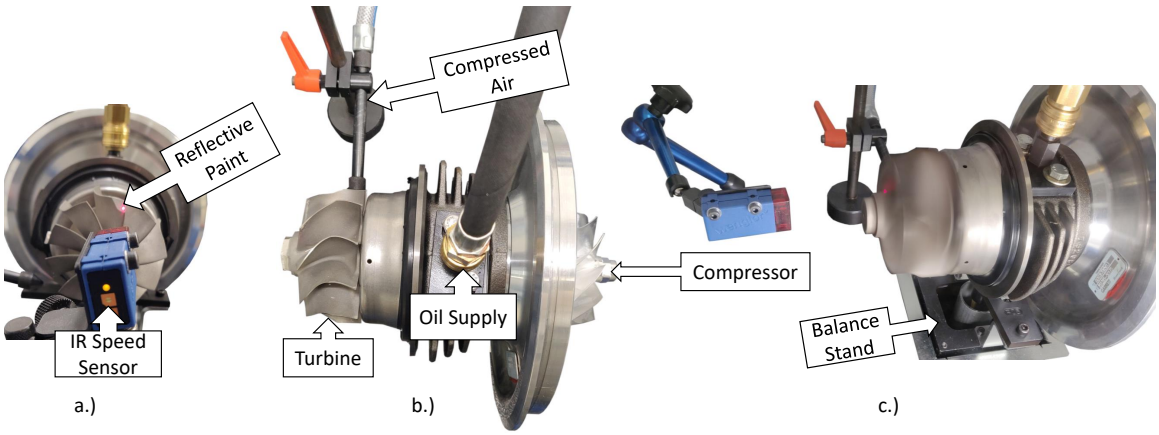

Figure 61. Balancing Test Stand. a.) IR Speed Sensor. b.) Stationary Balancing Stand. c.) Balancing Stand in Action.

After spinning the turbocharger, the balancing stand provided the unbalance magnitude and direction, shown in Figure 62a. The machine is stating that 0.0349 g of material off of the location that aligns with the 8.8 blade position while the compressor requires 0.0137 g off of the area between blades 6 and 7. After removing the proper amount of material from the correct locations, the output is Figure 62b. The green circle describes the region of balance that meets the G-6.3 Standard. Material was removed from the turbine off of the hex on the backend to prevent disrupting the aerodynamics, shown in Figure 62c. However, there was no access to the back end of the compressor. This meant that material was removed from between the blades, shown in Figure 62d. The further distance allowed less material to be removed. This process was accomplished on every compressor that was ran.

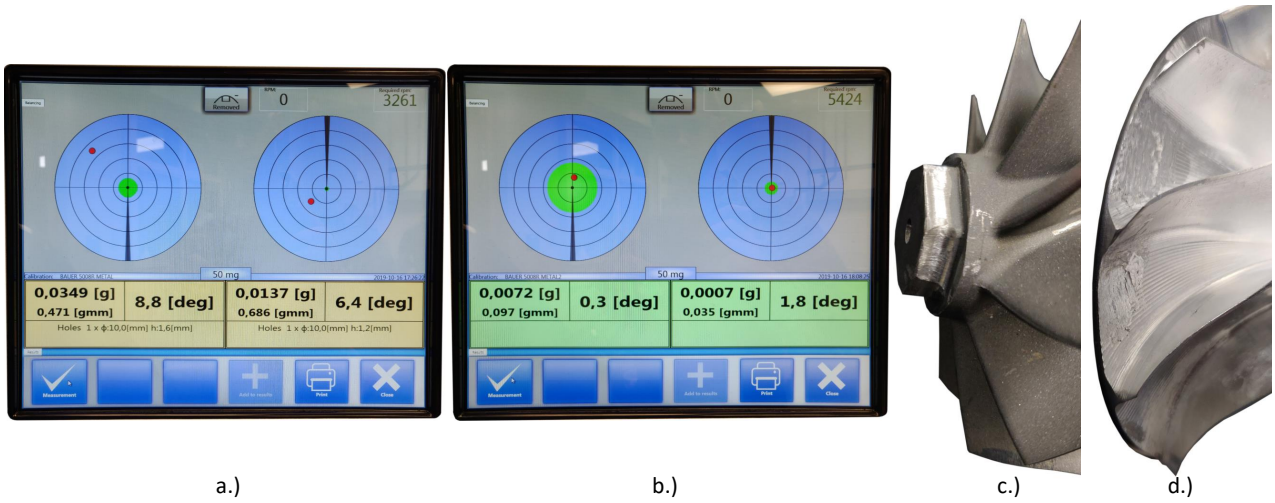

Figure 62. Balancing Test Stand Results. a.) Unbalanced Results. b.) Balanced Results. c.) Balanced Turbine. d.) Balanced Compressor.

IV. Results and Discussion

4.1 Material Testing

The material testing, while not conclusive according to the ASTM standard [55], provided an initial estimation of the material properties that was deemed adequate for the finite element analysis modeling. The results from each of the three materials are presented, with ULTEM 9085 in Section 4.1.1, Onyx in Section 4.1.3, and 300-AMB in Section 4.1.2. Each material has a discussion on measured printer accuracy and repeatability, the material property results, and initial failure mechanisms.

4.1.1 ULTEM 9085 Tensile Results.

ULTEM 9085 is one of the two ULTEM products produced by Stratasys for use in their Fortus 450mc printer. While both are similarly priced, the ULTEM 9085 is typically easier to achieve quality results. However, it has lower published ultimate strength and glass transition temperature. The 10 XZ prints had minimal visible flaws while out of the 15 attempted ZX prints, five were successful. These two directions are shown in Figure 63.

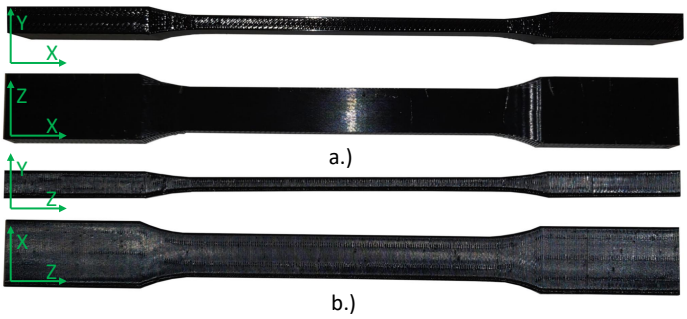

Figure 63. ULTEM 9085 Printed Specimens a.) On-Edge, XZ Build Direction b.) Upright, ZX Build Direction

Mean and standard deviations for the measured cross section are shown in Table 10. The XZ prints had mean measurements 0.01%-1.3% to the design while the

Table 10. Measured vs. Designed Specimen Thickness and Width, ULTEM 9085

ULTEM 9085	Design t, in.	Design w, in.	$\bar{t}$, in.	$\sigma(t)$, in.	$\bar{w}$, in.	$\sigma(w)$, in.
On Edge, XZ	0.160	0.500	0.16003	0.000624	0.50665	0.000669
Upright, ZX	0.160	0.500	0.17026	0.001541	0.51098	0.002274

ZX prints had mean measurements 2.2%-6.4% away from the design. The standard deviation of the XZ prints was 60%-70% lower than the ZX prints.

4.1.1.1 Material Property Results.

The ultimate strength (σ_u) and the modulus of elasticity (E) are the two primary properties used in the FEA. Additionally, these properties vary widely over the expected temperature range. Figure 64a shows the uncorrected stress vs. strain for the nine tested XZ specimens. From this figure, it appears that temperature does not drastically affect the stiffness of the ULTEM 9085, just the ultimate strength. All of the samples failed before a global strain of 0.06 mm/mm. Additionally, the sample at 435 K did not resist tension in any detectable manner; this was compared to the published HDT@1.82 MPa of 446 K and a GTT of 453 K [44].

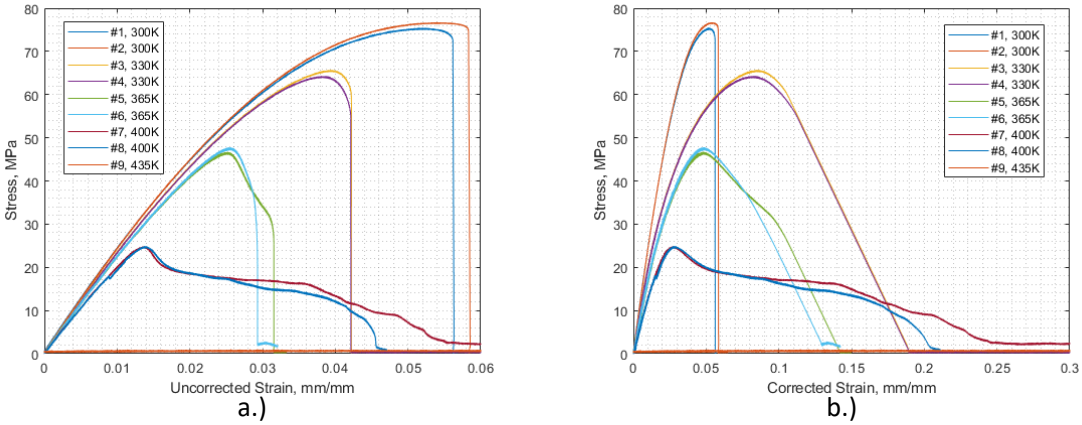

Figure 64. Stress vs. Strain Curves, ULTEM 9085 XZ. a.) Uncorrected Strain b.) Corrected Strain.

When the strain was corrected per Section 3.1.5, as in Figure 64b, the expected differences in stiffness appeared. For the 365 K + temperature specimens, the strain at

the ultimate strength was lower than the 300 K or 330 K specimens. Testing withing the elastic region was more consistent between the specimens than the plastic/failure regions. This is likely because the elastic region was dominated by the continuous "shell" filament rather than the rastered filling. Because the continuous sections were stiffer than the raster in the direction of tension, they took the majority of the stress. The raster was much less consistent than the shell. This meant that once the shell failed, the raster behaved differently between specimens.

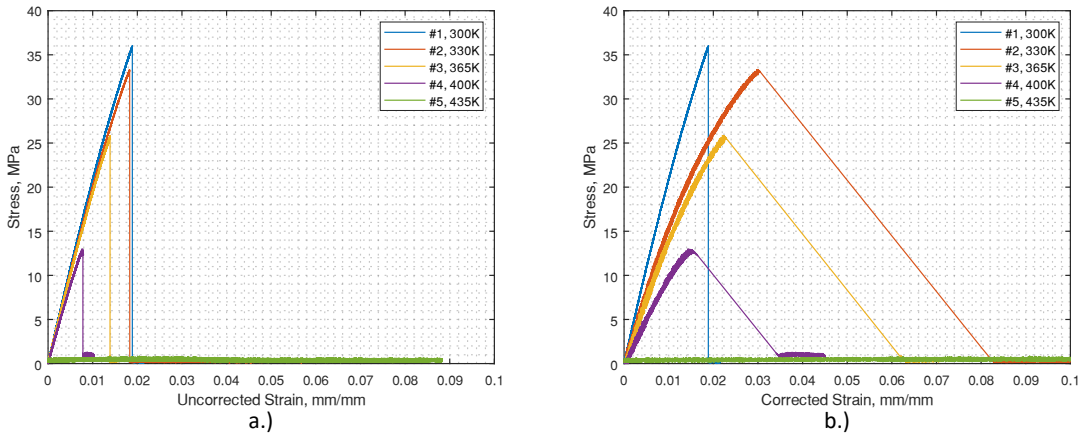

Figure 65. Stress vs. Strain Curves, ULTEM 9085 ZX. a.) Uncorrected Strain. b.) Corrected Strain

The corrected and uncorrected stress vs. strain plots are shown in Figure 65. As with the XZ specimens, the uncorrected stiffness did not vary significantly with temperature. Differences appeared when the strain was corrected. Additionally, the specimen had also no strength at 435 K, with the layers easily pulling apart. In contrast to the XZ specimens, the ZX specimens were significantly more brittle. This was because there were fewer complicated modes of energy storage within the specimen. All of the energy was stored in the bonds between layers; this meant that when failure occurred, there was no secondary region to absorb energy.

Figure 66 is a summary of the tensile test results for ULTEM 9085. The published data closely matched the 300 K, XZ specimens. However, there was a significant dif-

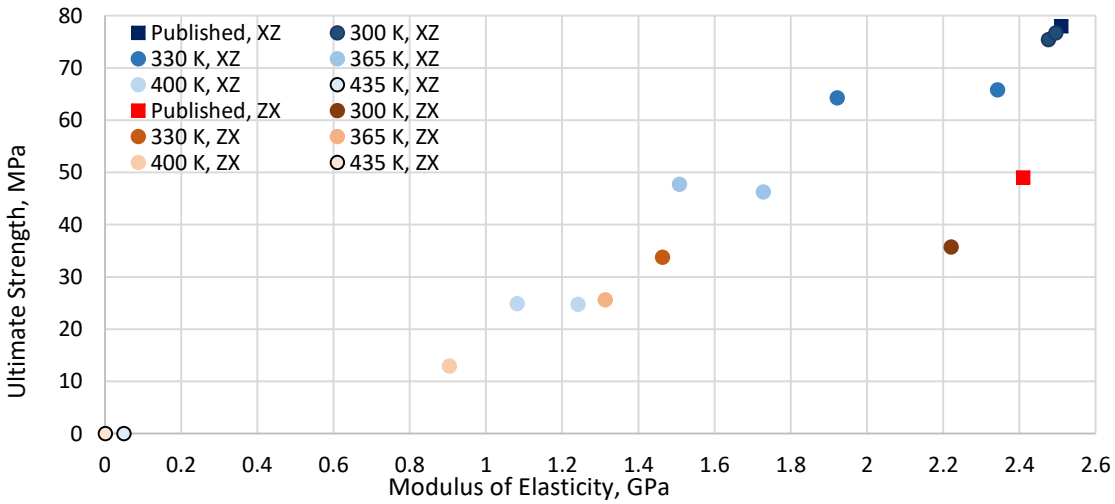

Figure 66. Summary of Material Results, ULTEM 9085.

ference between the published data and the 300 K, ZX directions. This is likely because there are a multitude of different print orientations, rasters, and layers for the XZ specimens and only one layer of adhesion for the ZX directions. Minor imperfections would only slightly weaken the XZ specimens while any minor imperfection drastically affects the strength of the ZX specimens.

4.1.1.2 Plastic Failure Results.

While the data gleaned from the stress-strain curves is what supplied the material properties to the FEA, analyzing the physical specimens allowed a better understanding of what led to failure and how to design AM parts around the various substructures seen within a print. Overall, the strength within a line in the direction of tension was significantly stronger and stiffer than the raster, which was also significantly stronger than the inter-layer adhesion. Brittle failure appeared to be the primary mechanism at lower temperatures while creep overload appeared to be the primary mechanism at higher temperatures.

Figure 67 shows the ten ULTEM 9085 XZ specimens printed with nine specimens tested until failure. Temperature increased from 300 K to 435 K, from left to right.

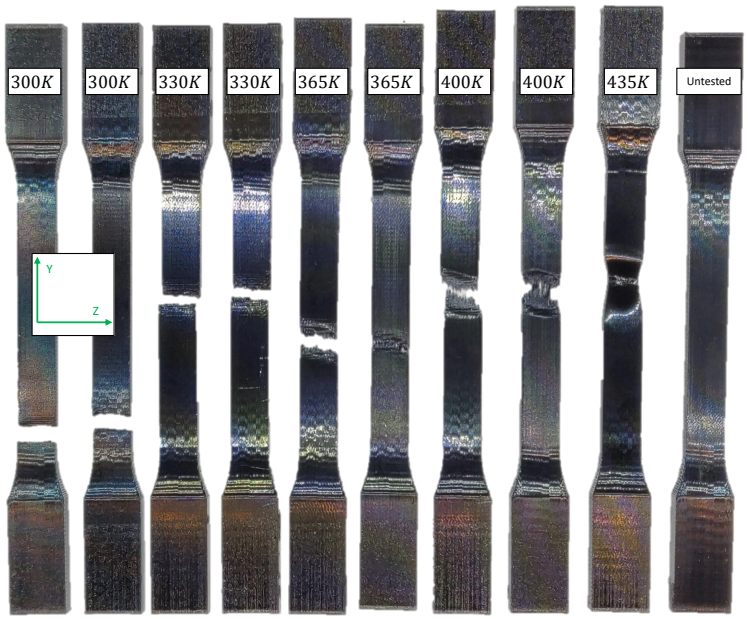

Figure 67. Broken ULTEM 9085 XZ Specimens.

As expected, increasing temperature made the failure region less distinct. The 300 K and 335 K specimens both appeared to fail primarily due to brittle overload. The creep inherent in plastics could not deform the plastic enough to keep up with the designated strain rate. From 365 K to 400 K, the specimens experienced significant necking as plastic deformation occurred. However, the 400 K specimens never had a distinct failure stress over the prescribed strain region, as seen in Figure 64. At 435 K, there was no actual failure because the material deformation occurred at a constant, low stress. Although below the ULTEM 9085 HDT@1.82 MPa of 446 K, stresses around 0.7 MPa led to creep failure.

The ULTEM 9085 ZX specimens exhibited failure differently. This is shown in Figure 68. While the XZ specimens failed across a region, the ZX specimens always failed across a single layer. This was due to the variety of substructures within the cross section. The XZ specimens had 5 substructures: The outer wall internally, the intersection of the outer wall with the $\pm 45°$ raster, the $+45°$ raster internally, the $-45°$ raster internally, and the $+45°$ to $-45°$ intersection. Each substructure con-

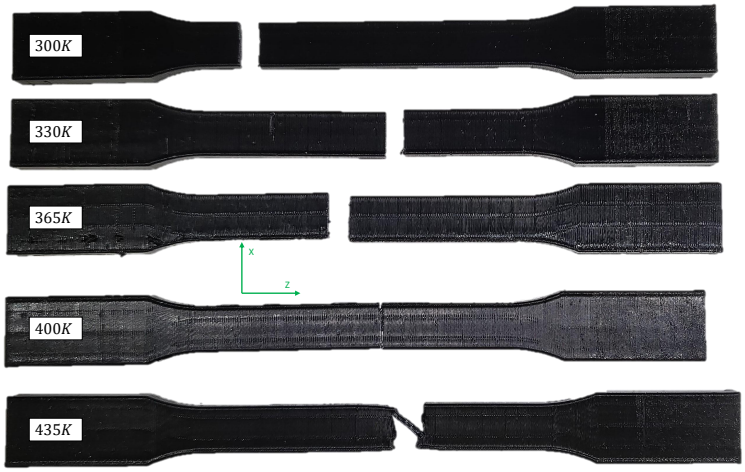

Figure 68. Broken ULTEM 9085 ZX Specimens.

tributed differing strengths, stiffnesses, interlayer adhesion, and stress propagation. In contrast, the ZX cross section only had two substructures: the outer wall layer intersection and the raster layer intersection. The lack of redundant, interdependent structures meant that a single, poorly adhered layer would lead to premature failure; this is regardless of the quality of the other layers. While the XZ specimens acted like a rope with many interlocking structures, the ZX specimens were more like a chain with a single bad link makes the remaining links' strength irrelevant.

A close-up view of the failed cross-section supports the previous conclusions. Figure 69 shows the four XZ specimens that failed during testing. The flat, lighter areas in the 300 K specimen are typical of sudden, brittle failure. Likely, failure began on the left/right edges and slowly propagated as the stress was increased. With each failure, the effective cross-section decreased. This led to a higher local stress. Eventually, local stress exceeded the material strength and failure suddenly occurred. With increasing temperatures, more necking occurred as the PEI polymer chains straightened and lengthened.

The same cross-sections for the ZX specimens is shown in Figure 70. One interesting feature is the fusing or sintering of distinct substructures into larger masses,

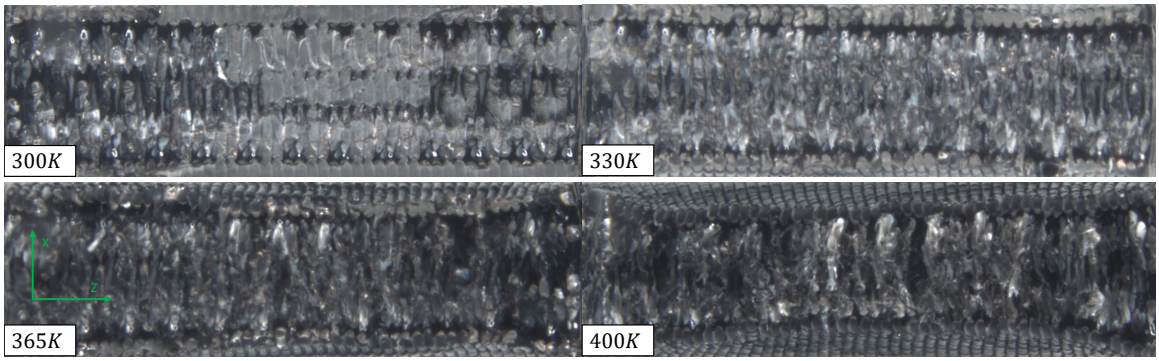

Figure 69. Broken ULTEM 9085 XZ Specimens' Cross-Sections.

most apparent in comparing the 300 K specimen to the 400 K specimen. This fusing is analogous to the sintering of PBF metal. Because the "inter-structure" boundary is typically weaker than the "intra-structure" material, a sintered plastic part could have a more uniform structure. This would be stronger and stiffer. A process called hot, isostatic pressing (HIP) is commonly used to strengthen structures with boundaries and voids by holding the part in a high-temperature, high-pressure oven to fuse the material together [80]. This could raise the standard XZ σ_u from the achieved 76 MPa to closer to 110 MPa - σ_u of solid PEI [29] . A close up comparing the 300 K specimen structure to the 400 K structure is shown in Figure 71.

A close-up of the the side and top of the XZ and ZX, 400 K specimens is shown in Figure 72. Figure 72a shows the aforementioned interdependence between layer in the direction of tension. The lines in the z-direction to the right of the failure plane show slipping within the plane. Figure 72b is a close up of the top of the XZ specimen. Failure did not occur neatly in the Z direction as with lower temperature specimens. The little "hairs" on the piece of the raster left of the failure plan are likely where the raster pulled away from the other raster because the strength within that line of filament was stronger than the interlayer adhesion. Figure 72c. shows the plane of failure from the top for the 400 K ZX specimen. The same "hairs" of failed interlayer adhesion are present here. This failure location had two failures that

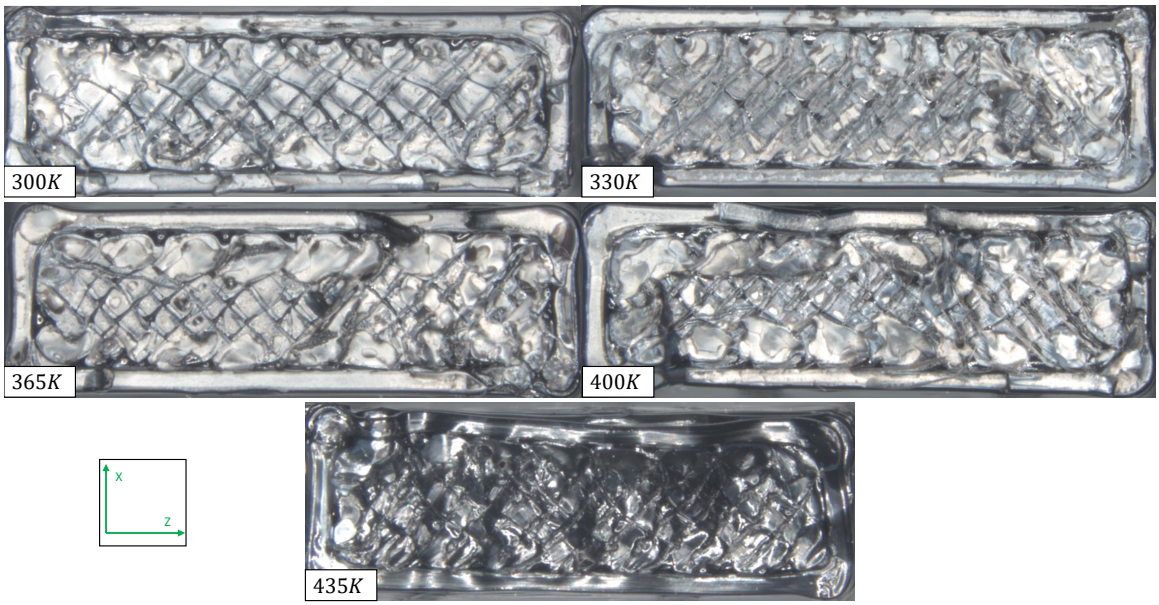

Figure 70. Broken ULTEM 9085 XZ Specimens.

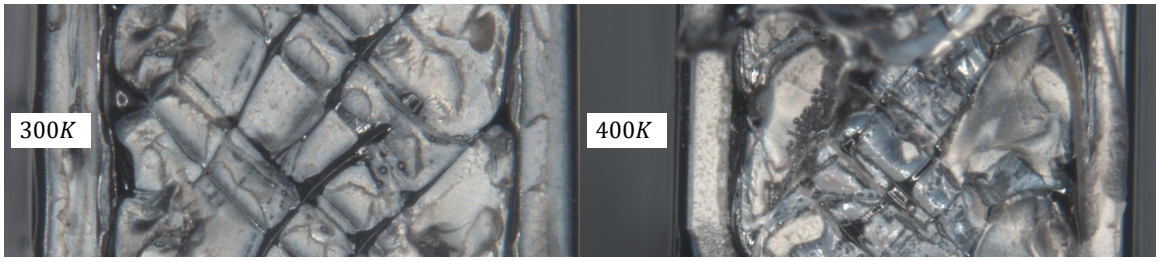

Figure 71. Close-up of ULTEM 9085 ZX Cross Section.

were close to intersecting when the test ended. Both of these layers had deformities that degraded the strength and ultimately led to failure. Finally, Figure 72d shows the same specimen from the top. The failure plane is on the right side of the figure while the center is focused on additional layers that were beginning to fail.

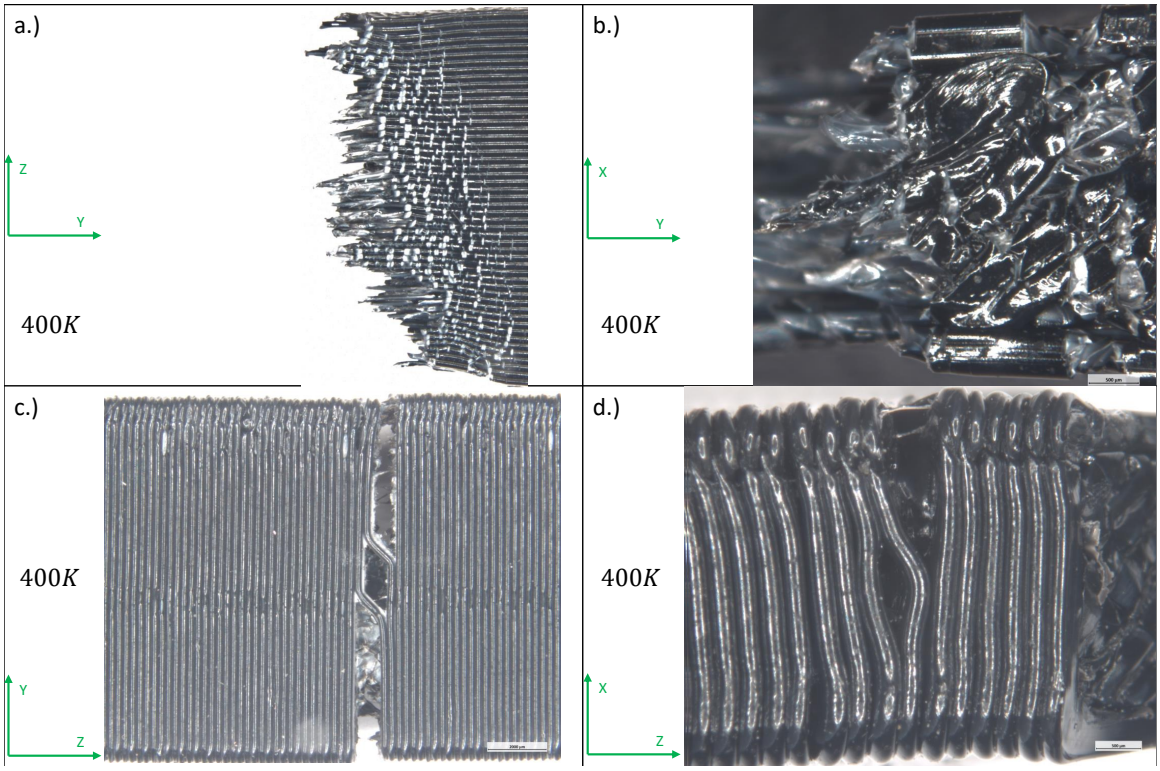

Figure 72. Broken ULTEM 9085 Specimens. a.) Side of XZ. b.) Top of XZ. c.) Side of ZX. d.) Top of ZX.

4.1.1.3 Material Data.

The final material properties used in the FEA model are shown in Table 11 below. E and σ_u were the mean of the tensile testing results. To simplify the FEA, the material was considered isotropic. Although the tensile data shows that this is typically a poor assumption, a test FEA case, shown in Section 4.2.3, shows that the maximum axial (vertical) stresses are around 35% of the maximum radial stresses. Because $\frac{\sigma_{u_{ZX}}}{\sigma_{u_{XZ}}} = 51.3 \pm 2.2\%$ or about $1.5 \times 35\%$ for all temperatures, the material

Table 11. Material Properties for ULTEM 9085, XZ

Temperature	≤300 K	315 K	330 K	347.5 K	365 K	382.5 K	400 K
σ_u, MPa	76.09	70.58	65.07	56.04	47.00	35.92	24.84
E, GPa	2.48	2.31	2.13	1.88	1.61	1.39	1.16
α, 1/K	8.1	8.1	8.1	6.93	5.76	5.76	5.76
ρ, kg/m^3	1,270 Stratasys						
k, W/(m*K)	0.22, MATWEB PEI						
ν	0.44, MATWEB PEI						

can be considered isotropic without drastically increasing the chance of a compressor failure prior to the FEA failure prediction. Published values were used for density (ρ), thermal conductivity (k), and Poisson's ratio (ν) and were assumed constant while the published coefficient of thermal expansion (α) varied with temperature.

4.1.2 300-AMB Tensile Results.

The second material that underwent material testing was 300-AMB. This photopolymer is produced by 3D Systems for high stress, high temperature applications. This material was chosen because of its high published operating temperature and the high published dimensional accuracy of the printer [53]. Ten specimens were printed in the XZ direction at tested at a wide range of temperatures, up to 570 K, its published maximum temperature. A printed sample is shown in Figure 73.

Figure 73. 300-AMB Printed Specimen

Mean and standard deviations for the measured cross section are shown in Table 12. This material had mean measurements 0.8%-1.7% beneath the design. However, the average variation was a few ten-thousandths of an inch. This small variation is important from a design perspective. Although the first print will likely not be

dimensionally accurate, once the part has been properly scaled, the subsequent prints will be within a few thousandths of an inch from the desired dimensions.

Table 12. Measured vs. Designed Specimen Thickness and Width, 300-AMB

300-AMB	Design t, in.	Design w, in.	$\bar{t}$, in.	$\sigma(t)$, in.	$\bar{w}$, in.	$\sigma(w)$, in.
On Edge, XZ	0.160	0.500	0.15722	0.000394	0.49586	0.000135

4.1.2.1 Material Property Results.

The 300-AMB was marketed as a high-strength, high temperature photopolymer. Figure 74 depicts the stress-strain curve for the 300-AMB built "on-edge". The large difference between the two "303 K" tests is believed to be because the first test was under a constantly increasing load while the second test experienced a constant deformation rate. The constant deformation rate is the suggested method in the test standard [55]. Additionally, the 400 K specimen was tested at a constant force rate rather than a constant deformation rate. The final test at 570 K did not record well and this data is an approximation. The data sheet states that "the heat deflection temperature [was] over 300 °C at both low and high stress" [53]. While this was not achieved, linear-elastic performance was achieved at all temperatures up to 500 K.

The elastic modulus versus the ultimate strength at the range of temperatures is shown in Figure 75. Neither of the ambient test specimens was close to the published data. Errors around 50% were seen at ambient conditions. This could possibly be due to microfractures introduced during transportation, slightly angled loading, or varying testing conditions.

While this material was significantly weaker than published, the relationship between temperature and the calculated properties was close to linear for this temperature range. This is shown in Figure 76. The relatively strong linear relationship is

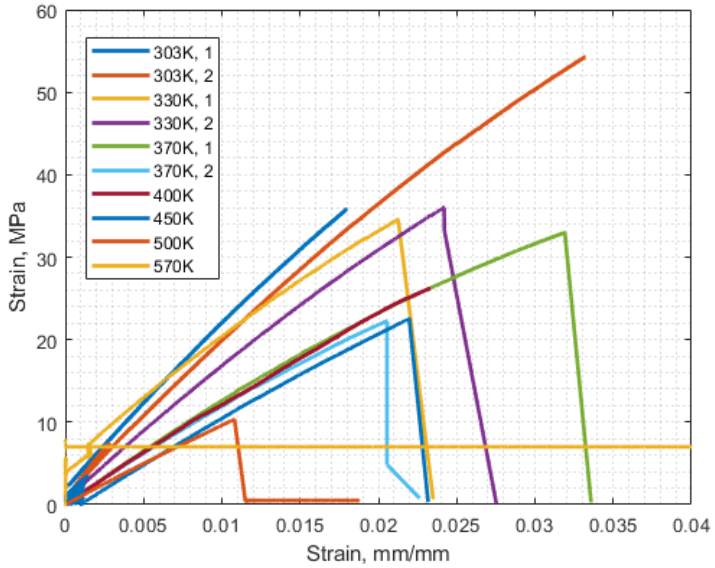

Figure 74. Stress vs. Strain Curve, 300-AMB XZ

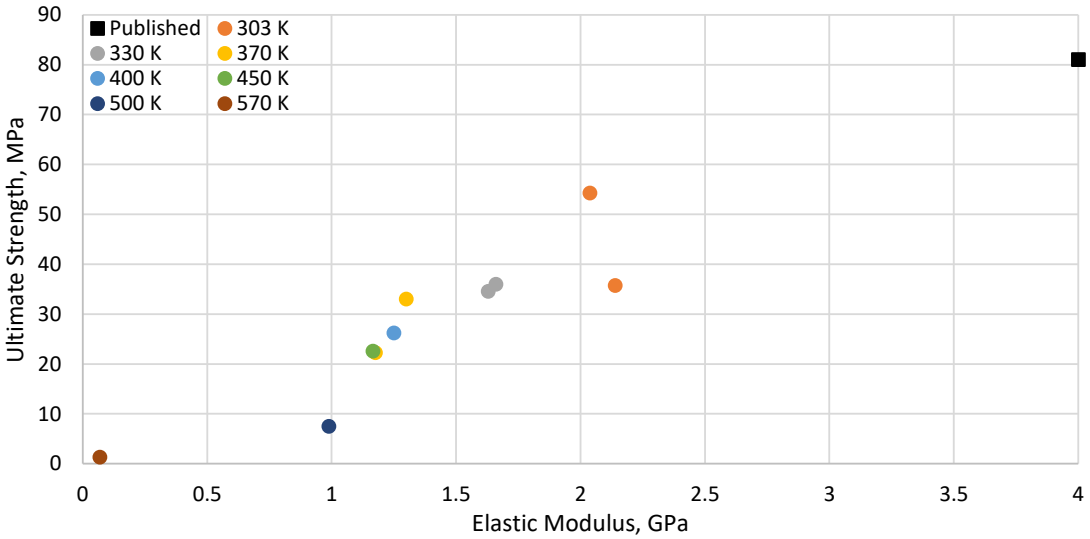

Figure 75. Summary of Material Results, 300-AMB.

useful when estimating properties at a range of temperatures, as seen during finite element analysis.

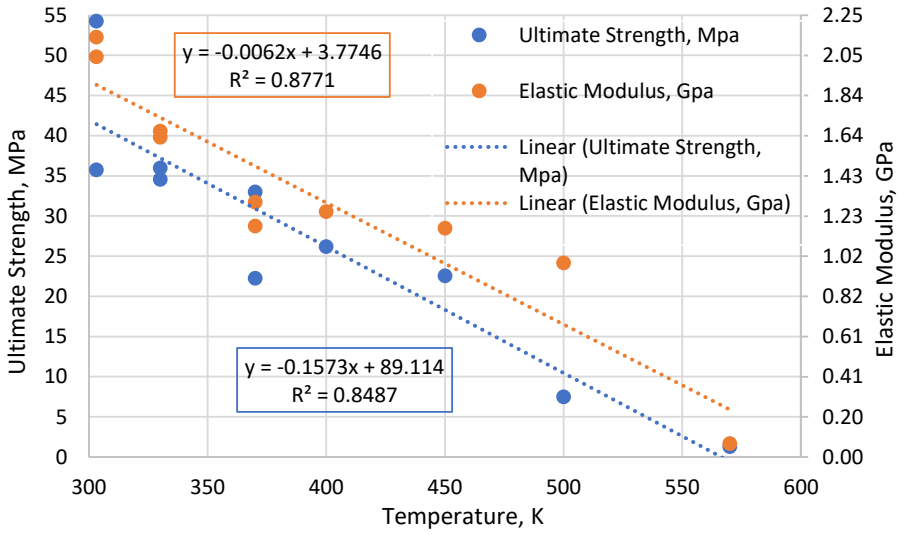

Figure 76. Ultimate Strength and Elastic Modulus versus Temperature for 300-AMB.

4.1.2.2 Plastic Failure Results.

As before, an analysis of the physical fractures provides additional knowledge into the material properties. The type of fracture provides more of an opportunity to design around the limitations to the material than simply the ultimate strength and the elastic modulus as functions of temperature.

Figure 77 depicts the ten broken tensile test specimens with a reference specimen on each side. This is to show the large amount of material that was lost upon rupture. The sharp, jagged edges differs from the gradual elongation and relatively flat failure of the ULTEM 9085 specimens seen in Figures 67 and 68. Forty-five degree failure is typically representative of a slip plane preventing the failure from propagating straight through the material. The vast majority of the specimens lost a significant amount of material upon rupture, breaking apart like glass. Up to 400 K, no lasting temperature effects appear. Starting with the 450 K sample, permanent discoloration

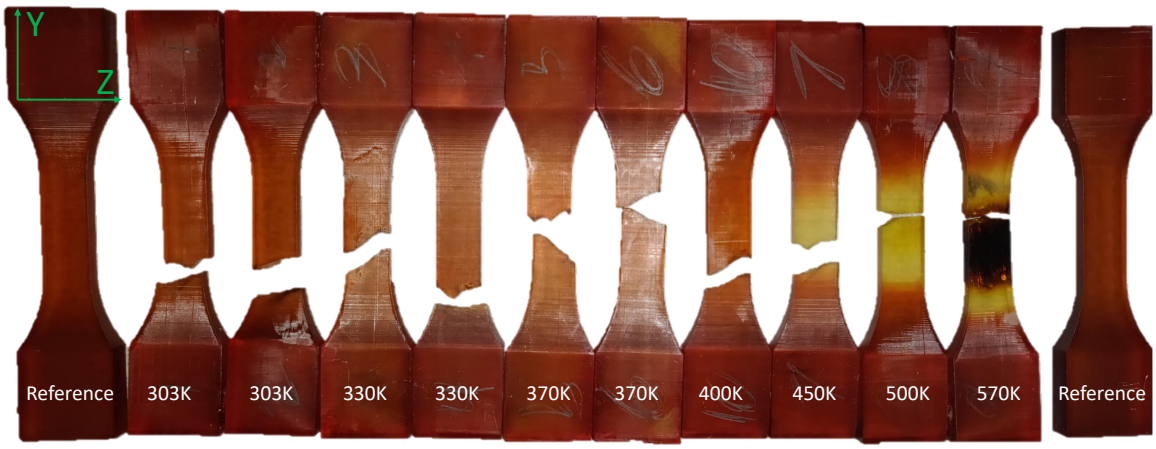

Figure 77. Broken 300-AMB Specimens.

from the high heat is noted. This region continued to spread up and down the sample. The change in color is typically representative of a chemical degradation within the polymer. At 570 K, the high temperature began to char the resin. This sample was the only sample to exhibit any plastic deformation.

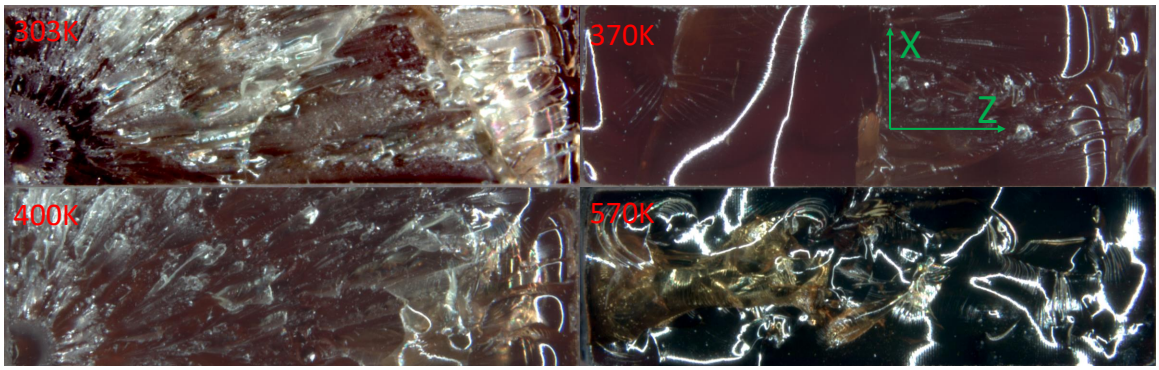

Figure 78. Broken 300-AMB Specimens' Cross-Sections.

As mentioned before, the first 303 K specimen and the 400 K specimen were tested at a constant force rate while the rest were tested at a constant deformation rate. This appears to have led to different types of failures. Figure 78 shows the cross section of four of the specimens at varying temperatures. The two specimens on the left experienced a constant force rate while the two specimens on the right experienced a constant deformation rate. The constant force appears to have initiated

a failure at a single location while energetically spread through the failure plane. The two constant deformation rate specimens failed in such a way that the surface was left much smoother. As before, there is significant thermal degradation of the 570 K specimen. In contrast to the ULTEM 9085, heating the specimen did not lead to any significant change in failure mechanics. All of the fractures were brittle and sudden.

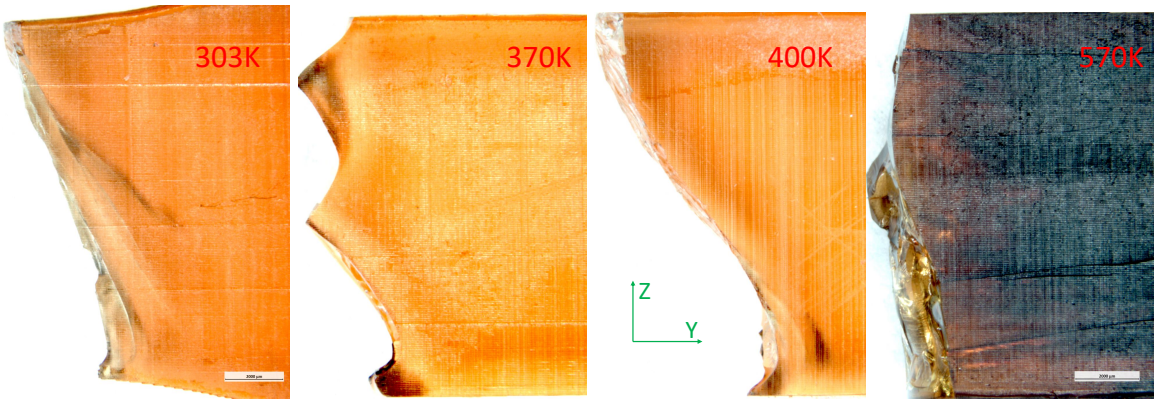

Figure 79. Broken 300-AMB Specimens' Side Profile.

Figure 79 depicts the same four specimens from the side. The same shattered look appears again in the 303 K and the 400 K specimens while the 370 K and the 570 K specimens appear smoother. The 570 K specimen also has horizontal lines cutting though it, likely due to the thermal stresses as it cooled when removed from the furnace. Interestingly, the deeper discolorations within the 570 K specimen do not appear to reach the edge of the failure.

A closer look at the side profile of the 303 K and the 570 K specimens shows two distinct structural features that likely affected the fracture. The first feature is the large lines running in the Y-direction appearing from the building process. From the scale on the image, the layers are approximately 50 μm. This is supported by the material datasheet [53]. The second feature is the vertical lines cutting through the layers from where the cured sections of the projector align. This alignment could provide areas for stress to concentrate, leading to the failure path seen above.

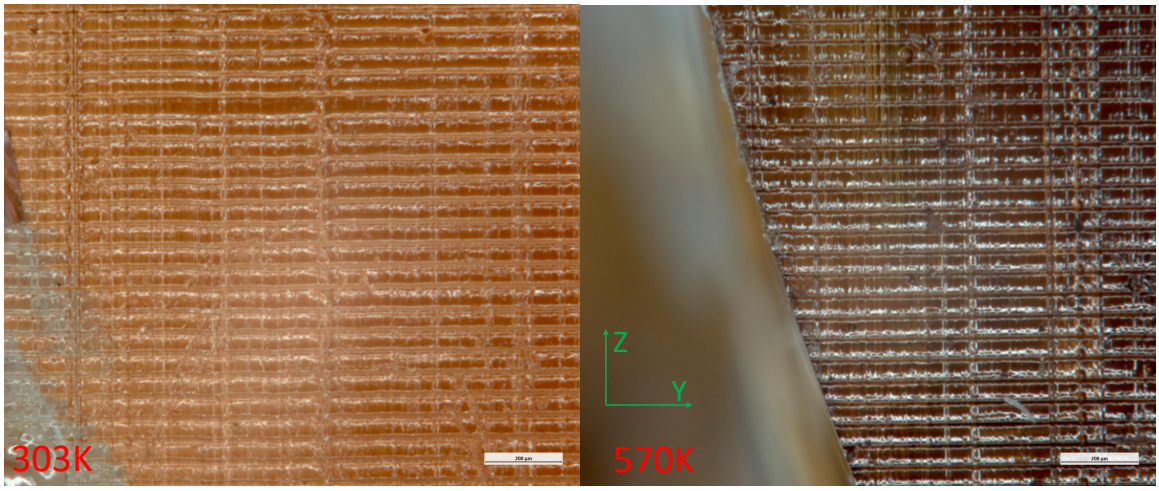

Figure 80. Close-up of ULTEM 9085 ZX Cross Section.

Table 13. Chosen Material Properties for 300-AMB [28, 29, 53]

Temperature	≤300 K	315 K	330 K	347.5 K	365 K	382.5 K	400 K
σ_u, MPa	73.5	69.5	65.6	60.9	56.6	51.6	47.0
E, GPa	2.98	2.82	2.66	1.47	2.27	2.09	1.90
α, 1/K	6.2	6.2	6.2	6.2	6.2	5.4	5.4
ρ, kg/m^3	1,300						
k, W/(m*K)	0.22						
ν	0.4						

4.1.2.3 Material Data.

The final material properties used in the FEA model are shown in Table 13. E and σ_u were the mean of the tensile testing results and the published data. A linear regression was assumed, with the zero-intersect occurring at 570 K. Again, to simplify the FEA, the material was considered isotropic. Published values were used for density (ρ), thermal conductivity (k), and Poisson's ratio (ν) and were assumed constant while the published coefficient of thermal expansion (α) varied with temperature.

4.1.3 Onyx Tensile Results.

The final material was a reinforced plastic called Onyx. Onyx is the proprietary name for the chopped-carbon fiber and nylon blend produced by Markforged. While

the published material properties for it are lower than many other plastics, the primary draw to it is in the Mark II printer's ability to lay continuous fiber reinforcement. The printer first lays down a shell of Onyx and then follows it with a fiber impregnated in a polymer. These continuous fibers dramatically increase the strength of the material. Due to difficulty of obtaining material and the significantly longer time to print, a much smaller number of samples were used to initially characterize the material. Three specimens were printed with Kevlar fiber following the procedure stated in Section 3.1.3. The layer height was roughly half of the ULTEM 9085 layer height, leading to a significantly better print surface quality. This almost-smooth surface finish is seen in Figure 81.

Figure 81. Onyx-Kevlar Printed Specimen

4.1.3.1 Material Property Results.

Of the three materials tested, Onyx-Kevlar was the strongest and stiffest compared to the ULTEM 9085 or the 300-AMB. It also displayed the least thermal effects. Figure 82 is the stress-strain curves for the three specimens tested. Both 300 K specimens failed with 1% of each other. The brittle nature of Kevlar is shown by the sudden failures. Heat did not significantly affect the part because the fibers went into the cooled grips of the MTS machine. This meant that the thermal limits of the Onyx were almost meaningless as essentially all of the load was carried by the fibers.

Figure 83 compares the measured results to the published values. Because Markforged only published the data for their thermoplastic and their fibers separately, it

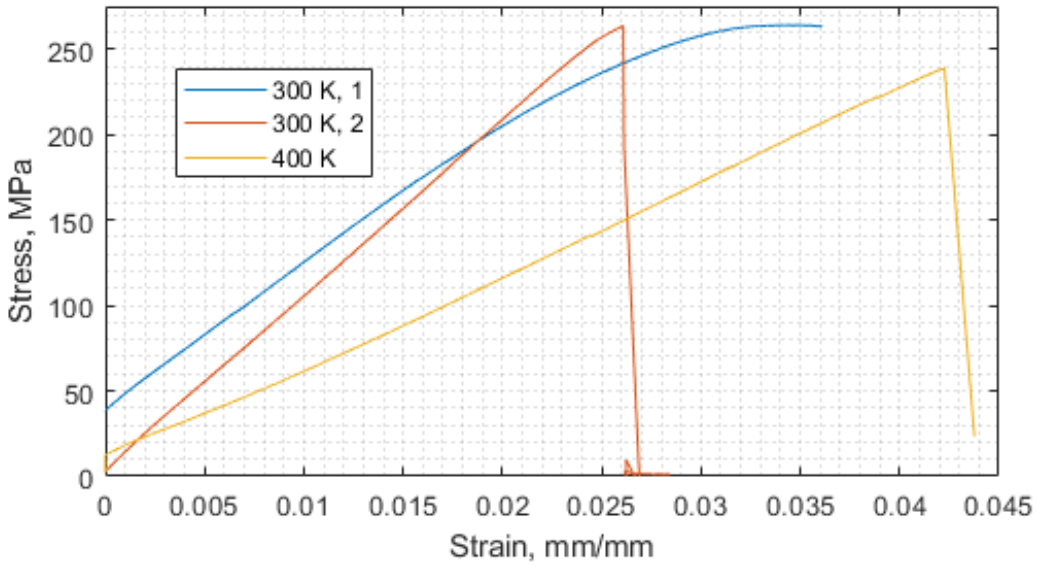

Figure 82. Stress vs. Strain Curves, Onyx-Kevlar.

is more difficult to compare to without making some assumptions. As seen in Section 4.1.3.2, roughly a third of the specimen was Kevlar fibers. By assuming the rule of mixtures applies (See [81]), shown in Equation 74, the test results are shown to have closely aligned with the published data.

$$E_{total} = E_{Fiber} v_{f,Fiber} + E_{Matrix} v_{f,Matrix} \tag{74}$$

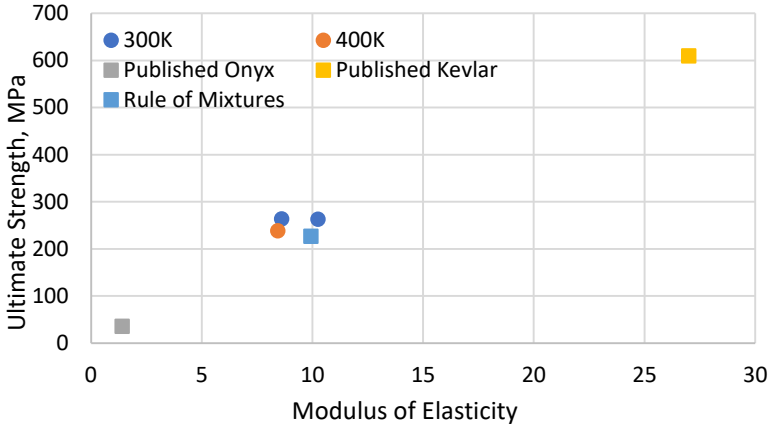

Figure 83. Summary of Material Results, Onyx-Kevlar

4.1.3.2 Plastic Failure Results.

Figure 84 shows the three specimens after tensile failure. While the Onyx failure seems to indicate the location of failure, that is only where the Onyx failed. later analysis showed that the failure occurred within the grips, as the fibers wrapped around a bend. The middle specimen had its grips crushed in the MTS due to too much pressure. The only indication of being heated was that the bottom specimen had ash marks in the middle section.

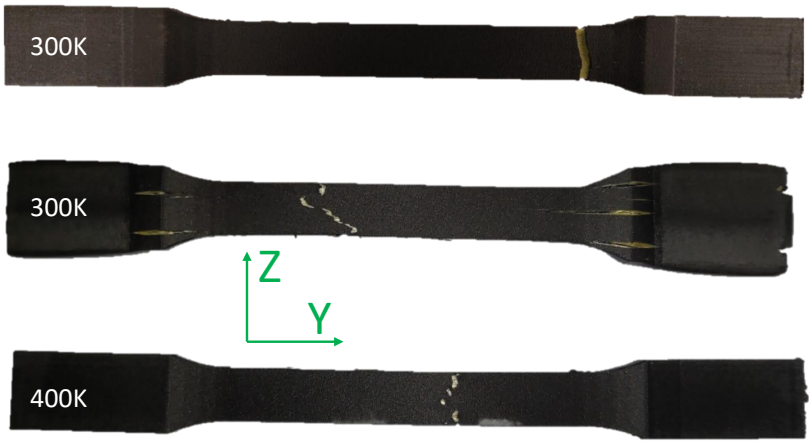

Figure 84. Broken Specimens, Onyx-Kevlar

A close inspection of the first test specimen, shown in Figure 85, shows how the fibers failed around the curve to the grip section. Likely, the high grip pressure fractured the fibers and led to their premature failure. Looking at the XZ plane, the two separate print areas are shown. The concentric fibers in the handle did little to strengthen the structure. All of the stress was resisted by the longitudinal fibers. This knowledge aids in designing using fibers: unnecessary fibers do not prevent failure, they just take up space and increase the cost and time to print.

One specimen was carefully cut through the middle section. Half of the width of the specimen is shown in Figure 86. As mentioned above, roughly a third of the specimen was fiber reinforced while the remainder was Onyx.

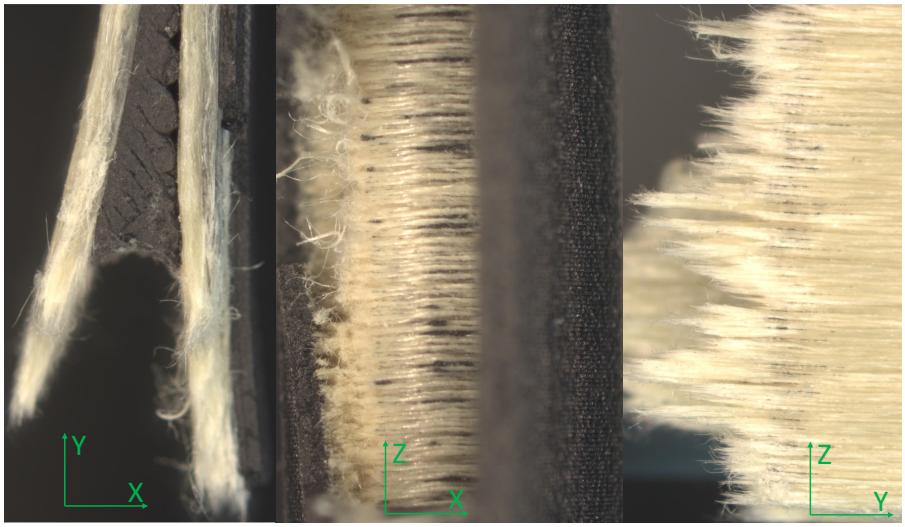

Figure 85. Broken Specimen 1, Onyx-Kevlar

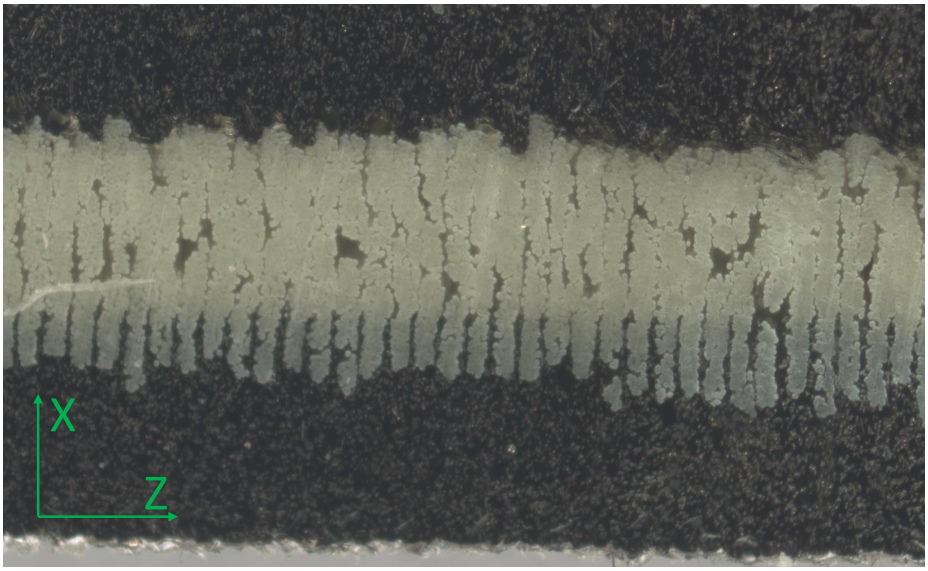

Figure 86. Cut Specimen 1, Onyx-Kevlar

4.1.3.3 Material Data.

The final material properties used in the FEA model are shown in Table 14. E and σ_u were the mean of the tensile testing results. To simplify the FEA, the material was considered isotropic. Published values were used for density (ρ), thermal conductivity (k), coefficient of thermal expansion (α), and Poisson's ratio (ν) and were assumed constant for all temperatures.

Table 14. Material Properties for Onyx-Kevlar

Temperature	≤300 K	315 K	330 K	347.5 K	365 K	382.5 K	400 K
σ_u, MPa	263	260	256	251	247	243	239
E, GPa	8.60	8.58	8.55	8.52	8.49	8.46	8.43
α, 1/K	5.8						
ρ, kg/m^3	1,200						
k, W/(m*K)	40						
ν	0.4						

4.2 Compressor #1: Stock P400 and GTX5008R

Both the stock JetCat P400 and the stock Garrett GTX5008R compressors were analyzed to compare to the printed compressors. The P400 compressor was made from Al 7075-T6 and it was assumed that the GTX5008R compressor was made from the same material in order to perform FEA on the GTX5008R. This is likely a decent assumption because both compressors were aluminum and the Al 7075-T6 is a common turbomachinery metal. The material properties are shown in Section 4.2.1. FEA was performed on both compressors to assess baseline performance. This is shown in Section 4.2.3. Finally, the GTX5008R compressor was operated to validate the published compressor map, shown in Section 4.2.4. Because the stock P400 compressor had a larger diameter shaft than the turbocharger, it could not be physically tested on the test stand.

4.2.1 Material Data.

The material properties used in the FEA were a combination of a study by AFRL [28] and ultimate strengths from Matweb [29]. The material properties are shown in Table 15. A linear interpolation for the temperature-dependent material properties was used to split the properties into five temperatures between the expected high and low temperatures. As before, ρ, k, and ν were assumed to be constant for all temperatures.

Table 15. Material Properties for Al 7075-T6

Temperature	$\leq$300 K	315 K	330 K	347.5 K	365 K	382.5 K	400 K
σ_u, MPa	569	551	533	513	492	430	334
E, GPa	68.8	68.1	67.3	66.7	66.2	65.2	63.8
α, 1/K	2.22	2.24	2.25	2.27	2.28	2.30	2.32
ρ, kg/m^3	2795.7						
k, W/(m*K)	130						
ν	0.33						

4.2.2 Experimental Variations.

The GTX5008R compressor was tested in its stock turbocharger. This was done in an attempt to understand the test setup more thoroughly. While this is the first compressor presented, it was the second compressor tested. This meant that the instrumentation and controls included a variable back pressure valve, a quick shut-off valve, a high-speed camera, and temperature-indicating paint. Due to difficulties with using the infrared speed sensor, the speed data only mapped out the lower region of the compressor map.

4.2.3 Finite Element Analysis.

The finite element analysis for the two stock compressors was not expected to predict failure at the operating speeds. The primary purpose for this round of FEA

was to determine if there were locations that FEA predicted failure that did not materialize in physical testing. The secondary purpose was to prove that the isotropic assumption mentioned in Section 4.1 was acceptable. The stresses in the axial direction for each compressor is shown in Figure 87. The maximum axial stresses were 88 MPa and 34 MPa and the maximum radial stresses were 236 MPa and 124 MPa, for the GTX5008R and P400, respectively. Because the maximum axial stress was between 27%-37% of the radial stresses, respectively, it is clear that the radial stresses dominate the failure analysis and the isotropic assumption is not obviously errant.

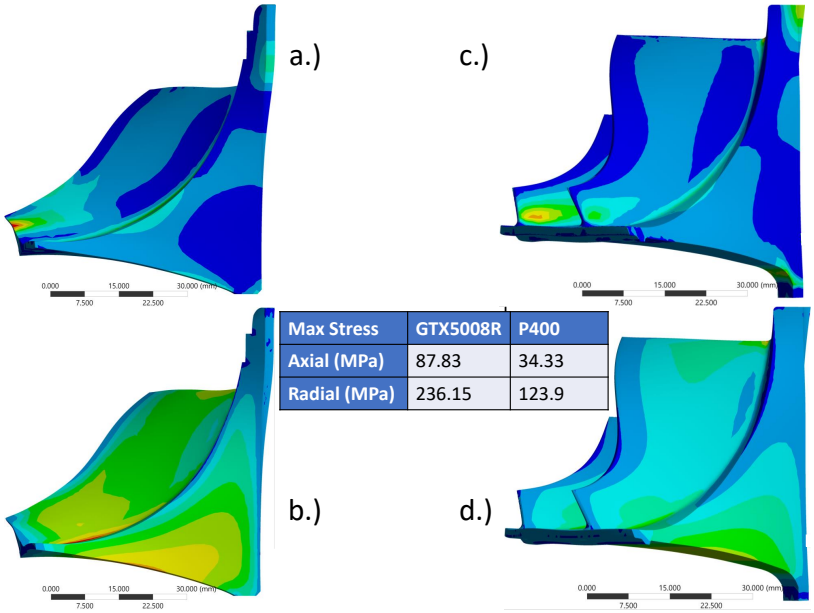

Figure 87. FEA Axial Stresses and Radial Stresses in GTX5008R and P400 Compressor. a.) GTX5008R Axial Stress, 98,000 RPM. b.) GTX5008R Radial Stress, 98,000 RPM. c.) P400 Axial Stress, 50,000 RPM. d.) P400 Radial Stress, 50,000 RPM

4.2.3.1 FEA for JetCat P400 Compressor.

The JetCat P400 compressor was expected to easily withstand the 98,000 RPM as this is operating speed of its engine. Using the temperature boundaries defined in Section 3.2.3, the temperature profile, shown in Figure 88a, is found. At 98,000 RPM, the equivalent stress, shown in Figure 88b, is significantly lower than any

failure stress at any temperature. The maximum stress was 378 MPa at the surface of the bore. This is significantly less than the 513 MPa ultimate strength at that location's temperature. For this reason, the entirety of the P400 compressor at that speed is grayed out - signifying $\sigma_{act_i} < \sigma_{u_i}$, for all locations. In order to estimate a failure speed, the rotational speed was increased until failure occurred. This is shown in Figure 88c. The P400 failure is predicted to occur at 158,000 RPM due to a crack propagating from the bore to the back face of the compressor. Although there is a section of high stress along the base of the blades, this stress did not penetrate through the surface and would not likely lead to failure. Because the same boundary conditions for the 98,000 RPM case was applied to the 158,000 RPM case, this failure speed was only a loose prediction. In order to improve the accuracy of the failure prediction, new temperature boundary conditions would need to be applied. As rotational speed is increased, the exit pressure increases, leading to an increase in the exit temperature. Also, as the compressor blades continue to "fold" outward, they would possibly contact the shroud.

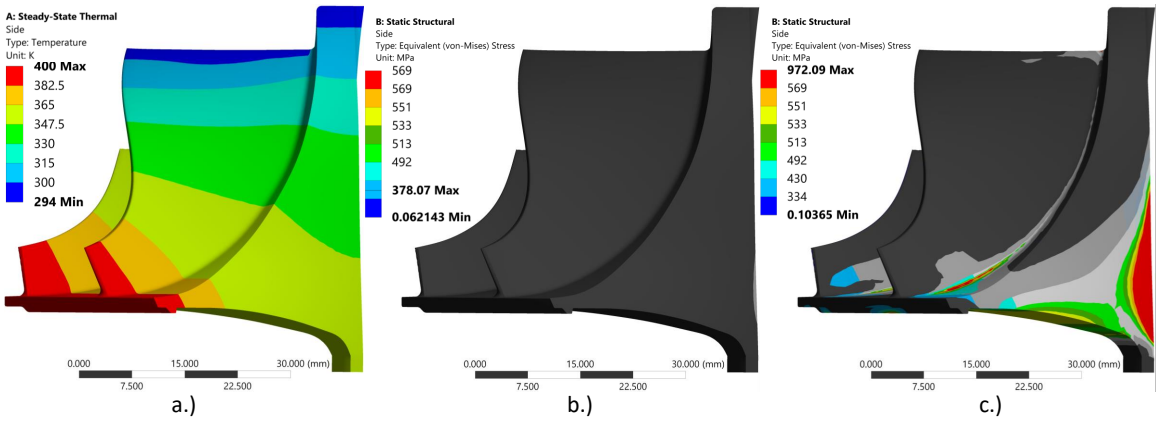

Figure 88. FEA Predicted Temperature and Stress for P400 Compressor, Al 7075-T6. a.) Temperature Profile. b.) at 98,000 RPM. c.) at 158,000 RPM

In addition to a baseline stress profile, a baseline deformation profile is useful for designing compressors. If the stock compressor is expected to deform some distance outwards, that deformation distance should be a safe threshold to prevent blade

impingement on the shroud. The total deformation of the JetCat P400 compressor at the 98,000 RPM operating condition is shown in Figure 89a. The maximum total deformation was 0.23 mm, occurring at the tip of the compressor body. The radial deformation, shown in Figure 89b, is the amount the compressor was predicted to expand in the outward/radial direction. The maximum radial deformation was 0.18 mm, also occurring at the outer edge of the compressor. Radial expansion in the curved part of the blade edge could lead to the blades contacting the shroud. While expansion in the lower part of the blades could be acceptable in the turbocharger setting, the P400 engine had diffusor vanes set close to the compressor blades. The deformation in the axial direction was a maximum of 0.03 mm, seen in Figure 89c. This is smaller than the tolerances of these compressors and can be assumed negligible. However, if the blade tips rise excessively, it could lead to impingement on the shroud.

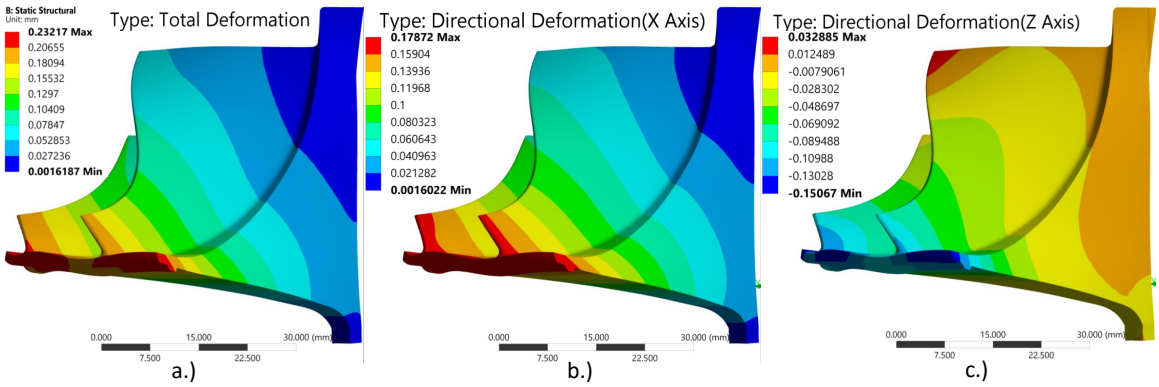

Figure 89. FEA Predicted Deformation for P400 Compressor, Al 7075-T6. a.) Total Deformation. b.) Radial Deformation. c.) Axial Deformation.

4.2.3.2 FEA for Garrett GTX5008R Compressor.

The FEA results from the Garrett GTX5008R compressor were unsurprisingly similar to the P400. The thermal profile, seen in Figure 90a, had similar isotherms with the exception of the 330-347.5 K isotherm. This isotherm was shifted down from the P400 case. As shown in Figure 90b, the GTX5008R compressor was expected

to easily withstand the 98,000 RPM operating case. The maximum stress at 98,000 RPM for the GTX5008R was slightly lower than the P400; 361 MPa compared to 378 MPa. However, due to the variation in conduction through the GTX5008R model, the temperature was lower in the bore so the allowable stress was higher, 533 MPa compared to 513 MPa. Using the same process as before, the rotational speed was increased until failure was predicted at 167,500 RPM, an increase of 8,500 RPM compared to the JetCat P400. The primary cause of the increased rotational speed was the significantly larger radius of curvature on the back face of the GTX5008R compressor.

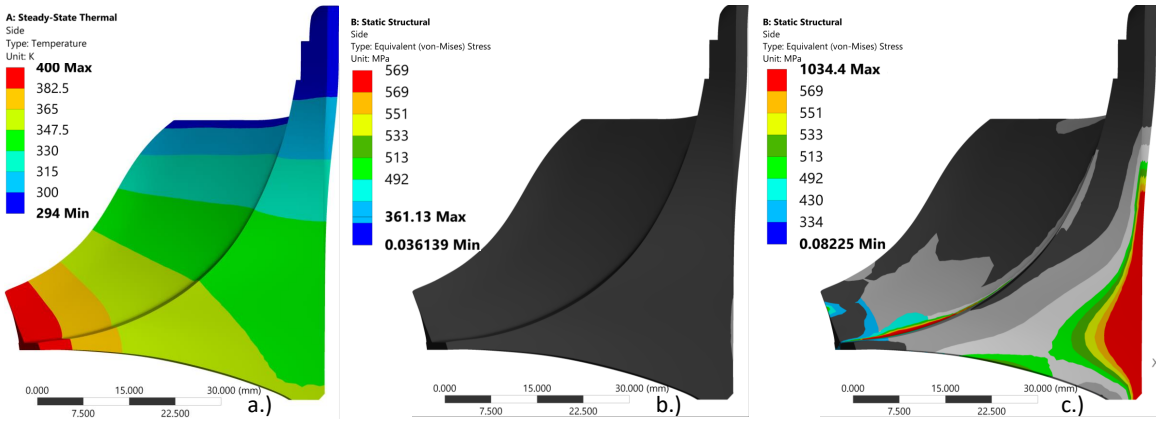

Figure 90. FEA Predicted Temperature and Stress for GTX5008R Compressor, Al 7075-T6. a.) Temperature Profile. b.) at 98,000 RPM. c.) at 167,500 RPM

Figure 91a depicts the total deformation for the GTX5008R compressor. Unsurprisingly, it was only slightly less than the total deformation of the P400 compressor (0.223 mm to 0.232 mm). However, the axial deformation in Figure 91b increased from 0.179 mm to 0.192 mm. The location of maximum stress moved from the entire outer section in the P400 to just the tips of the blades. Additionally, the maximum axial stress increased from 0.033 mm at the top of the P400 blades to 0.094 mm at the outer edge of the GTX5008R compressor, between blades. This was likely due to the removal of a balancing ring present in the P400. This balancing ring provided

a region behind the compressor surface from which to remove material rather than from a surface exposed to the flow.

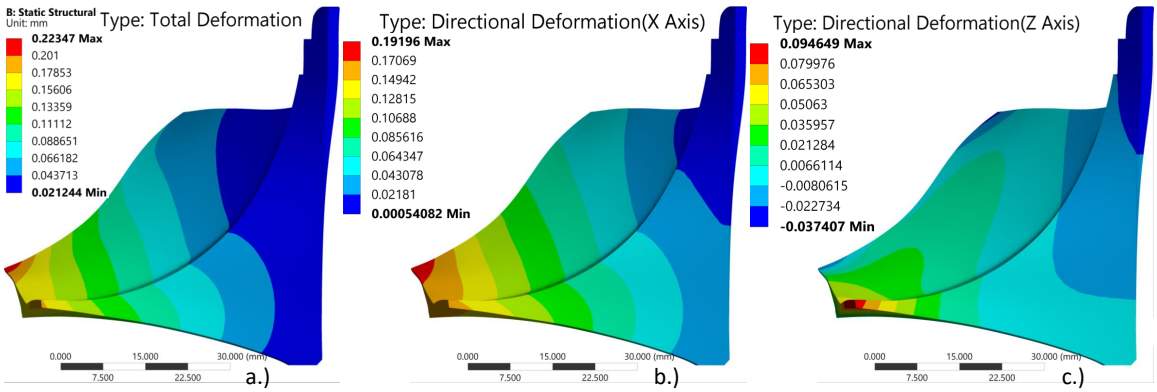

Figure 91. FEA Temperature and Stress Results for GTX5008R Compressor, Al 7075-T6. a.) Temperature Profile. b.) at 98,000 RPM. c.) at 167,500 RPM

4.2.4 Performance Analysis.

The physical testing of the GTX5008R had the primary purpose of characterizing a stock turbocharger to compare with the AM compressors. However, during these runs, numerous errors accumulated. At high speeds, the IR speed sensor froze due to the expansion of the incoming turbine air. After long runs, a pressure tube on the compressor exhaust melted from the heat and gave errant readings. This limited the useable data to what is shown in Figure 92. To clean up the RPM data, a moving average filter was applied averaging the 50 data points surrounding the measurement. While this decreased the ability to determine transient effects, it allowed better conclusions to be drawn correlating speed to other variables.

Figure 93 shows the RPM versus the pressure ratio for the region of useable data. Where the pressure ratio closely follows the RPM trend, the variable valve was fixed. Where the pressure ratio changes differently from the RPM, the valve was adjusting to reach a desired setting.

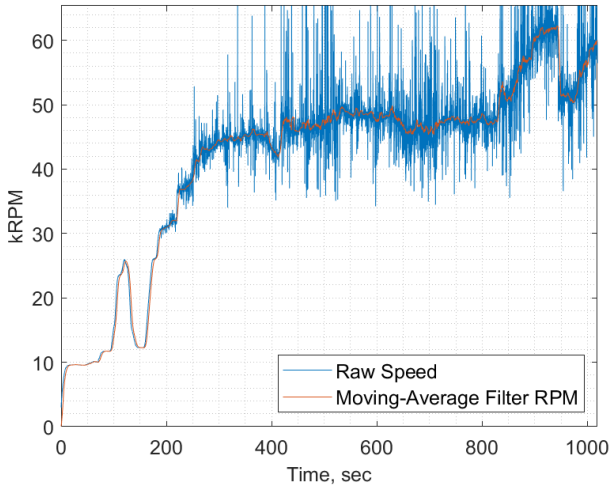

Figure 92. Raw versus Averaged RPM Data, Stock GTX5008R

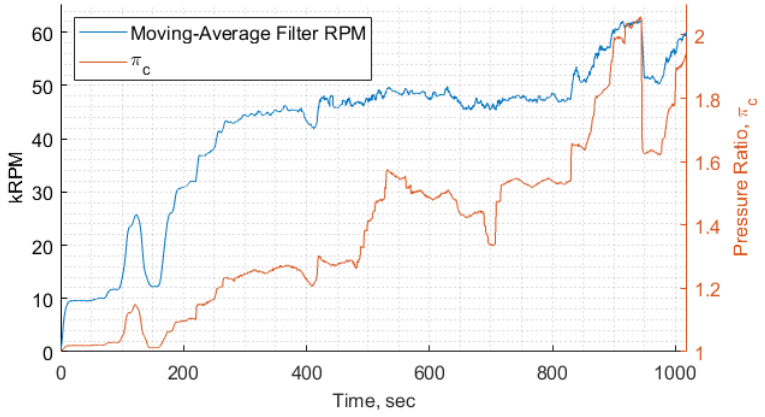

Figure 93. Compressor Pressure Ratio versus RPM, Stock GTX5008R

Efficiency is one of the more difficult compressor parameters to measure. Due to the form of the uncertainty equation (Section 2.4.5), at lower speeds near 30% of the maximum speed, the efficiency uncertainty is commonly ± 20% [36]. Another issue is that during any transient condition, the efficiency is unknown. At lower speeds, the metal of the turbocharger and piping is relatively cold. If the turbocharger suddenly speeds up, the pressure ratio will respond fairly quickly. However, the cold metal will absorb heat from the flow, artificially lowering the temperature of the airflow. Because the efficiency is calculated based on the difference between the actual temperature rise and the ideal temperature rise, heat transfer from the flow increases the indicated efficiency.

This increase in efficiency due to the heat uptake is seen clearly in Figure 94. While the compressor was warming up at low speeds, the efficiency was greater than 100%. Any time the valve was shut, the same effect occurred and the efficiency would appear to shoot up as the new thermal gradient developed. From 12 kRPM onward, the efficiency values were close to the expected values.

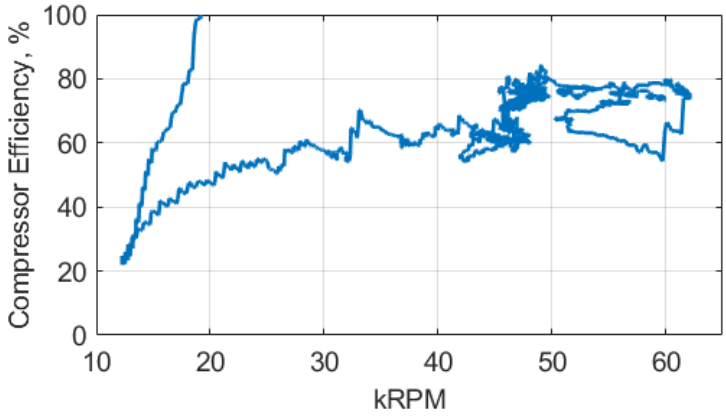

Figure 94. Compressor Efficiency versus RPM, Stock GTX5008R

A compressor map is a common way to describe the operating region of a certain compressor. Figure 95 is the GTX5008R compressor data overlaid onto its published map [11]. This overlay clearly shows the operations of the turbocharger run. From

the start to 45 kRPM, the compressor was spun with a constant back-pressure valve setting. With the valve fully open, the compressor was choking and was following the choke line on the right boundary. At 45 kRPM, the back–pressure valve was adjusted to increase the pressure ratio to around 1.5. Following this, another constant back-pressure increase in speed occurred. At this point, the RPM sensor cut out from freezing and the pressure tubing melted.

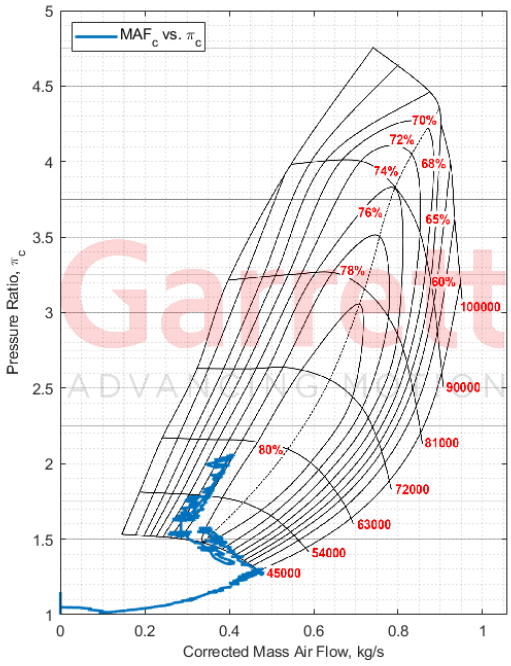

Figure 95. Compressor Map for Stock GTX5008R

The amount of work that the compressor adds to the flow compared to the amount of work that the turbine removes from the flow is an important metric related to efficiency. The ratio of the work removed by the turbine to the work added to the flow by the compressor is the turbomachinery efficiency and includes the many losses associated with compressing and expanding air. The difference between the turbine work to the compressor work is the actual friction power losses. However, due to the many steps needed to convert from basic measurements to power (Pressure → Pres-

sure Differential → Velocity → Mass Air Flow → Power) the accumulation of errors means that poor initial measurements can result in meaningless the calculated power. This is shown in Figure 96. The only set of measurements that provide a possible condition with positive friction is comparing the "Cold" total-static measurements. The other two sets of data have calculated turbine power lower than the calculated compressor power.

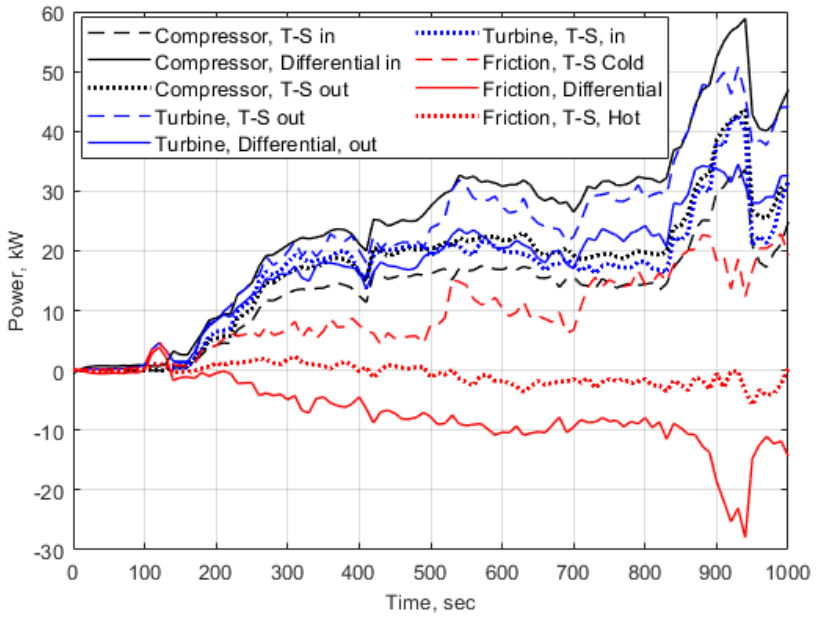

Figure 96. Compressor Work, Turbine Work, and Frictional Losses, GTX5008R

In order to better understand failure, a high-speed camera was installed. This camera was able to provide dozens of frames per compressor revolution. While the ULTEM 9085 compressor catastrophic failure occurred before camera installation, it is also a useful tool for verifying rotational speed. When this compressor was near 60 kRPM, the speed sensor cut out. By triggering the high-speed camera, the speed data was collected, shown in Figure 97. From Figure 97a-Figure 97b, 22 frames elapsed. At the 22,000 frames per second record rate, the compressor was shown to be at 60,000 RPM.

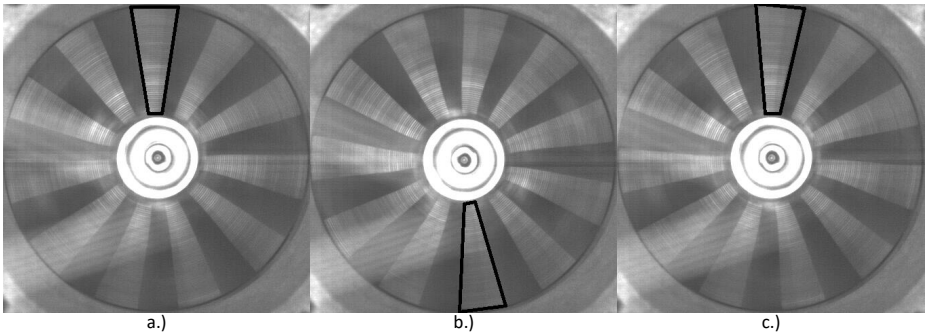

Figure 97. GTX5008R High-Speed Camera Footage. a.) Frame 1. b.) Frame 11. c.) Frame 22.

In FEA, the results depend primarily on the boundary conditions. One difficult boundary condition to obtain is the back face temperature of the compressor. By using temperature-indicating crayons, shown in Figure 98, an initial estimate of the back face temperature distribution was obtained. Each color crayon melted at a specific temperature. This means that if crayon remained, the surface did not reach the crayon's melting temperature. While this initial effort had numerous, accumulating errors, it demonstrated a method that could be done more precisely and more quickly to gather useful data. The largest source of error in this test was that the compressor was not quickly cooled after running and before examining the crayons' markings. This allowed heat to conduct towards the center of the compressor and melt off crayon that would not have melted during operation.

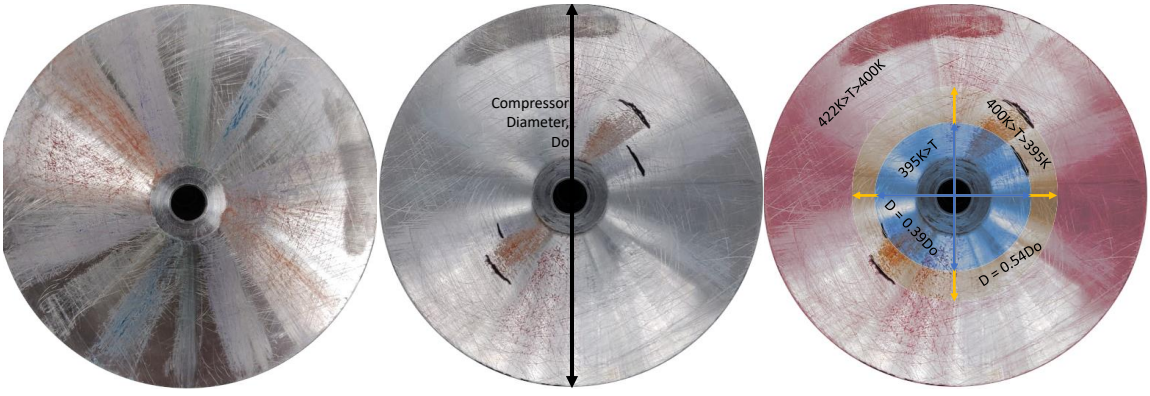

Figure 98. GTX5008R Back Face Heat Map. Before Test (left). After Test (middle). Digitally Colored (right).

4.3 Compressor #2: JetCat P400, ULTEM 9085

Due to the access and ease of printing with ULTEM 9085, it was the first material chosen for an AM compressor. Although the ULTEM 9085 compressor was not expected to withstand the full 98,000 RPM, it was expected to fail at a high enough speed to collect meaningful pressure and temperature measurements. The following section discusses experimental (Section 4.3.1) and compressor (Section 4.3.2) modifications. Section 4.3.3 covers the FEA on the compressor model, Section 4.3.4 attempts to determine the mechanism of failure, and finally, Section 4.3.5 compares the performance of the compressor to published data.

4.3.1 Experimental Variations.

This was the first compressor fully tested. The variable butterfly was set to 38deg based on an initial run of the GTX5008R compressor. This value was chosen because it set the turbocharger operations near the center of its published compressor map, which also aligned with the P400 compressor op line from Grannan [36]. Due to initial difficulties providing enough air flow to drive the turbine, only the bottom section of the compressor map was reached. Additionally, the butterfly valve was difficult to set and fix the butterfly valve to the desired angle. This meant that only a few attempts were initially made to set the valve at the ideal angle. Because the ULTEM 9085 shrunk around 0.2 mm when it initially cooled, the compressor had to be press-fit onto the turbocharger shaft with an arbor press. However, this press-fit provided the friction needed to avoid slipping of the compressor on the shaft.

4.3.2 Model Modifications.

Because the goal for this round of modifications was to change the compressor as minimally as possible, there were only three modifications to the original JetCat P400

model. The radius was decreased from 9.96 mm to 9.47 mm to allow the compressor to fit snugly on the turbocharger shaft. The original CAD model had a sharp blade-body interface angle. This was to aid in varying the fillet to any beneficial size. For this compressor, the fillet radius was set to a constant 1.02 mm. This approximately matched the fillet radius of the JetCat P400 compressor. The final modification was the lengthening of the shaft body an additional 2.327 mm. This was because the shaft of the GTX5008R was longer than the P400. Without this additional length, the P400 compressor would scrape the back plate. These three changes are shown in Figure 99 below. The final print is shown in Figure 100. The layers are visually large with this printer in comparison to other printers.

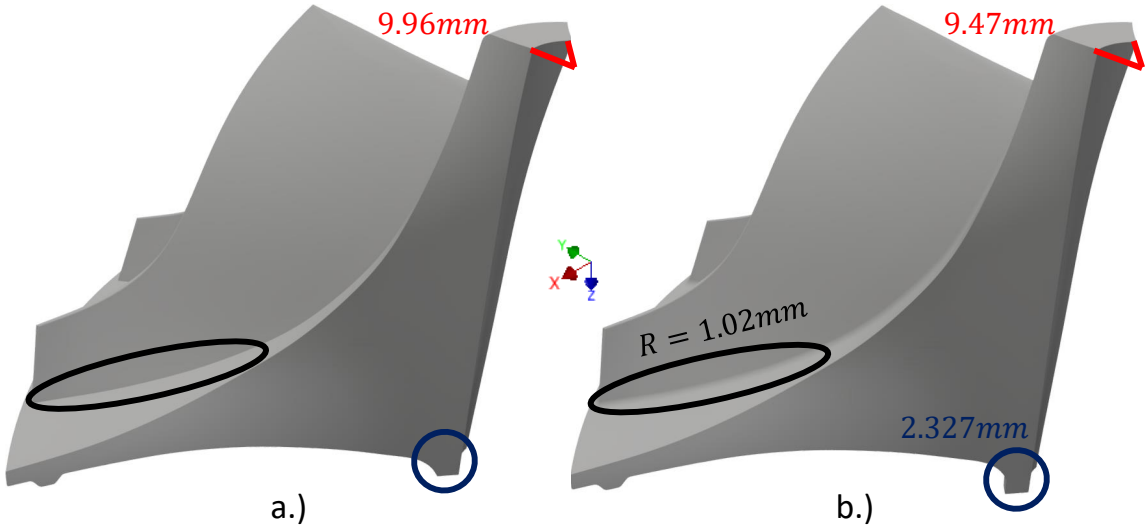

Figure 99. Modifications of P400 Compressor for ULTEM 9085. a.) Original JetCat P400. b.) Modified ULTEM 9085 P400.

4.3.3 Finite Element Analysis.

The initial FEA on the P400 compressor made from ULTEM 9085 used the thermal and rotational conditions expected from 98,000 RPM rotation. Figure 101 depicts the thermal profile of the compressor with the boundary conditions mentioned in Section 3.2.3.

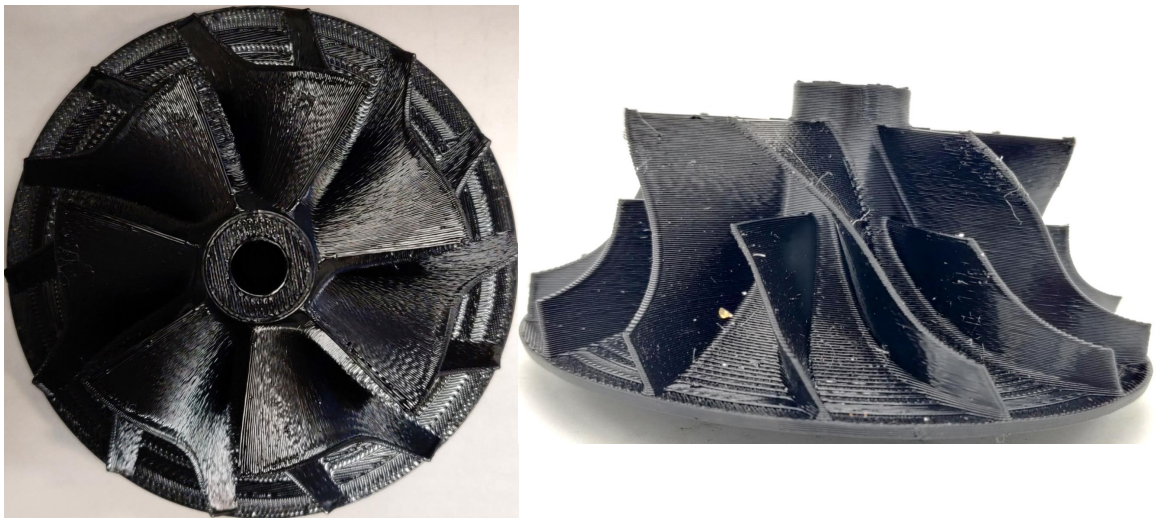

Figure 100. Printed Modified P400 Comressor, ULTEM 9085

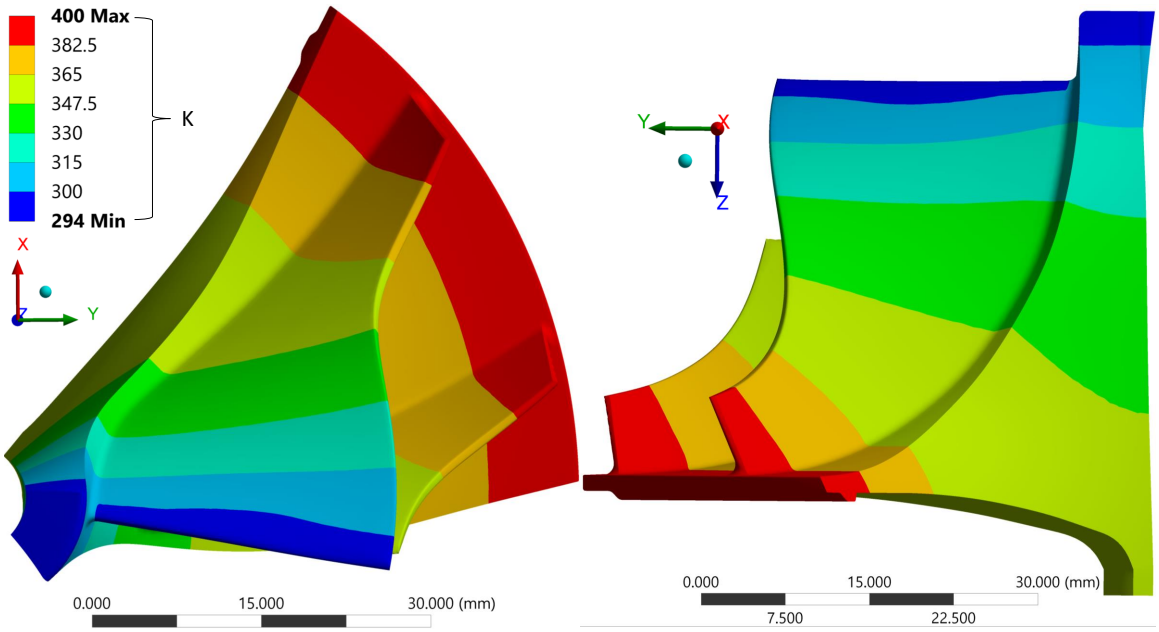

Figure 101. Top and Side Thermal Profile for P400 Compressor, ULTEM 9085.

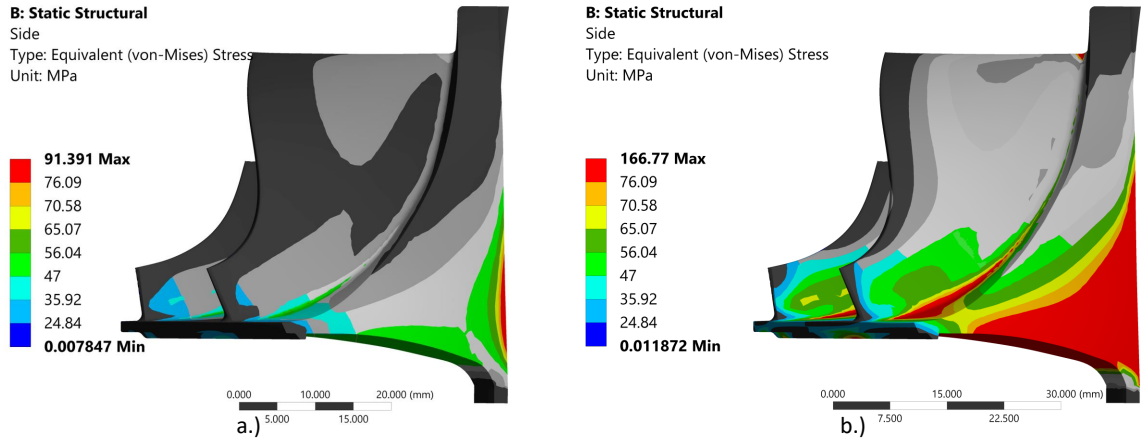

Figure 102. Equivalent Stress Profile for P400 Compressor, ULTEM 9085. a.) 72,375 RPM. b.) 98,000 RPM.

The final results, shown in Figure 103, show the predicted deformation of the ULTEM compressor. The maximum deformation of the stock P400 compressor was predicted at 0.23 mm (Figure 89). The maximum deformation expected with the ULTEM 9085 compressor was predicted at 3.3 mm, more than 10x larger than the stock Al compressor. This exceeds the radial tip clearances and impingement was expected.

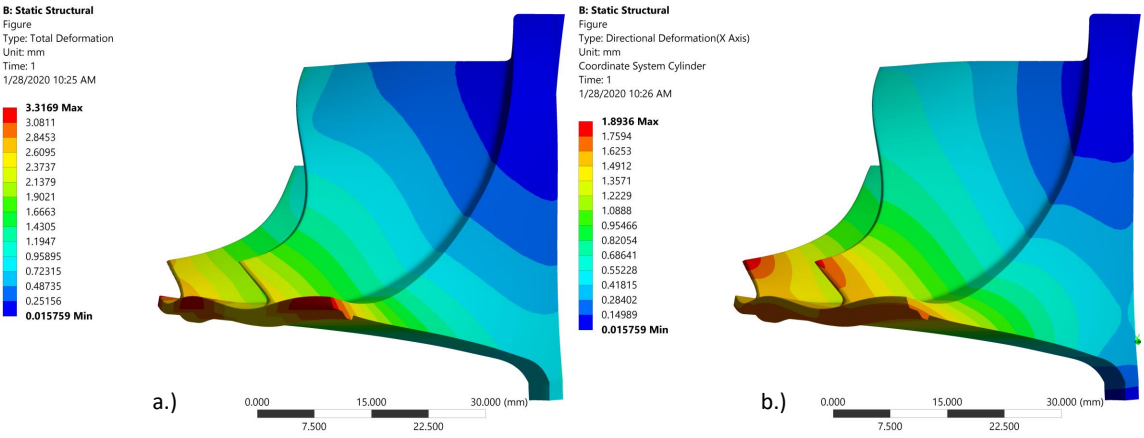

Figure 103. Deformation Profile for P400 Compressor, ULTEM 9085 at 98,000 RPM. a.) Total Deformation. b.) Radial Deformation.

4.3.4 Failure Analysis.

While FEA predictions seemed to provide a clear answer to the failure speed, the many simplifications meant that some form of validation must be accomplished prior to determining the adequacy of the design. If success had been defined as withstanding the loads of 98,000 RPM rotation, this compressor would have been a failure. However, one of the primary goals of this research was to determine whether or not FEA could be used to predict compressor failure and meeting this goal required failure. Complete failure was determined to have occurred when the pressure ratio dropped to 1.0 - either the compressor broke through the bore or the blades sheared off.

Precisely determining the part of the compressor that failed initially was difficult because there was no visual evidence of the failure. Because of the large amount of kinetic energy of the compressor at the failure speed, the initial failure was likely followed by numerous other failures. For instance, a blade could have failed, unbalancing the whole system, and leading to a break through the hub. Alternatively, the compressor could have broken through the hub, releasing the spinning fragments into the shroud where the blades were sheared off.

Figure 104 depicts the raw RPM data in blue, a filtered speed in red, the failure speed in yellow, and the pressure ratio (π_c) in purple. The raw data was from the IR interrupt sensor facing the turbine. The filtered speed was a region of 25 data points, averaged to reach each point's value. The failure speed was chosen to be where the compressor pressure ratio dropped to zero. The pressure ratio was the ratio of the total exit pressure to the total inlet pressure. The raw data in Figure 104a suggests the presence of two large vibrational modes centered around 35,000 RPM (3,665 Hz) and 57,000 RPM (5,970 Hz).

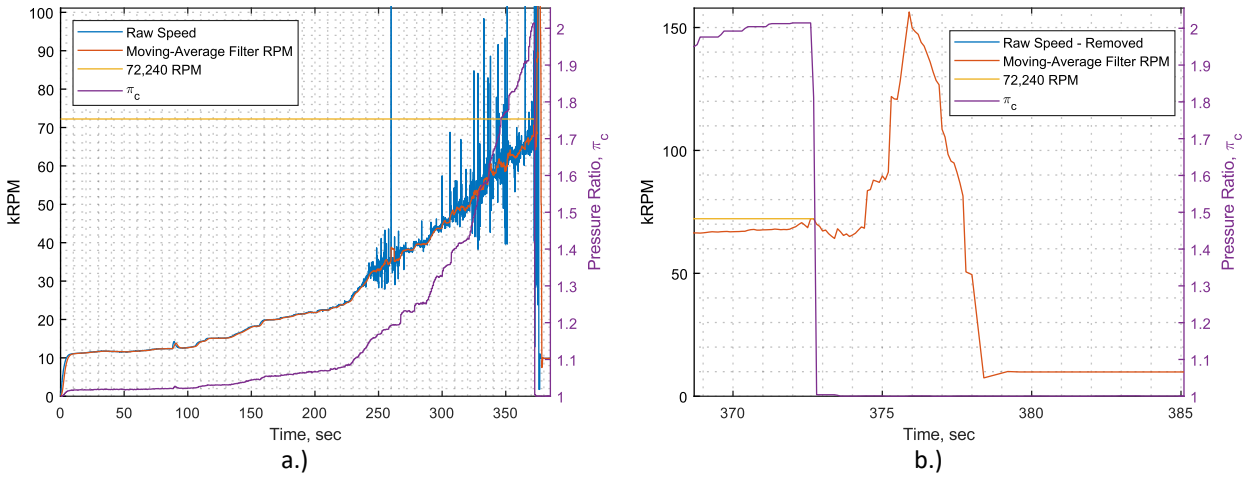

Figure 104. Experimental Failure Speed of the P400 Compressor, ULTEM 9085. a.) Full Compressor Run. b.) Region of Failure.

The region of the test around failure, shown in Figure 104b, shows how the failure speed was determined. The pressure ratio's steady climb dropped to 1.0 over the course of two data point. The sudden drop in pressure ratio implies that the compressor likely broke through the hub. If the break had been from one of the blades failing or from a region near the tip of the compressor, the pressure drop would have likely been over a longer period of time than 0.2 seconds. The filtered RPM dropped slightly post-failure. This might have been because the shaft was rubbing on a stationary compressor. Due to the sudden loss of a load, the turbine quickly began to speed up. This increase in speed was audible outside of the test cell. As the air continued to pull the turbine axially in the direction of the exit, the entire shaft was pulled in that direction. The shaft's motion was only stopped when the nut originally holding onto the compressor reached the bearing. At this point, the shaft broke in two, with the compressor side staying in the turbocharger and the turbine and remaining shaft quickly exiting the exhaust.

The collection of images from the failed compressor is shown in Figure 105. Figures 105a-b show the multitude of compressor fragments remaining after the failure

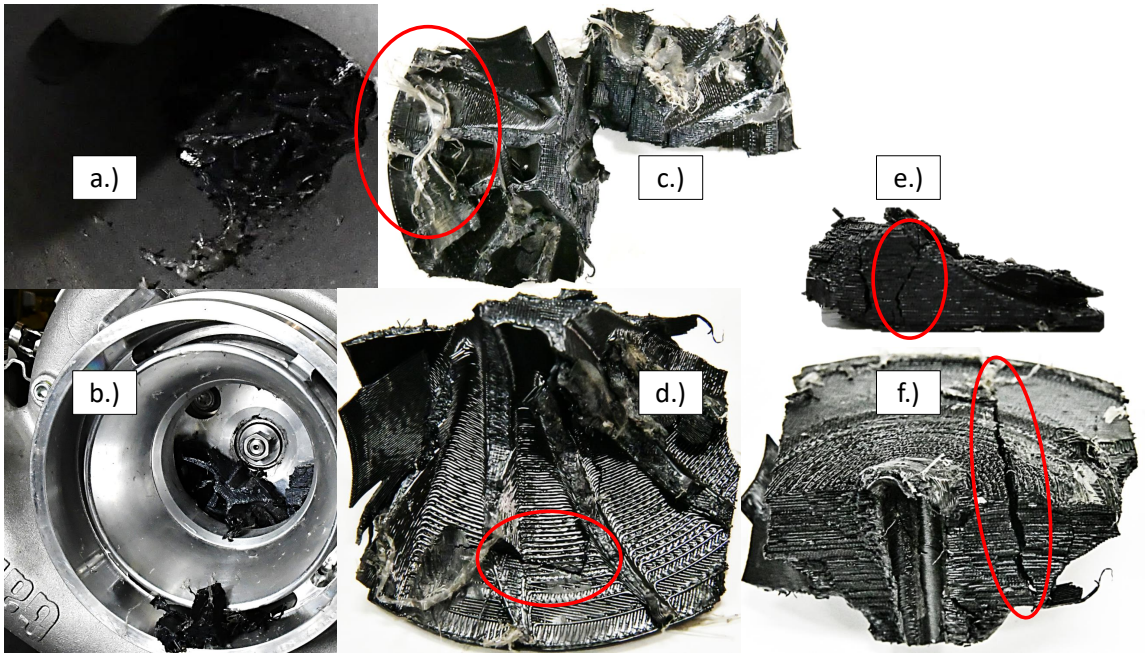

Figure 105. Post-Failure of the P400 Compressor, ULTEM 9085. a.)Plastic Fragments. b.)Compressor Shaft Pulled Through. c.) Two Fragments, Melted Plastic. d.) Large Fragment, Top. d.) Small Fragment. f.) Large Fragment, Bottom.

occurred. None of the compressor fragments exited the exhaust tube, likely due to the suddenly stopped airflow upon failure. The compressor side of the shaft is shown flush with the bearing in Figure 105b. Figure 105c is the two large fragments of the compressor. The similarities between the ULTEM compressor fragments to images of turbocharger compressor overspin failures in Section 2.1.4 provides additional evidence that the failure occurred through the hub. This was the predicted failure location from the FEA in Section 4.3.3. Also in Figure 105c are melted plastic peelings. The FEA predicted a deformation of 3.3 mm, which would have led to rubbing on the shroud. These melted plastic peelings were evidence that the blades were losing material to the shroud. This possibly completely eliminated tip clearance losses discussed in Section 2.1.5.1, improving performance once the material completely wore away. This "automatically-adjusting tip clearances" would have only occurred while

speed was increasing. If the compressor had slowed down, the tip clearances would have drastically increased.

Figure 105d shows the larger compressor fragment with all of the blades violently removed. Because of the inconsistencies in the failure, it appears that they were broken off from contacting the shroud rather than failing from rotational tension. The circled crack was at a location of high stress in the FEA model. Although not a predicted location of failure, the high amount of energy stored in that location could have led to a crack forming when the fragment hit the shroud. Figure 105e depicts the smaller of the two fragments. The crack circled in red was normal to the plane of failure and is present in the larger fragment as well in Figure 105f. Figure 105f also clearly shows fracture through the bore.

Figure 106a shows the back plate of the compressor housing. The top right hole has plastic scrapings in the direction of rotation. This corresponded with the cyclic rubbing heard when manually rotating the compressor. The shroud, shown in Figure 106b, had a constant line of melted plastic where the P400 shroud intersected with the original housing. This aligned with the FEA deformation predictions of the maximum deformation occurring axially in this location. Little rubbing was seen on the upstream section of the shroud, indicating that rubbing had not yet occurred at this location. Figure 106c is a photo of the damaged turbine after forceful ejection from the turbocharger. The amount of damage led to this turbocharger being replaced after this test and demonstrated the necessity of future test stand improvements.

4.3.5 Performance Analysis.

While the structural aspects of designing a compressor are necessary to consider, they are only there to allow the compressor to perform its only purpose, to compress air. A compressor that can spin at the desired speed but not compress any air is an

Figure 106. Housing and Turbine from P400 Compressor, ULTEM 9085 Test. a.) Compressor Back Plate. b.) Compressor Shroud. c.) Turbine.

even worse solution than a compressor than compresses well but cannot reach the full speed. There are three primary metrics that can be used to judge a compressor's "aerodynamic ability": the pressure ratio, the mass air flow, and the efficiency.

Because the total pressure is a measure of how much extractable energy is in the flow, the ratio of compressor exhaust to inlet pressure is used. Figure 107 shows the pressure ratio of the two measured total pressures, a fourth-order polynomial fit, and the stock P400 data from Grannon [36]. While the pressure is always below the stock P400 data, this cannot be used as conclusive evidence that AM compressors perform worse. One likely reason for this difference in π_c is the incorrect positioning of the back-pressure butterfly valve. Rather than any real-time adjustment of the back-pressure, the valve was set based on trial-and-error with the stock GTX5008R compressor. For subsequent compressor tests, the first stock P400 data point RPM should be reached and the back-pressure varied to match the initial π_c. From this, better conclusions could be achieved regarding the effects of AM on compressor per-

formance. The primary conclusion that should be drawn from this figure is that a reasonable amount of compression can be obtained from a plastic AM compressor.

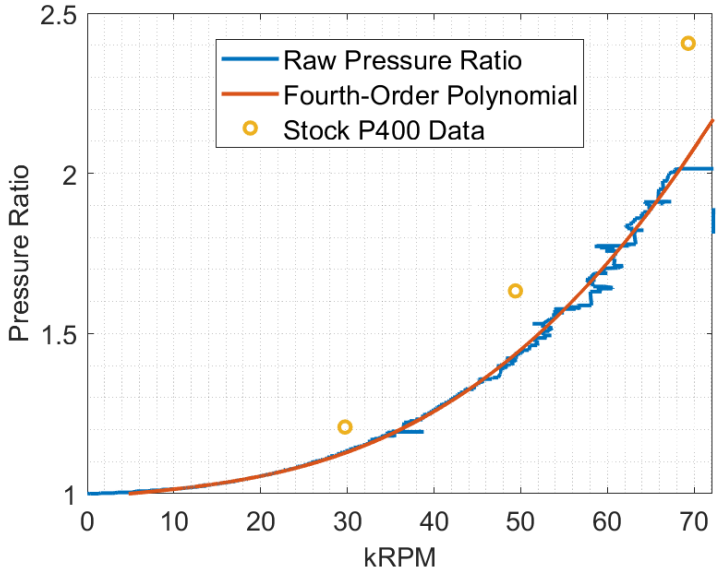

Figure 107. Pressure Ratio vs. RPM, P400 Compressor, ULTEM 9085 Test.

In addition to compressing air, the compressor must move enough air to achieve desired engine flow rates. Figure 108 shows the mass air flow through the compressor, corrected to standard conditions. This measurement was performed three different ways and all closely aligned. The first method used the differential pressure sensor and the definition of total pressure to obtain a velocity. This velocity was assumed to be representative of the flow and the continuity equation led to a mass flow rate. The second way used the values from the total and static pressure transducers. The primary difference in using these sensors is seen at low speeds with the increased noise. The final method used the automotive mass air flow sensor. All three methods closely aligned until the end of the test. At around 68,000 RPM, the MAF reported a large drop in mass air flow while the pressure transducers took longer to report this drop. This means that failure potentially occurred at 68,000 RPM rather than 72,240 RPM.

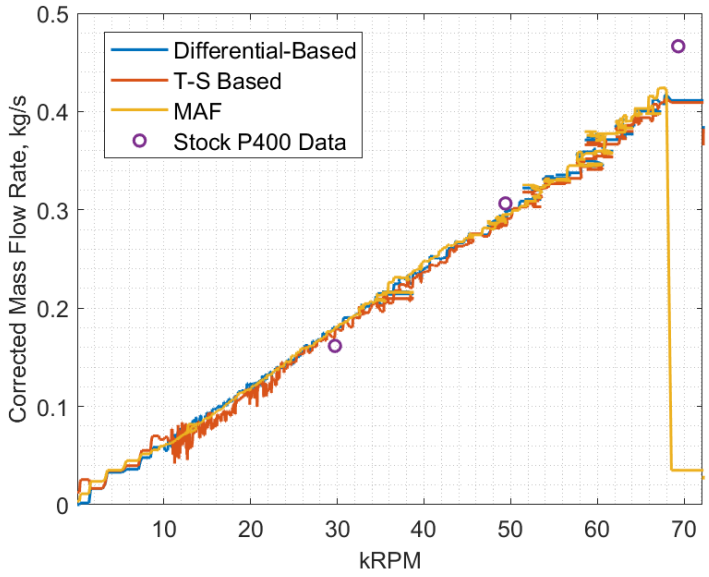

Figure 108. Mass Air Flow vs. RPM, P400 Compressor, ULTEM 9085 Test.

In addition to moving enough air, the compressor must be efficient enough to to maintain the compress-combust-expand cycle. If the efficiency is too low, the benefits gained from improved combustion would be lost to powering the compressor. Figure 109 depicts the isentropic efficiency (η_c) of the compressor. The blue line is η_c, calculated directly from the pressure and temperature measurements, shown in Equation 30. The red line is a fourth-order polynomial best fit of the data from 20,000-70,000 RPM. The circles are the stock P400 data. Due to the high margin of error for measuring η_c [36], the ULTEM P400 compressor cannot be said to be more or less efficient than the stock compressor, but does appear to have similar overall efficiency.

Similarly designed and sized compressors tend to behave similarly. For this reason, overlaying the P400 data onto a similarly-sized compressor map allows conclusions to be drawn regarding the P400 compressor. This was done by Grannan et. al. [36], the creators of the "Stock P400 Data". Rather than using the same compressor used in that paper, the comparison used the GTX5008R compressor map. This compressor

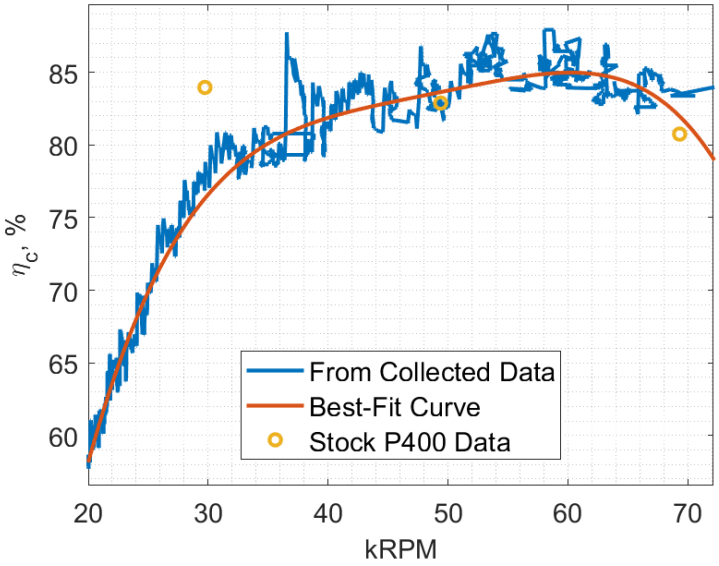

Figure 109. Isentropic Efficiency vs. RPM P400 Compressor, ULTEM 9085 Test.

was more similar in inducer and exducer size, maximum RPM, and maximum π_c than the BorgWarner S400SX3 compressor. The P400 ULTEM 9085 compressor data and the stock P400 compressor data are shown overlaid on the GTX5008R compressor map in Figure 110. As before, the stock P400 data closely aligned with the ULTEM P400 compressor. This plot solidifies the belief that the majority of the differences in performance were due to the incorrectly-set butterfly valve. The remaining data, plotting both the collected and the stock data from two other sets of data, demonstrates that, despite the compressors' similarity, they may not be identical enough for substitution.

For most compressor analysis, the aerodynamic losses, characterized by η_c, are the only losses of interest. The mechanical losses are usually both negligable and consistent between compressors. However, as seen from the melted plastic peelings seen in Figure 105c, there were abnormal sources of friction. Figure 111 shows the power removed from the turbine air stream, the power added to the compressor air stream, and the difference between the two. One source of this difference is likely the

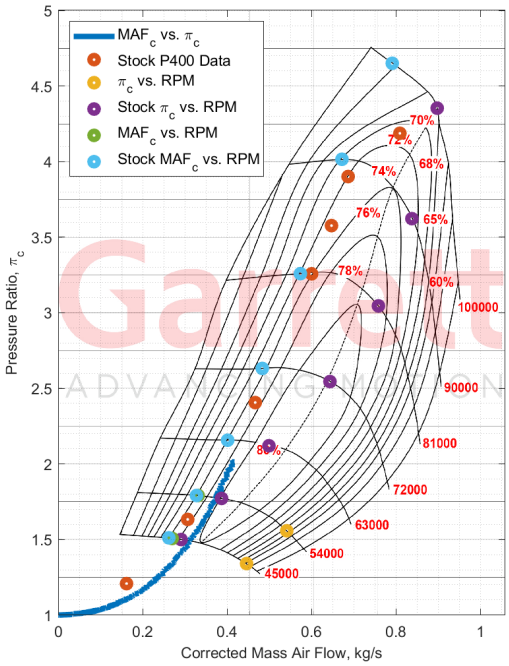

Figure 110. GTX5008R Compressor Map with P400 Compressor, ULTEM 9085 Data.

ULTEM compressor blades rubbing against the aluminum shroud. Unfortunately, the large magnitude of the power losses indicate that much of the lost power was from heat transfer from the flow to the system's metal piping, lasting until steady state. In order to determine the friction losses from compressor tip rubbing, a hysteresis study must be performed.

4.4 Compressor #3: Modified JetCat P400, 300-AMB

The 300-AMB photopolymer displayed more than adequate thermal properties in Section 4.1 and tensile strengths similar to ULTEM 9085. The largest problem of this material was the brittle nature of thin sections. In order to determine if the material was worth pursuing, finite element analysis was performed on a modified compressor design. The following section will cover the compressor design modifications in Section 4.4.1 and the finite element results in Section 4.4.2.

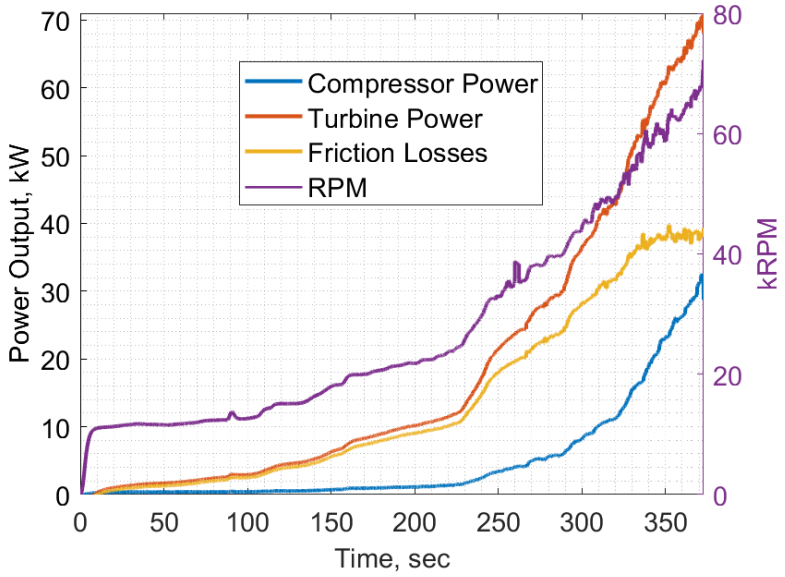

Figure 111. Compressor and Turbine Power and Losses, P400 Compressor, ULTEM 9085 Test.

4.4.1 Model Modifications.

The goal of this set of compressor modifications was to design a compressor with increased failure speed. There were three regions of high stress discovered during the ULTEM 9085 FEA, shown in Figure 102b. These regions are the bore stress, the right-angle connection where the blades initially connect to the body, and the blades as they turn radial.

Figure 112 depicts the new compressor beside the compressor use in the ULTEM 9085 test. The sudden transition from the blades to the body was modified to larger fillets. The fillet was increased to as large as the CAD software allowed. This could decrease the aerodynamic performance by decreasing the flow area, but it would drastically decrease the stresses experienced at the blade roots. The second change seen from this perspective was a trimming of the outer edge of the blades; this change had two benefits. The first benefit was a reduction of high-moment mass and the second benefit was providing room for a larger fillet to exist at the blade tips.

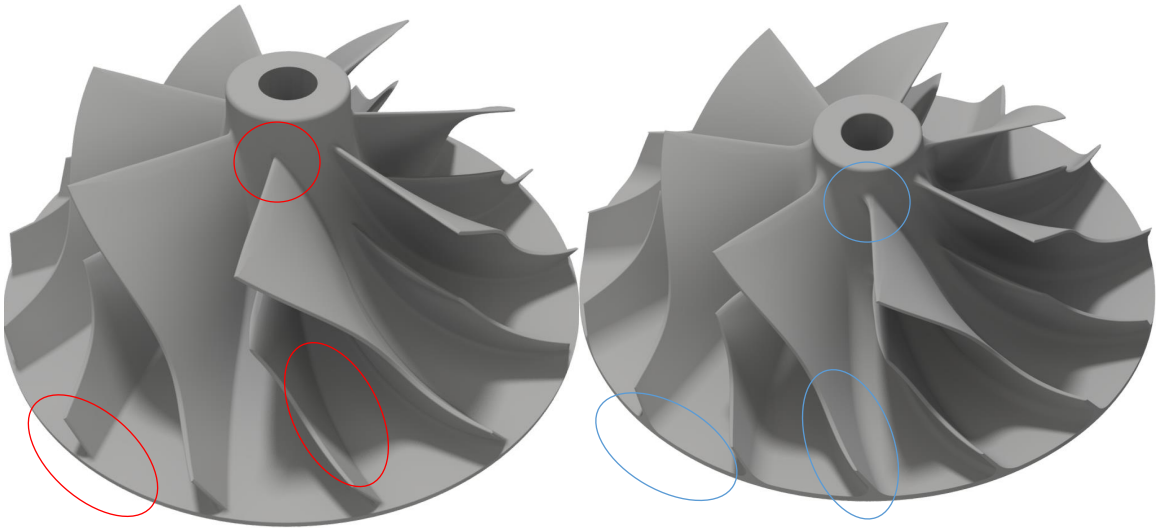

Figure 112. Modifications of P400 Compressor for 300-AMB from the top. Original ULTEM 9085 Compressor (left). Modified Design (right).

Figure 113 shows the redesigned compressor from a side profile. The largest modification was the large radius of curvature placed on the back face of the compressor; this decreased the stress concentration and provided more material to prevent expansion and bore failure. The large balancing ring was replaced with a thinner ring to eliminate more mass while leaving a stiffening ring near the blade tips. The large increase in fillet size is also shown.

4.4.2 Finite Element Analysis.

The thermal profile for the compressor under the boundary conditions discussed in Section 3.2.3 is shown in Figure 114. Due to the increased back face radius of curvature, the temperature for much of the bore decreased.

Figure 115 depicts the equivalent stresses and the deformation of the modified P400 compressor at 98 kRPM. The dark green through the hub will likely lead to failure at this speed. In addition to that location, the entire region where the blade intersects with the body appears to be above the ultimate strength. Because of the

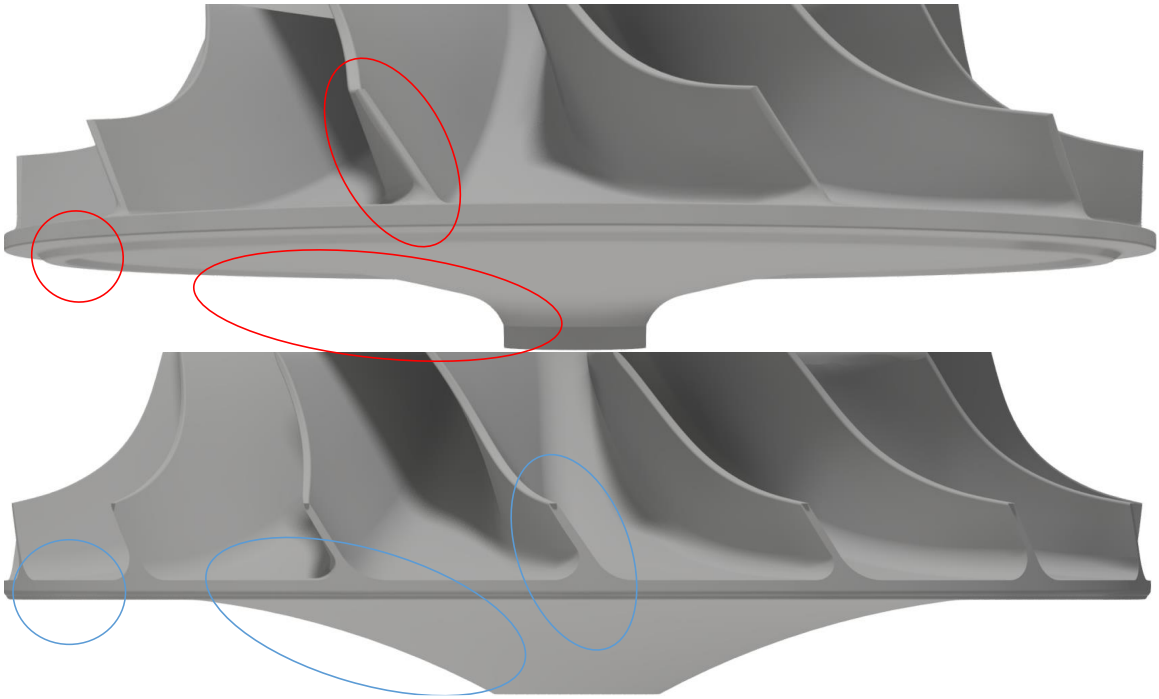

Figure 113. Modifications of P400 Compressor for 300-AMB from the side. Original ULTEM 9085 Compressor (top). Modified Design (bottom).

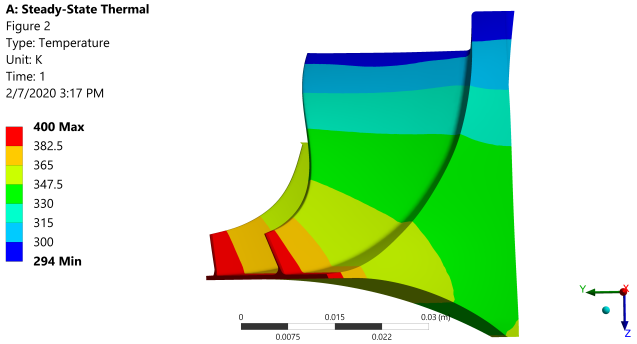

Figure 114. Thermal Profile for Modified P400 Compressor, 300-AMB

increased stiffness at higher temperature, the 300-AMB compressor deforms roughly a third as much as the ULTEM compressor.

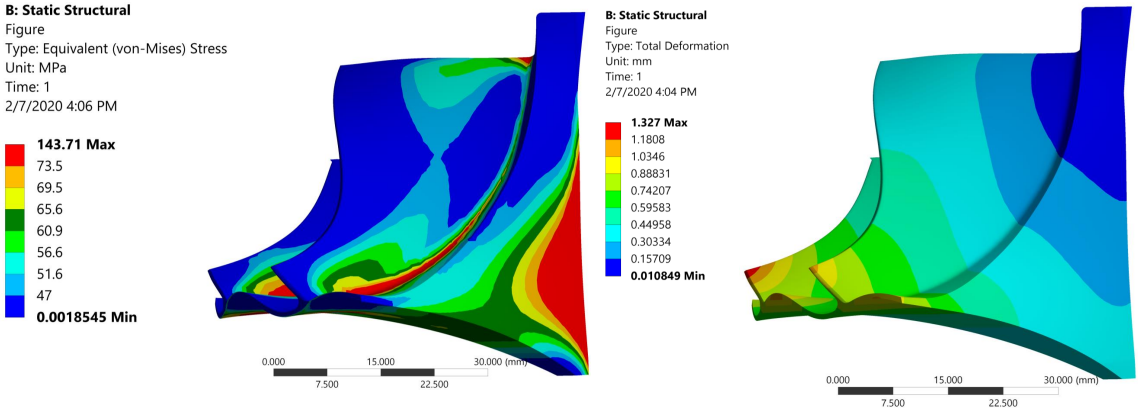

Figure 115. Stresses and Deformation for Modified P400 Compressor, 300-AMB, 98,000 RPM

By decreasing the rotational speed to 96 kRPM, the failure is no longer predicted to occur in the hub, rather, the blades appear to be likely to shear off. If the material was more ductile, the results found here would make it a worthwhile candidate for physical compressor testing. However, the brittleness would likely make balancing, assembly, and testing depend more on avoiding contact with the blades rather than the compressor structure itself.

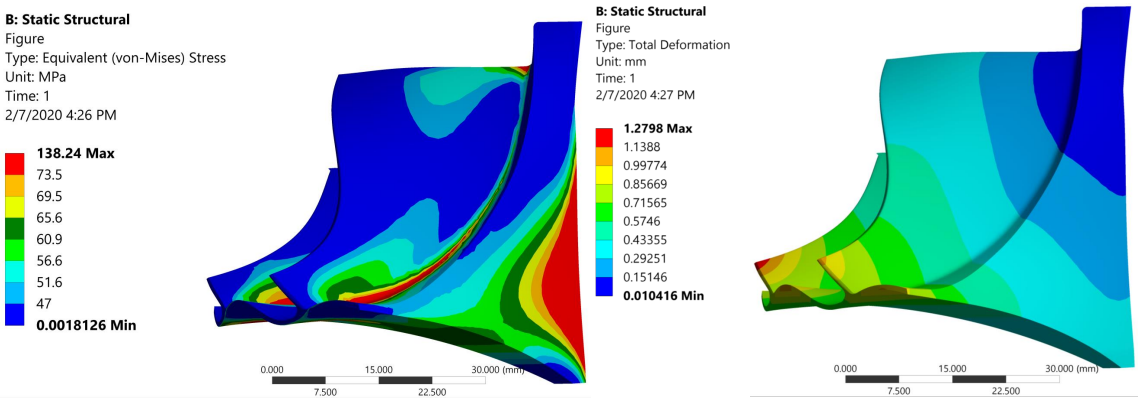

Figure 116. Stresses and Deformation for Modified P400 Compressor, 300-AMB, 96,000 RPM

4.5 Compressor #4: Modified JetCat P400, Onyx-Carbon Fiber

The final compressor tested was the Onyx material with continuous carbon fiber reinforcements. The high specific strength seen in Section 4.1 suggests the material would be a successful alternative to aluminum. The compressor design used was the one discussed for the 300-AMB analysis in Section 4.4.1. While the carbon fiber increased the cost roughly 10x and the build time 5x, the possibility of a successful compressor made these costs tolerable. The following section discusses any experimental (Section 4.5.1 and compressor (Section 4.5.2) modifications. Section 4.5.3 covers the FEA on the compressor model, Section 4.5.4 analyzes why this compressor failed, and finally, Section 4.5.5 compares the performance of the compressor to published data.

4.5.1 Experimental Variations.

This compressor had the high-speed camera to record failure, a variable ball valve to back-pressure the compressor, a three-way safety valve, and a new IR speed sensor. This new sensor performed even worse than the previous one, with max speeds only reaching 30,000 RPM before no longer working. The high speed camera was used to back out the failure speed.

4.5.2 Model Modifications.

The model was the same CAD file discussed in Section 4.4.1 for analysis with the 300-AMB photopolymer. The printed compressor was 64% carbon fiber by volume. Three key layers are shown in Figure 117 to demonstrate the large amount of carbon fiber within the compressor. At the widest location, all but two inner and two outer walls were made from continuous carbon fiber. The blades had reinforcement extending into the blade. This reinforcement disappeared towards the top of the print (front

of the finished compressor). The printed model is shown in Figure 118. Other than the leftover support material, the quality was visually significantly better than the ULTEM 9085 compressor, leading to a lower surface roughness.

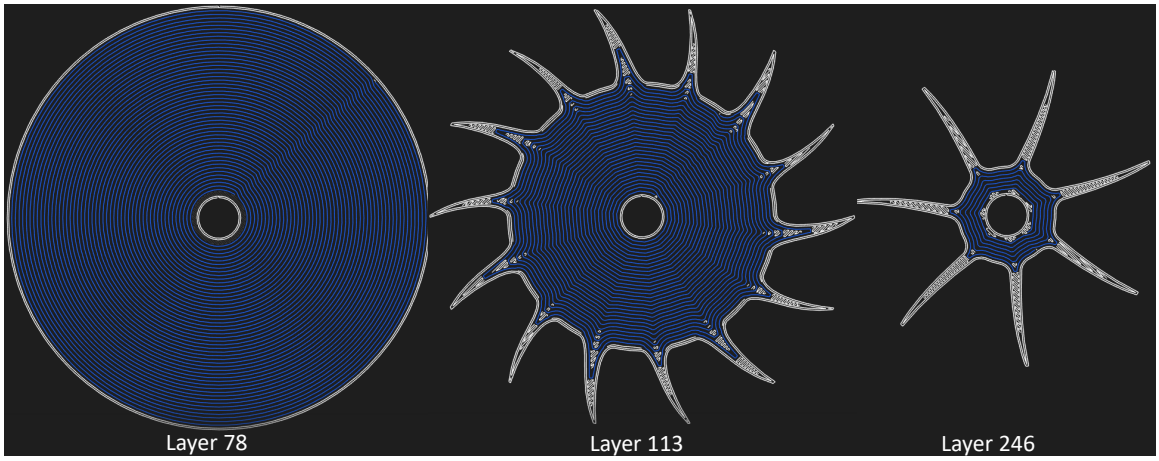

Figure 117. Key Print Layers, P400 Onyx-Carbon Fiber

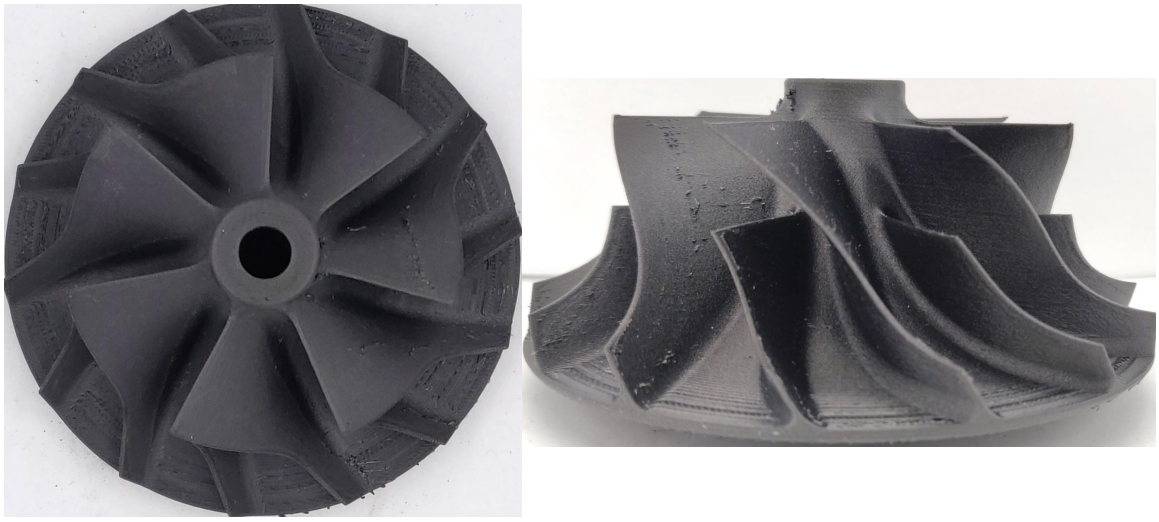

Figure 118. Printed Modified P400 Comressor, Onyx-Carbon Fiber

4.5.3 Finite Element Analysis.

Because the tensile testing had a small number of samples and the whole specimen was not heated, the measured material properties are not conclusive. This means that the modeling is significantly less accurate than the other compressor models.

Figure 119 below depicts the thermal profile of the modified compressor. This profile is identical to the 300-AMB compressor because the shape is the same and the compressor is at steady state.

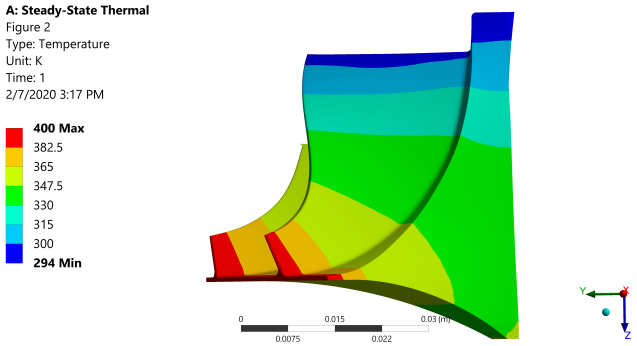

Figure 119. Thermal Profile for Modified P400 Compressor, Onyx-Carbon Fiber

At the operating speed of 98 kRPM, there were no stresses predicted to be above the ultimate strength of the compressor anywhere on the modified compressor for the carbon fiber. This is shown in Figure 120. The maximum stresses are roughly half of the ultimate strength for this material. While it is understood that the isotropic assumption applies significantly less now than before, the initial results predicted this compressor to withstand the loading. A more in-depth analysis would be able to split the model into separate regions and add directionally-dependent stress criteria to the model. The deformation at operating speeds was predicted to be roughly 0.65 mm, still three times higher than the aluminum compressor.

By increasing the speed, an initial prediction for the failure speed can be achieved. Using this technique, the stress concentration at the top of the compressor, shown in Figure 121, appears to be the location of failure at 160 kRPM. While this FEA analysis did not take into consideration many key factors that would have affected the failure speed, the initial estimations made it worthwhile to pursue.

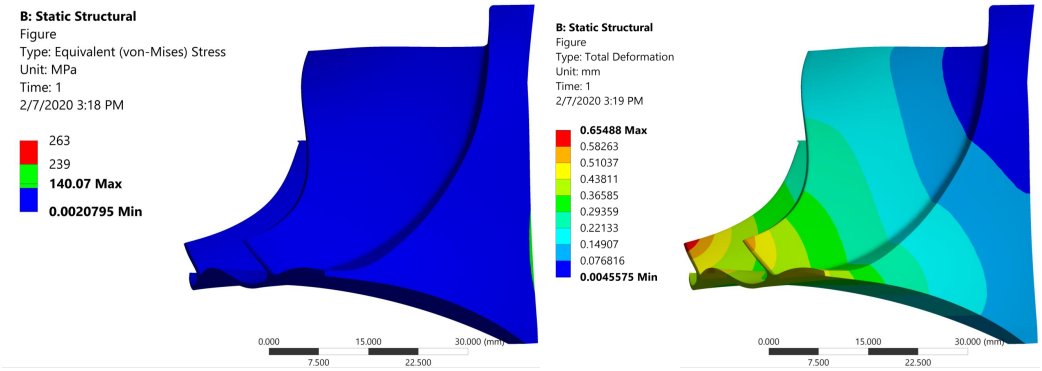

Figure 120. Stresses and Deformation for Modified P400 Compressor, Onyx-Carbon Fiber, 98,000 RPM

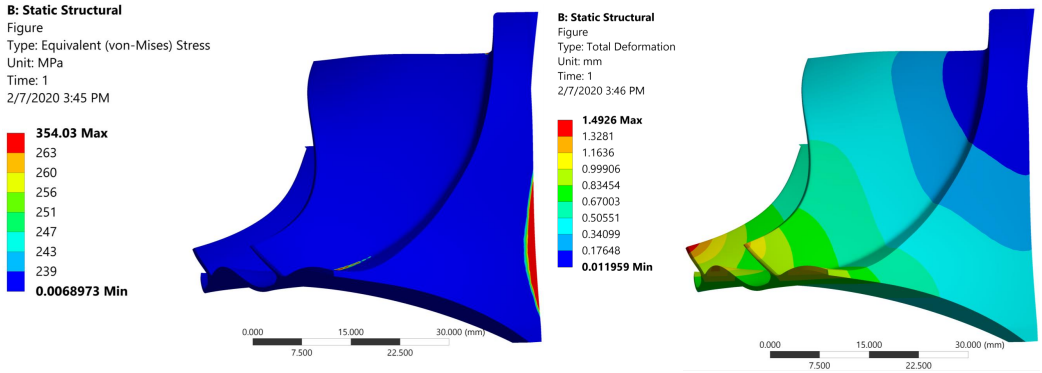

Figure 121. Stresses and Deformation for Modified P400 Compressor, Onyx-Carbon Fiber, 160,000 RPM

4.5.4 Failure Analysis.

Failure for this compressor did not occur violently as in the ULTEM 9085 compressor. Rather, some vibrational mode within the system was excited and the turbocharger began to shake violently. The experiment was ended when the vibrations were noticed. As seen in Figure 122, the violent shaking occurred at 34,200± 250 RPM.

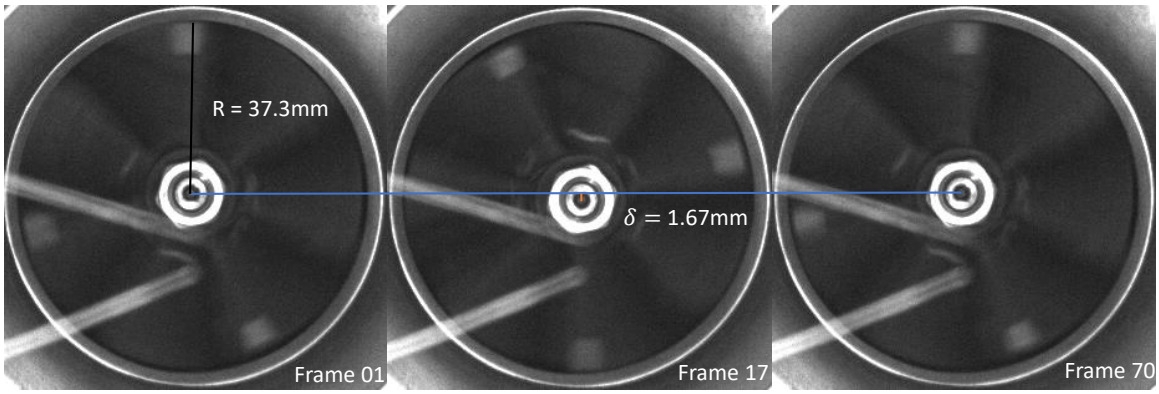

Figure 122. Failure Oscillations of Onyx-CCF Compressor

What was believed to have happened was that the compressor dimensional accuracy was lower than the ULTEM 9085 compressor. This is because of the large increase in material that had to be removed from one section of the compressor (≈500 mg) in order to achieve even the G-16 standard, discussed in Section 3.3.2.2. As the compressor accelerated, the expansion was asymmetric due to the large amount of material that had already been removed. This led to compounding imbalances. The failure that occurred from this is the nut screwing itself into the part and quickly melting/burning the nylon away to get inside the compressor. This melting also welded the compressor to the back plate of the turbocharger.

This failure occurred due to an inability to easily balance the turbocharger system, not because it had reach its material limit. If this compressor was reprinted with a

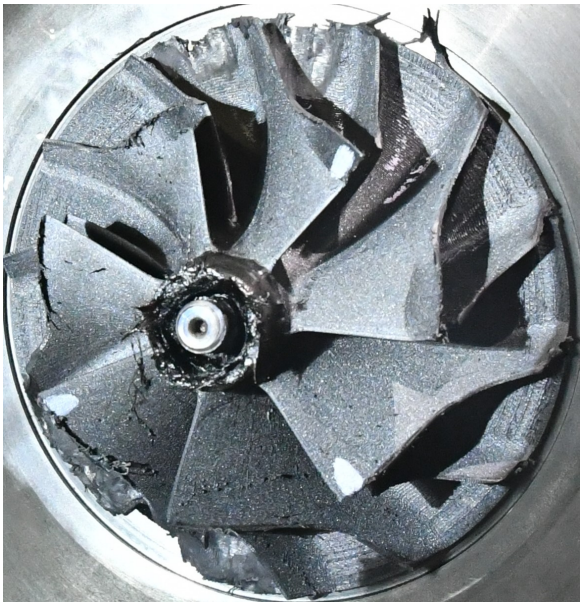

Figure 123. Compressor Failure, P400 Onyx-Carbon Fiber

balancing ring to allow proper balancing to occur, the top speed would have likely been significantly higher, as predicted by the FEA.

4.5.5 Performance Analysis.

Because the Onyx-CF compressor failed early on in testing, fewer conclusions can be made regarding the aerodynamic performance of this compressor in comparison to the ULTEM 9085 compressor. However, similar trends and conclusions appear in the pressure ratio and the efficiency. With the variable back-pressure valve, the pressure ratio shown in Figure 124 is closer to the published values than those seen in the ULTEM 9085 compressor.

Similarly, the Onyx-CF compressor's efficiency, shown in Figure 125 is within the margin of error for measuring isentropic efficiency for this size compressor. Although the limited data warrants future research, the close proximity of the measured data to the published stock data, both for the pressure ratio and the efficiency, demonstrates

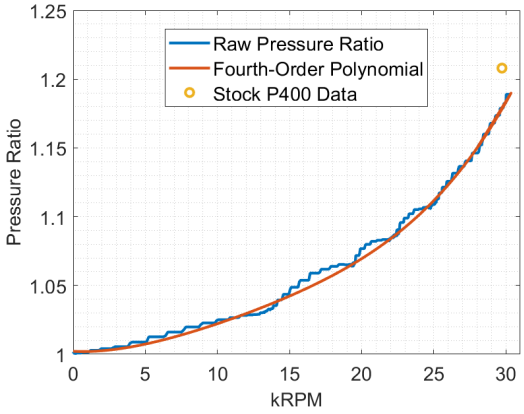

Figure 124. Pressure Ratio vs. RPM, Modified P400 Onyx-Carbon Fiber

the potential for effective substitution of these compressors into the stock P400 jet engine.

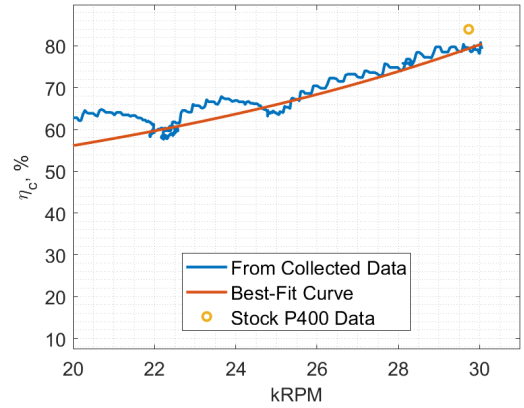

Figure 125. Isentropic Efficiency vs. RPM, Modified P400 Onyx-Carbon Fiber

V. Conclusion

The three objectives laid out at the beginning of this thesis and reiterated numerous times thoughout were achieved, each to varying levels of completeness. The first objective, "to design, build, and test an additively-manufactured centrifugal compressor that could be substituted into a commercial off-the-shelf micro-gas turbine," was met by the ULTEM 9085 and the Onyx-CF compressors. The ULTEM 9085 could be substituted directly into the JetCat P400 engine if operations was limited to under 70 kRPM. The modeling predicted a quality-built Onyx-CF compressor would easily withstand the expecting loading. The second objective, "to provide an initial correlation between AM compressors and failure speed using finite element analysis," was met with the physical testing of the ULTEM 9085 compressor, with failure occurring within a few hundred RPM of predicted failure. The third and final objective, "to attempt to characterize the effects of AM on compressor performance," was met by showing that the compressors produced pressure ratios on par with the stock compressors with efficiencies statistically indistinguishable from the stock compressors. More fine measurements would be required to raise the statistical certainty of the difference in efficiencies.

The three materials analyzed all showed the promise of creating a substitute compressor. The ULTEM 9085 had decent strengths and stiffnesses. However, because it was printed on the highest quality printer, the compressors needed minimal post-processing and balanced much quicker and easier than the Onyx printer. The 300-AMB had the most desirable temperature range. This meant that the strength and stiffness did not vary considerably with temperature. However, the inability to print with the XY plane in the $r - \theta$ plane of the compressor and the brittle nature of the material made it less ideal of a solution and was not pursued beyond FEA modeling. The fiber-reinforced nylon had exciting strength, stiffness, and temperature

range. While the printer had significantly better surface finish, it was slower, more expensive, and had worse dimensional accuracy than the ULTEM 9085.

The ULTEM 9085 compressor, though it failed below the desired speed, failed close to the speed predicted by the FEA model. Although this was likely due to a balancing of simplifications (not steady state vs. isotropic material) it provided an initial launching point for future compressor work. Because the JetCat P400 can idle from 30,000 RPM, with only slight modifications, this compressor could get the JetCat engine to operate over half of its range of speeds. One way to improve this material would be to insert thin metal bands within the body of the compressor. The additional stiffness and strength could be gained with only a small amount of additional time.

While the Onyx-CF compressor did not reach close to the speeds predicted by the FEA model, the type of failure was encouraging. Rather than the compressor failing structurally, the mating between the compressor and the turbocharger shaft failed, likely an unrepeatable freak accident. The compressor structure was completely undamaged except for the bolt melting into the compressor bore. This likely has a variety of simple solutions. A short list of possible solutions include a metal insert to prevent the nut from melting into the compressor, a spring washer between the nut and the compressor, shrinking the compressor bore to increase the bore friction, a physical locking mechanism such as a key or "D"-shape, leaving unnecessary material on the bounds of the compressor to take off while balancing, and shrinking down the blade tips to prevent rubbing and binding.

The second goal was to determine if FEA could be used to accurately predict compressor failure. For the one compressor that actually failed in a structural manner, it closely matched the predicted speed. Although it was accurately predicted 100% of the time, a single data point is not conclusive. While much more work needs to be

done to determine how well the compressor failure can be modeled with the relatively simplified boundaries, the results are promising.

The third goal was much more difficult to obtain with just the two compressors tested to failure. The results from the ULTEM 9085 test demonstrated that there was not a statistically significant aerodynamic performance difference between the metal compressor and the ULTEM compressor. While the poor surface finish in the additively-manufactured compressors likely decreased performance relative to the stock compressors, the lower stiffnesses likely led to tip rubbing and a resultant reduction in tip-clearance losses.

More certain measurements would be necessary in order to conclude any difference between the stock and AM materials. The outward expansion of the blades significantly affected the work balance. Because the ULTEM 9085 was able to merely melt off rather than smoke like the Onyx-carbon fiber, gradually wearing away the tips would be a acceptable solution to correcting the tip rubbing. If the blade tips were thinned out for the region of expected wear, they would still prevent tip losses during acceleration without introducing as much foreign matter into the combustor. The physical removal of blade material would lead to a large hysteresis present in compressor operations.

The primary future work would include remodeling the Onyx-carbon fiber compressor to both better hold on to the shaft and to have material designated for removal during balancing. By trimming down the blades, the chance that they rub on the shroud as violently goes down. The final future work needed to demonstrate a working, AM plastic compressor would be to improve the manner in which speed was detected. A common method is the inclusion of a magnetic nut on the compressor side. This would hopefully eliminate both freezing air and the large amounts of noise associated with using the current IR speed sensors.

By remodeling the compressor, a few tests could show that a plastic compressor could successfully replace the metal compressors, allowing for a drastic decrease in the cost and time per design cycle iteration. This will allow future innovation to progress at a faster rate, combining the usefulness and strength typically only seen in subtractive manufacturing with the freedom of creativity and design of rapid, low-cost additive manufacturing.

Bibliography

1. Gibson, I., Rosen, D., and Stucker, B., *Additive Manufacturing Technologies*, Springer, New York City, NY, 2nd ed., 2005.

2. Japikse, D. and Baines, N., *Introduction to Turbomachinery*, Concepts ETI, Inc.; Oxford University Press, Norwich, VT; Oxford, England, 1st ed., 1994.

3. Rodgers, C., "Specific Speed and Efficiency of Centrifugal Impellers," *proc. ASME 25th Gas Turbine Conference*, , No. A80-36101 14-34, March 1980, pp. 191–200.

4. Logan, E., *Turbomachinery: Basic Theory and Applications*, Marcel Dekker, Inc., New York City, NY, 2nd ed., 1993.

5. Otto, K. and Wood, K., *Product Design: Techniques in Reverse Engineering and New Product Development*, Pearson Education, Inc., Bloomington, MN, 12th ed., 2013.

6. J.D. Mattingly and K.M. Boyer, *Elements of Propulsion*, American Institute of Aeronautics and Astronautics, Inc., Reston, 2nd ed., 2016.

7. Creative Commons Licensing, "Attribution-ShareAlike 3.0 Unported," January 2020, Accessed via website, Jan-2020.

8. Pulkrabek, W. W., *Engineering Fundamentals of the Internal Combustion Engine*, Pearson Education Inc., Bloomington, MN, 2nd ed., 2016.

9. Dobson, J., "'JetMan' Yves Rossy Soars Like a Superhero: The Future of Human Flight in Dubai," 2015, Accessed via website, Jan-2020.

10. JetCat, "JetCat P400 Pro Product Information and Specifications," Ballrechten-Dottingen, Germany, 2020, Accessed via website, Jan-2020.

11. Motion, G. A., "GARRETT® GTX5008R Turbocharger Images and Specifications," 2019, Accessed via website, Jan-2020.

12. Panton, R.L., *Incompressible Flow*, John Wiley and Sons, Inc., Hoboken, NJ, 3rd ed., 2005.

13. Moran, M.J., Shapiro, H.N., Munson, B.R., and DeWitt, D.P., *Introduction to Thermal Systems Engineering*, John Wiley and Sons, Inc., Hoboken, NJ, 1st ed., 2003.

14. Buckingham, E., "One Physically Similar Systems; Illustrations of the Use of Dimensional Equations," *Physics Revised*, Vol. 4, No. 4, 1999, pp. 345–376.

15. Balje, O.E., "A Study of Reynolds Number Effects in Turbomachinery," *Journal of Engineering for Power*, Vol. 86, No. 3, July 1964, pp. 227–235.

16. Van den Braembussche, R.A., *Micro Gas Turbines – A Short Survey of Design Problems*, von Kármán Institute for Fluid Dynamics, Rhode-St-Genese, Belgium, 2005.

17. Balje, O.E., *Turbomachines*, John Wiley and Sons, Inc., New York City, NY, 1st ed., 1981.

18. Harman, R.T.C., *Gas Turbine Engines*, John Wiley and Sons, Inc., New York City, NY, 1st ed., 1981.

19. Wilson, D.G., *The Design of High-Efficiency Turbomachinery and Gas Turbines*, MIT Press, Cambridge, MA, 1st ed., 1984.

20. Pfleiderer, C., *Die Kreiselpumpen (The Centrifugal Pumps)*, Springer-Verlag, Berlin, Germany, 1st ed., 1949.

21. Boyce, M.P., *Gas Turbine Engineering Handbook*, Gulf Publishing Co., Houston, TX, 1st ed., 1981.

22. Zheng, X., Jin, L., Du, T., Gan, B., Liu, F., and Qian, H., "Effect of temperature on the strength of a centrifugal compressor impeller for a turbocharger." *Proceedings of the Institution of Mechanical Engineers, Part C: Journal of Mechanical Engineering Science*, Vol. 227, No. August, 2013, pp. 896–904.

23. Floren, C., "One Question: Talking Turbocharger Explosions With Chris Floren Of Garrett Motion," August 2019, Accessed via website, Feb-2020.

24. Muthu, S.E., Dileep, S., and Mishra, R.K., "Optimization of a Centrifugal Impeller for a Small Gas Turbine Engine: A Finite Element Approach," *Proceedings of the ASME 2012 Gas Turbine India Conference*, December 2012.

25. Miller, J.K., "Turbo: Real World High Performance Turbocharger Systems," *CarTech Inc.*, 2008, Accessed via website, Feb-2020.

26. Roark, R. J., Young, W. C., and Plunkett, R., *Formulas for Stress and Strain*, Vol. 43, McGraw-Hill, 7th ed., 2002.

27. Callister, W.D. and Rethwisch, D.G., *Fundamentals of Materials Sceince and Engineering: an Integrated Approach*, John Wiley and Sons, Inc., Hoboken, NJ, 4th ed., 2012.

28. Gillaugh, D, *Individual Conversations with a FEA Professional, May-December 2019*, AFL-RQT, Dayton, OH, 2019.

29. MatWeb, "MatWeb Material Property Data," 2020, Accessed via website, Feb-2020.

30. Turunen-Saaresti, T. and Jaatinen, A., "Influence of the Different Design Parameters to the Centrifugal Compressor Tip Clearance Loss," *Journal of Turbomachinery*, Vol. 135, No. 1, 2012, pp. 011017.

31. Jaatinen-Varri, A, Turunen-Saaresti, T., Gronman, A., and Roytta, P., Backman, J., "The tip clearance effects on the centrifugal compressor vaneless diffuser flow fields at off-design conditions," *10th European Conference on Turbomachinery Fluid Dynamics and Thermodynamics, ETC 2013*, April 2013, pp. 972–982.

32. Pampreen, R., "Small Turbomachinery Compressor and Fan Aerodynamics," *Journal of Engineering for Power*, Vol. 95, 07 1973, pp. 251.

33. Kays, W., Crawford, M., and Weigand, B., *Convective Heat and Mass Transfer*, McGraw-Hill, New York City, NY, 4th ed., 2005.

34. Tang, Y., Xi, G., Wang, Z., and Tian, Y., "Quantitative Study on Equivalent Roughness Conversion Coefficient and Roughness Effect of Centrifugal Compressor," *Journal of Fluids Engineering*, Vol. 142, No. 2, October 2019.

35. Adams, T., Grant, C., and Watson, H., "A Simple Algorithm to Relate Measured Surface Roughness to Equivalent Sand-grain Roughness," *International Journal of Mechanical Engineering and Mechatronics*, Vol. 1, January 2012.

36. Grannan, N.D., Hoke, J., McClearn M.J., Litke, P., and Schauer, F., "Trends in JetCat Microturbojet-Compressor Efficiency," *AIAA SciTech Forum: 55th AIAA Aerospace Sciences Meeting*, January 2017.

37. Kirk, E.G., "Composite Materials for Future Aeroengines," *International Gas Turbine and Aeroengine Congress and Exposition*, June 1989.

38. Vo, H.D. and Trepanier, J.Y., "Undergraduate Project in Compressor Rig Design, Fabrication, and Testing for Complete Engineering Training," *Journal of Engineering for Gas Turbines and Power*, Vol. 138, No. 5, May 2016.

39. Fernández, S., Jiménez, M., Porras, J., Romero, L., Espinosa, M. M., and Domínguez, M., "Additive Manufacturing and Performance of Functional Hydraulic Pump Impellers in Fused Deposition Modeling Technology," *Journal of Mechanical Design*, Vol. 138, No. 2, December 2015.

40. Meier, M.A., Gooding, W.J., Fabian, J., and Key, N., "Considerations for Using Additive Manufacturing Technology in Centrifugal Compressor Research," *Proceedings of ASME Turbo Expo 2019: Turbomachinery Technical Conference and Exposition*, June 2019.

41. Walker, G.T., Turner, M.G., Holley, A.T., and Hoke, J.L., "Experimental Test Rig for 3D Printed, Axial Compressor Utilizing a COTS Turbocharger," *AIAA Scitech 2020 Forum*, January 2020.

42. Jia, D., Li, F., and Zhang, Y., "3D-printing process design of lattice compressor impeller based on residual stress and deformation," *Scientific Reports*, Vol. 10, No. 1, December 2020, pp. 600.

43. Meli, E., Rindi, A., Ridolfi, A., Furferi, R., Buonamici, F., Iurisci, G., Corbo, S., and Cangioli, F., "Design and Production of Innovative Turbomachinery Components via Topology Optimization and Additive Manufacturing," *International Journal of Rotating Machinery*, , No. September, 2019, pp. 1–12.

44. Stratasys, *Collection of Material Property Datasheets*, 2019, Accessed via website, Feb-2020.

45. Additive Manufacturing Research Group, *The 7 Categories of Additive Manufacturing*, Loughborough University, 2020, Accessed via website, Feb-2020.

46. Molitch-Hou, M., *Additive Manufacturing: Materials, Processes, Quantifications and Applications*, Butterworth-Heinemann, Mississauga, Canada, 1st ed., 2018.

47. Varotsis, A.B., *Introduction to Binder Jetting 3D printing*, 3D Hubs, 2012, Accessed via website, Feb-2020.

48. Varotsis, A.B., *Introduction to Material Jetting 3D printing*, 3D Hubs, 2012, Accessed via website, Feb-2020.

49. Carlota, V., *The Complete Guide to Directed Energy Deposition (DED) in 3D Printing*, 3D Natives, 2019, Accessed via website, Feb-2020.

50. ASTM F2792-12a, "Standard Terminology for Additive Manufacturing Technologies, (Withdrawn 2015)," Tech. rep., ASTM International, West Conshohocken, PA, 2012, Accessed via website, Feb-2020.

51. Byberg, K. I., Gebisa, A. W., and Lemu, H. G., "Mechanical properties of ULTEM 9085 material processed by fused deposition modeling," *Polymer Testing*, Vol. 72, October 2018, pp. 335–347.

52. Ngo, T. D., Kashani, A., Imbalzano, G., Nguyen, K. T., and Hui, D., "Additive manufacturing (3D printing): A review of materials, methods, applications and challenges," *Composites Part B: Engineering*, Vol. 143, Feburary 2018, pp. 172–196.

53. 3D Systems, *Collection of Material Property Datasheets*, 3D Systems, Inc., 2019, Accessed via website, Feb-2020.

54. Markforged, *Collection of Material Property Datasheets*, Markforged, Inc., 2019, Accessed via website, Feb-2020.

55. ASTM D638-14, "Standard Test Method for Tensile Properties of Plastics," *ASTM International*, 2014.

56. *Poisson Ratio of Polymeric Materials*, Polymer Properties Database, 2015, Accessed via website, Feb-2020.

57. Koutromanos, I., *Fundamentals of Finite Element Analysis: Linear Finite Element Analysis*, John Wiley and Sons, Inc., Hoboken, NJ, 1st ed., 2018.

58. Kim, N., *Introduction to Nonlinear Finite Element Analysis*, Springer Science + Business Media, New York City, NY, 1st ed., 2015.

59. Pletcher, R.H., Tannehill, J.C., Anderson, D.A., *Computational Fluid Mechanics and Heat Transfer*, Taylor and Francis Group, LLC., Boca Raton, FL, 3rd ed., 2013.

60. Venkateshan, S.P., *Mechanical Measurements*, John Wiley and Sons, Ltd., Chichester, United Kingdom, 2nd ed., 2015.

61. Barlow, Jewel, Rae, William Jr., Pope, A., *Low-Speed Wind Tunnel Testing*, John WIley & Sons, Inc, New York, 3rd ed., 2018.

62. Starkweather, R., Agrawal, P.D., Fisher, J., *AlChE Equipment Testing Procedure: Centrifugal Compressors - A Guide to Peroformance Evaluation and Site Testing*, John Wiley and Sons, Inc., Hoboken, NJ, 2013.

63. Anderson, D.A., *Hypersonics and High-temperature Gas Dynamics*, American Institute of Aeronautics and Astronautics, Inc., Reston, VA, 2nd ed., 2006.

64. Nicholas, J.V. and White, D.R., *Traceable Temperatures: An Introduction to Temperature Measurement and Calibration*, John Wiley and Sons, Inc., Chichester, England, 2nd ed., 2001.

65. RS Components, "Data Pack E, RS Data Sheet, Thermocouples," Tech. Rep. November, Corby, United Kingdom, November 2005, Accessed via website, Feb-2020.

66. Morris, Alan S., Langari, R., *Measurement and Instrumentation: Theory and Application*, Academic Press, Boston, MA, 2nd ed., 2015.

67. National Instruments, "Decoding Tachometer Signals Using CompactRIO and LabVIEW FPGA," 2015, Accessed via website, Feb-2020.

68. McMaster-Carr, "Collection of Product Specifications," *McMaster-Carr Website*, 2019, Accessed via website, Feb-2020.

69. Tiller, C.R., *Patent for Acoustic Tachometer*, No. 4,452,079, United States Patent Office, June 1984.

70. Moffat, R., "Describing the Uncertainties in Experimental Results," *Experimental Thermal and Fluid Science*, Vol. 1, January 1988, pp. 3–7.

71. Moffat, R., "Contributions to the Theory of Single-Sample Uncertainty Analysis," *Transactions of the ASME*, Vol. 104, No. June, 1982, pp. 250–260.

72. ASTM D648-01, "Standard Test Method for Deflection Temperature of Plastics Under Flexural Load in Edgewise Position," *ASTM International*, 2001.

73. Buhrman, R., *Calibration Report, 22 Kip Displacement*, MTS Systems Corporation, Eden Prairie, MN, 2019, Calibration performed for AFIT.

74. Buhrman, R., *Calibration Report, 22 Kip Force*, MTS Systems Corporation, Eden Prairie, MN, 2019, Calibration performed for AFIT.

75. MTS, *Model 653 High-Temperature Furnaces*, MTS Systems Corporation, Eden Prairie, MN, 2018.

76. Omega, A Spectric Company, *Collection of Product Specifications*, Omega Website, 2019, Accessed via website, Feb-2020.

77. Monarch Instruments, *ROLS-W Product Specification Sheet*, 2019, Accessed via website, Feb-2020.

78. BiTorq, *Collection of Product Specifications*, Bitorq Valve Automation, A Division of Strahman Valves, Inc., 2019, Accessed via website, Feb-2020.

79. IRD Balancing, "Balance Quality Requirements of Rigid Rotors, The Practical Application of ISO 1940/1," March 2009.

80. Barre, C., "Hot Isostatic Pressing, Advanced Materials, and Processes," *ASM International*, Vol. 155, No. March, 1999, pp. 47.

81. Chawla, K.K., *Composite Materials: Science and Engineering*, Springer, New York City, NY, 3rd ed., 2013.

Vita

Aaron P. Bauer

EDUCATION

Masters of Science in Aeronautical Engineering. Air Force Institute of Technology (March 2020). Focus in heat transfer and air breathing propulsion.

Bachelors of Science in Mechanical Engineering. United States Air Force Academy (May 2018). Focus in additive manufacturing, mechatronics, linear controls, heat transfer, and materials.

PUBLICATIONS

Jensen, D.D., Wood, K.L., Bauer, A.P., Perez, B., Doria, M., and Jensen, L. "A Bio-Inspired Mind Map to Assist in Concept Generation for Wall Climbing Systems: Development, Assessment, and Resulting Prototypes." 2018 ASEE Annual Conference and Exposition. Paper ID 21644.

Bauer, A.P., Anderson, M.L., DePaola, R.A., Chimento, C., Gwaltney, C., Taylor, N., Teope, K. "Methods for Deploying Payloads from Multi-Rotor Unmanned Aerial Systems." AIAA Scitech 2019 Forum. AIAA 2019-1285.

Bauer, A.P., Schauer, F.R., Walker, G., Gillaugh, D., Kemnitz, R., Bohan, B.T., Holley, A.T., Hoke, J. "Design, Analysis, and Testing of a Low-Cost, Additively-Manufactured, Single-Use Compressor." AIAA Scitech 2020 Forum. AIAA 2020-0125.

PRESENTATIONS AT PROFESSIONAL MEETINGS

Bauer, A.P., Schauer, F.R., Walker, G., Gillaugh, D., Kemnitz, R., Bohan, B.T., Holley, A.T., Hoke, J. "Design, Analysis, and Testing of a Low-Cost, Additively-Manufactured, Single-Use Compressor." AIAA Scitech 2020 Forum. AIAA 2020-0125.

Bauer, A.P., Schauer, F.R., Walker, G., Gillaugh, D., Kemnitz, R., Bohan, B.T., Holley, A.T., Hoke, J. "Design, Analysis, and Testing of a Low-Cost, Additively-Manufactured, Single-Use Compressor." 44th Dayton-Cincinnati Aerospace Sciences Symposium. 45DCASS-063.

REPORT DOCUMENTATION PAGE

Form Approved
OMB No. 0704–0188

1. REPORT DATE *(DD–MM–YYYY)*	2. REPORT TYPE	3. DATES COVERED *(From — To)*
13-03-2020	Master's Thesis	Sept 2018 — Mar 2020

4. TITLE AND SUBTITLE

DESIGN, DEVELOPMENT, AND TESTING OF A LOW COST, ADDITIVELY-MANUFACTURED, CENTRIFUGAL COMPRESSOR

5a. CONTRACT NUMBER

5b. GRANT NUMBER

5c. PROGRAM ELEMENT NUMBER

6. AUTHOR(S)

Aaron P. Bauer

5d. PROJECT NUMBER

5e. TASK NUMBER

5f. WORK UNIT NUMBER

7. PERFORMING ORGANIZATION NAME(S) AND ADDRESS(ES)

Air Force Institute of Technology
Graduate School of Engineering and Management (AFIT/EN)
2950 Hobson Way
WPAFB OH 45433-7765

8. PERFORMING ORGANIZATION REPORT NUMBER

AFIT/MS/ENY/20-M-254

9. SPONSORING / MONITORING AGENCY NAME(S) AND ADDRESS(ES)

Air Force Research Labs, Aerospace Systems Directorate
Building 71A, 7th Street
WPAFB OH 45433-7765
Email: frederick.sschuaer@afit.edu

10. SPONSOR/MONITOR'S ACRONYM(S)

AFRL/RQTC

11. SPONSOR/MONITOR'S REPORT NUMBER(S)

12. DISTRIBUTION / AVAILABILITY STATEMENT

DISTRIBUTION STATEMENT A:
APPROVED FOR PUBLIC RELEASE; DISTRIBUTION UNLIMITED.

13. SUPPLEMENTARY NOTES

14. ABSTRACT

The three objectives of this research were to: 1.) design, build, and test AM compressors to substitute into COTS micro-gas turbine engines, 2.) provide initial correlations between FEA and compressor failure speed, and 3.) characterize the effects of AM on compressor performance. These goals improved the design cycle cost and the design-validation time cycle. ULTEM 9085, 300-AMB, and Onyx-Kevlar temperature-dependent tensile properties were measured. FEA-predicted failure speeds of stock compressor designs led design improvements, potentially fulfilling the original compressor requirements. Physical testing of the stock and ULTEM 9085 compressors occurred. Comparing these compressors' performances demonstrated that low cost, AM materials are viable alternatives for certain micro-turbine applications. An improved Onyx-Carbon Fiber compressor was tested to failure. These results provide a proof of concept supporting AM compressors, improving the development time cycle. This approach enables high-risk yet low-cost research and development. Additionally, with proper mission planning, low-cost AM compressors could provide significant improvements to engine cost and weight for limited-life applications.

15. SUBJECT TERMS

Micro-Turbine Engine, Centrifugal Compressor, Additive Manufacturing (AM), Material Extrusion, Continuous Fiber Filament, Material Testing, Finite Element Analysis (FEA), Commericial, Off-the-shelf (COTS)

16. SECURITY CLASSIFICATION OF:			17. LIMITATION OF ABSTRACT	18. NUMBER OF PAGES	19a. NAME OF RESPONSIBLE PERSON
a. REPORT	b. ABSTRACT	c. THIS PAGE			Dr. I. M. Smart, AFIT/ENP
U	U	U	U	190	19b. TELEPHONE NUMBER *(include area code)* (937) 255-3636, x4555; amy.magnus@afit.edu